



University of Perugia
Department of Physics and Geology
Master in Physics
Curriculum Astrophysics and Astroparticles
Class 2021 – 2022

Thesis

Real-time monitoring of Solar Energetic Particles with Alpha Magnetic Spectrometer on the International Space Station

Andrea Serpolla

Supervisor

Matteo Duranti, Ph.D.
INFN Perugia

Co-supervisor

Alberto Oliva, Ph.D.
INFN Bologna

Acknowledgments

Part of the work presented in this thesis was performed in presence at CERN, thanks to a 3-months scholarship provided by the National Scientific Commission 2, or *Commissione Scientifica Nazionale 2* (CSN2), of the National Institute of Nuclear Physics, or *Istituto Nazionale di Fisica Nucleare* (INFN) [1].

A special thanks goes to both my supervisors, Matteo Duranti, Ph.D. and Alberto Oliva, Ph.D., who have always provided me with their help and support.

Contents

Introduction	1
1 Cosmic Rays	3
1.1 All-particle energy spectrum	3
1.1.1 Spectral index	3
1.1.2 Particles origin	4
1.2 Composition of Galactic Cosmic Rays	5
1.3 Modelization	6
1.3.1 Sources	6
1.3.2 Diffusive shock acceleration	6
1.3.3 Propagation	8
1.4 Propagation in the Heliosphere	9
1.4.1 Solar modulation	9
1.4.2 Geomagnetic field	11
1.5 Detection	12
1.5.1 Ground experiments	13
1.5.2 Balloon experiments	13
1.5.3 Space experiments	14
2 Solar Energetic Particles	19
2.1 Structure of the Sun	19
2.2 Solar Magnetic Field	20
2.3 Solar Plasma	21
2.4 Heliosphere	22
2.5 Coronal Mass Ejections	22
2.6 Solar Energetic Particle events	23
2.7 Composition of Solar Energetic Particles	24
3 Alpha Magnetic Spectrometer	29
3.1 Permanent magnet	30
3.2 Silicon Tracker	31
3.3 Time of Flight	33
3.4 Anti-Coincidence Counters	34
3.5 Transition Radiation Detector	34
3.6 Ring Imaging Cherenkov	36
3.7 Electromagnetic Calorimeter	37
3.8 Trigger system	38
3.8.1 Fast Trigger	39

3.8.2 Level 1 trigger	40
3.9 Data Acquisition System	42
3.10 Monitoring Interface	43
4 Detection of Solar Energetic Particles	47
4.1 Data source	47
4.2 Data preprocessing	48
4.3 Data analysis	49
4.4 Data buffering filters	51
5 Real-time monitoring of Solar Energetic Particles	59
5.1 Quiet level definition	59
5.2 Scoring	61
5.3 Background subtraction	61
5.4 Event detection	64
5.5 Real-time monitoring	64
5.6 Alert system	64
Conclusions	67
A AMS live-time and triggers	69
B Solar Proton Events	93
C Time-series from the real-time monitor	95
Bibliography	105
List of Acronyms	115

Introduction

The International Space Station orbits in the Low Earth Orbit and is continuously occupied by astronauts. The Station travels at an altitude of about 400 km where the residual atmosphere and the geomagnetic field shield it from cosmic radiation. The space is indeed permeated by a flux of Cosmic Rays, i.e. charged energetic particles, than can represent an actual hazard for human activities out of Earth.

CR spectrum goes from 10^8 to 10^{21} eV (fig. 1.1) and is generated by galactic and extra-galactic sources. Supernovae (SNe) and Supernovae Remnants (SNRs) produce most of the Galactic Cosmic Rays (GCRs) [2] while the extra-galactic component is produced by radio sources and Active Galactic Nuclei (AGNi). After their production, GCRs are injected into the Interstellar Medium (ISM) by a Diffusive Shock Acceleration (DSA), which explains particles energization through "head-on", scattering-like interactions with the irregularities of a moving magnetic field [3]. During their propagation in the galaxy, CRs are subject to energy gain and losses, that can be described with Fokker-Planck equation (eq. 1.2) [4]. After entering the Heliosphere, i.e. the region where the solar activity predominates over the action of the galactic winds, CRs go through the Solar Magnetic Field (SMF) and the Solar Wind (SW). At this point, the propagation can be described by the Parker's equation 1.3 [5]. This equation can be solved analytically (e.g. using Force Field Approximation) or numerically (e.g. using Stochastic Differential Equations). The SW, in particular, is a flow of plasma that expands into the Heliosphere with a velocity of 400–800 km/s; its presence influence the low hand of the CR spectrum. In particular, the solar activity gives rise to the solar modulation, in which an anti-correlation can be seen between the solar activity and the flux of CRs (fig. 1.5). The study of the time varying conditions of the Heliosphere makes the *Space Weather*.

Among the various phenomena that compose the Space Weather, there are the Solar Energetic Particles (SEPs). SEPs are bursts of high-energy particles from the Sun that can last for hours or even days; they have energies between ~ 10 keV and several GeV, with a $\beta_{\max} = 0.9$. They are mainly composed by protons and electrons, but also by heavier elements from He to Au and Pb. SEP events can be categorized as *impulsive* or *long-duration/gradual*. The first type is produced by reconnection of oppositely directed magnetic field lines in the high corona of the Sun, which can eject electrons and ions into space, forming a *coronal jet* [6]. Impulsive events have generally short durations and can be accompanied by the production of an electromagnetic flare. The second type is energized by a Coronal Mass Ejection (CME) and has a longer duration [7].

Because of the wide range of the CR spectrum, the local environment of the ISS is not always capable of shielding the spacecraft from cosmic radiation. The low part of the energy scale of CR spectrum is influenced by the presence of SEPs and the SW. In particular the former is capable of producing intense flux of charged particles with energies of several GeV that can actually reach the ISS and its crew in some regions of the orbit. The ISS is equipped with dosimeters to monitor the doses absorbed by astronauts. The Alpha Magnetic Spectrometer (AMS) is also mounted on the ISS and can be used to detect SEPs.

The AMS-02 instrument is equipped with many detectors of the modern particle physics research to reveal the CR spectrum. In particular, AMS is composed of a Silicon Tracker that mea-

sures rigidity; a Time-of-Flight (ToF) that measures velocity and charge; Anti-Coincidence Counters (ACC) that detect particles entering sideways; a Transition Radiation Detector (TRD) that identifies e^\pm from p and nuclei and measures the charge; a Ring Imaging Cherenkov (RICH) that measures velocity and charge; an Electromagnetic Calorimeter (ECAL) that measures the energy and discriminates electromagnetic particles from hadronic one.

The AMS monitors and detects CR flux continuously. Faldi et al. show in [8] how it is possible to identify SEP events by looking at the trigger rate of the instrument. The low latency data of the trigger system allows accordingly to perform a real-time monitoring and alert for SEPs near the ISS. Such possibility would improve the current monitoring adopted to protect the space crews with a new reliable source of data. Therefore, this thesis intends to prove how it is possible to build a complete monitoring and alert system, taking advantage of all the trigger rates of AMS detectors, with the possibility of alerting ISS occupants for SEP events in progress.

First chapters are dedicated to the introduction of references about CRs (chapter 1), SEPs (chapter 2) and AMS instrument (chapter 3). Then, chapter 4 is dedicated to an identification algorithm for SEPs detection and chapter 5 to the realization of a monitoring and alert system for SEP events.

Part of the work presented in this dissertation was performed in presence at CERN.

Chapter 1

Cosmic Rays

Cosmic Rays (CRs) are composed by charged particles that reach Earth from all directions. In particular they are composed of 90% of protons, 8% of helium nuclei, 1% of electrons and another 1% of other nuclei and anti-matter, specifically anti-protons and positrons.

CRs can come from inside or outside our galaxy. *Galactic Cosmic Rays (GCRs)* are produced mainly in *Supernovae (SNe)* and *Supernovae Remnants (SNRs)*, while origins of extra-galactic ones are currently believed to be *radio sources* and *Active Galactic Nuclei (AGNs)*. In particular, GCRs produced by SNe are injected into the Interstellar Medium (ISM) by a *Diffusive Shock Acceleration (DSA)*, which explains the energy gains as "head-on", scattering-like interactions with the irregularities of a moving magnetic field. After their injection, CRs propagate within ISM passing through energy gains and losses that change their composition and that can be modelled with a Fokker-Planck equation. For instance, the anti-matter component is produced just by the interactions with the medium. After their trip in the Galaxy, the particles enter the Heliosphere and they undergo the effects of the solar activity and of the geomagnetic field. The final result is an experimental spectrum in energy that goes from 10^8 to 10^{21} eV. This spectrum can be divided into a *primary* component, made by the particles produced and accelerated at their astrophysical sources and a *secondary* component, produced by the interaction with the medium (e.g. ISM, Earth atmosphere, etc...). The first one can be detected with instruments outside the atmosphere or in its last layers. Anyway, also ground-based experiments are arranged to study the most energetic particles.

1.1 All-particle energy spectrum

The figure 1.1 shows CR all-particle energy spectrum. The spectrum covers a range that goes from 10^8 to 10^{21} eV, with the maximum flux at 2–3 GeV and that can be described by the power law

$$\Phi(E) \propto E^{-\gamma} \quad (1.1)$$

with the spectral index $\gamma \approx 2.8$.

1.1.1 Spectral index

The spectral index changes its value twice, at the so-called "*knee*" and "*ankle*" of the spectrum. The knee is located at $10^{15} - 10^{16}$ eV and corresponds to an hardening of γ up to 3. This change should reflect the fact that galactic sources have reached their maximum ability to accelerate CRs [10]. The ankle is located at $10^{18} - 10^{19}$ eV and here the spectral index goes back to its original value of 2.8. Compared to the first one, this change has a less clear explanation and it could be the

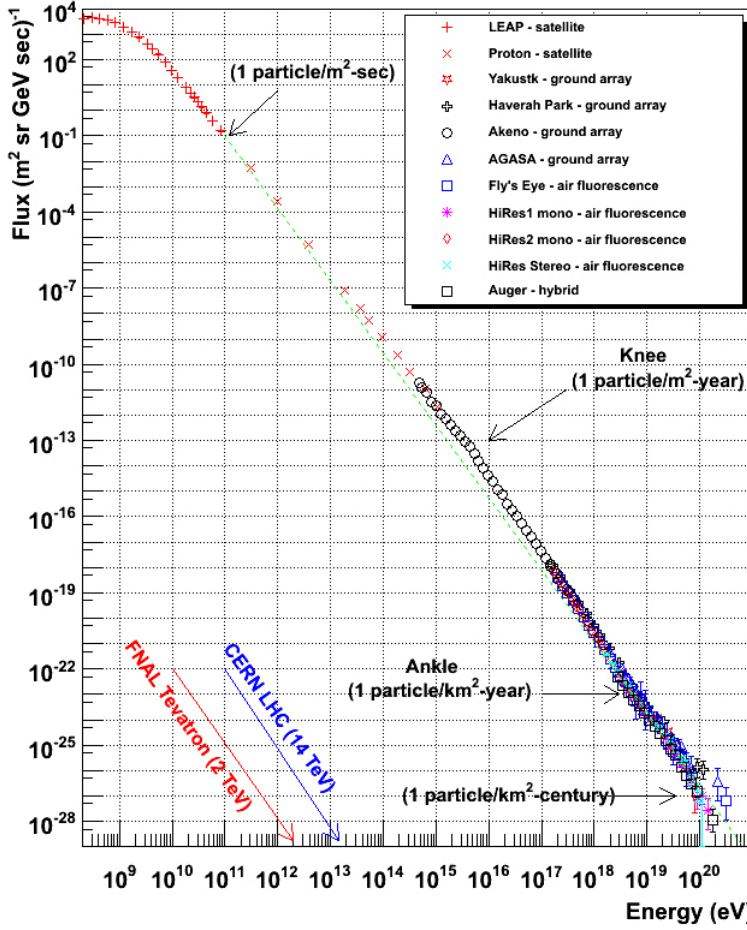


Figure 1.1: all-particle CR energy spectrum as measured by various experiments [9].

evidence of a higher energy population overtaking a lower one, for example extra-galactic particles overtaking the galactic ones [10], or the appearance of a new phenomenon, such as pair production due to the interaction of extragalactic protons with the Cosmic Microwave Background (CMB) radiation (i.e. $p + \gamma \rightarrow p + e^+ + e^-$) [11]. Above 10^{19} eV, the flux should also be suppressed by the *Greisen-Zatsepin-Kuzmin mechanism (GZK-mechanism)* [12] which affirms that CRs start interacting with the CMB radiation through the Δ^+ resonance (i.e. $p + \gamma \rightarrow \Delta^+ \rightarrow p(n) + \pi^0(\pi^+)$) with a consequent decrease of their path length in the ISM. The presence of an excess above that level can not be explained without an exotic explanation and the experimental data confirms a strong suppression compatible with the theory.

1.1.2 Particles origin

CRs can be produced by the Sun, by other astrophysical objects inside our galaxy or also outside that.

The Solar activity can produce particles with energies of the order of the MeV [13], while Rays above the GeV are considered to come from outside the solar system.

Regarding galactic and extra-galactic particles, electrons strongly suffer from Inverse Compton losses, due to the interaction with the CMB and synchrotron emissions, so even the most energetic particles can not travel more than a few kpc [14] (see fig. 1.2). Therefore, electrons are usually

considered to have a galactic origin and are used to study nearby astrophysical objects. On the contrary, energy losses of protons and nuclei during the interactions with the ISM are negligible. Their path is mostly influenced by the presence of the galactic magnetic field, so to assess if a particle is galactic or not, the gyroradius $r = p/(ZeBc)$ is taken into account and compared to the size of the Galaxy. Ultimately, it can be demonstrated that protons under 10^{15} eV are galactic, while above 10^{18} eV it is impossible to contain them, so they could be extra-galactic or be produced by closer sources and travel an almost straight path.

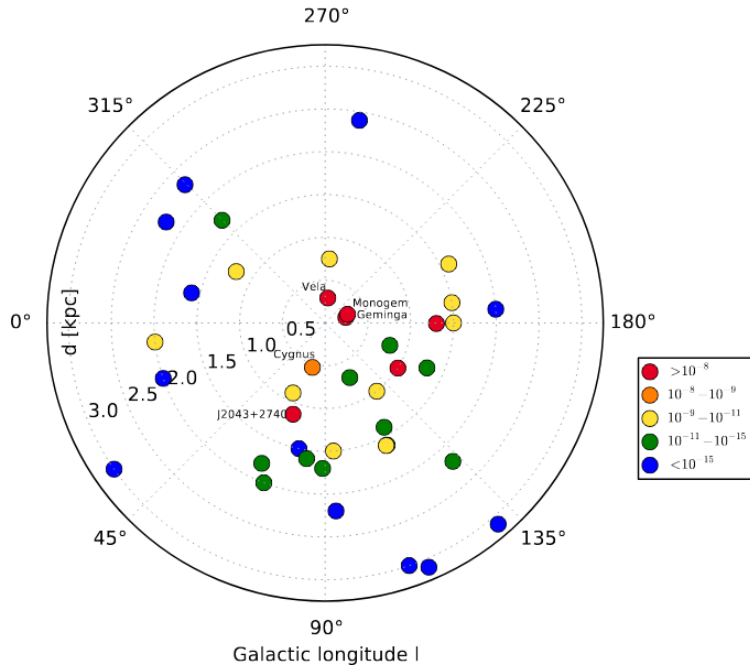


Figure 1.2: sample of single Supernovae Remnants and Pulsars in terms of their Galactic longitude and distance to the Earth, that is located at the center of the circle [14]. The color scale of the dots quantifies the electron flux integrated from 50 GeV to 5 TeV in units of $(\text{cm}^2 \text{ s sr})^{-1}$.

1.2 Composition of Galactic Cosmic Rays

The figure 1.3 shows the elemental abundances in GCRs with respect to the solar system ones.

The compatibility between GCRs and solar system abundances of the main elements of the stellar nucleosynthesis, in particular nitrogen, oxygen and iron, indicates that CRs should mostly have a stellar origin. In fact, SNe are considered the main source of GCRs.

GCRs are much more abundant in Li, Be, B ($Z = 3, 4, 5$) and Sc, Ti, V, Cr, Mn ($Z = 21-25$) [16]. Those elements are almost absent among the products of stellar nucleosynthesis and their excess is explained by the interaction between CRs and the ISM, specifically by the spallation of carbon, oxygen and iron nuclei. From a knowledge of the cross sections for spallation, it is possible to compute the quantity of matter crossed by the particle between its production and its detection, that for the bulk of CR results to be $X \simeq 5 \text{ g/cm}^2$. Then, considering the Galaxy disk density $\rho \simeq 1 \text{ proton/cm}^3$, a lower limit on the travelled distance can be obtained as $l = X/(m_p \rho) \sim 1000 \text{ kpc}$. Since the considered abundances concern CRs with a galactic origin and the travelled distance l is much greater than the thickness of the disk $d \simeq 0.2 \text{ kpc}$, GCRs wander for a long time before actually being able to escape the Galaxy or being detected.

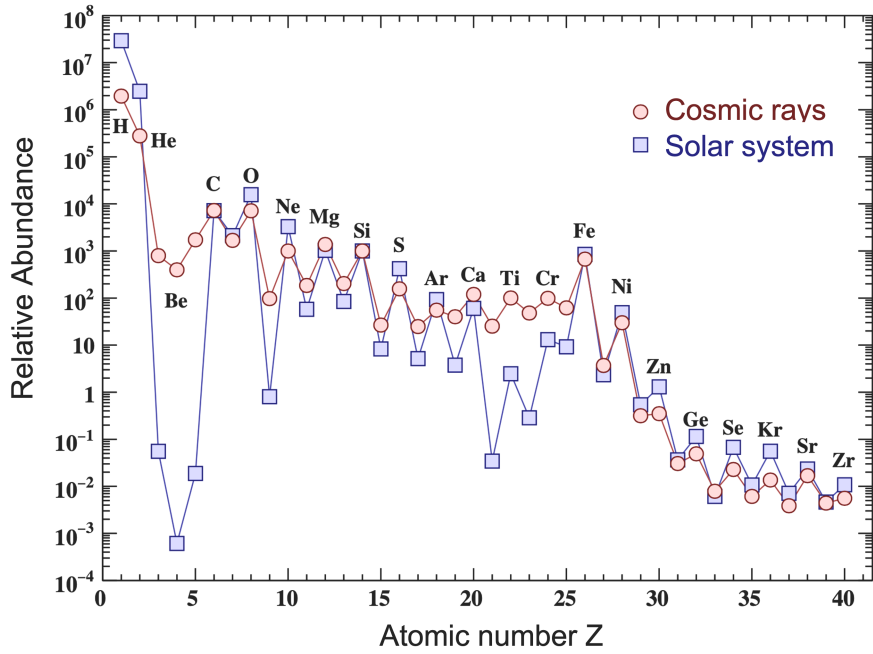


Figure 1.3: elemental abundances in GCRs relative to Si ($X_{\text{Si}} = 10^3$) compared to the abundances in the solar system [15].

Finally, measured CRs contain also a fraction of antimatter, in particular positrons and anti-protons. Those particles are actually secondary particles, produced by the interaction with the ISM [17]. The figure 1.4 shows the measured flux ratios $e^+/(e^+ + e^-)$ and \bar{p}/p .

1.3 Modelization

This section describes the CRs modelization from their sources until their entering in the Heliosphere. This section consider the CRs recognised sources, acceleration mechanisms and propagation theory in the ISM.

1.3.1 Sources

Currently *Supernovae Remnants (SNRs)* are recognised as the main source of GCRs. This hypothesis is confirmed from radio, optical and γ -rays spectra observations, from which it is also possible to estimate the value of the spectral index at the moment of particles injection into the ISM [2].

An extra-galactic origin is assumed for the highest energies (i.e. $E \gtrsim 10^{18}$ eV), since the acceleration mechanism that takes place in SNe, the diffusive shock acceleration, becomes ineffective and the particles gyroradius becomes greater than the size of the Galaxy. For that case, *radio sources* and AGNi are studied as possible CRs sources [18].

1.3.2 Diffusive shock acceleration

The main acceleration mechanism proposed for CRs is the *Diffusive Shock Acceleration (DSA)*. It was proposed for the first time by Fermi [3] and explains particles energy gains through the motion within an irregular magnetic field.

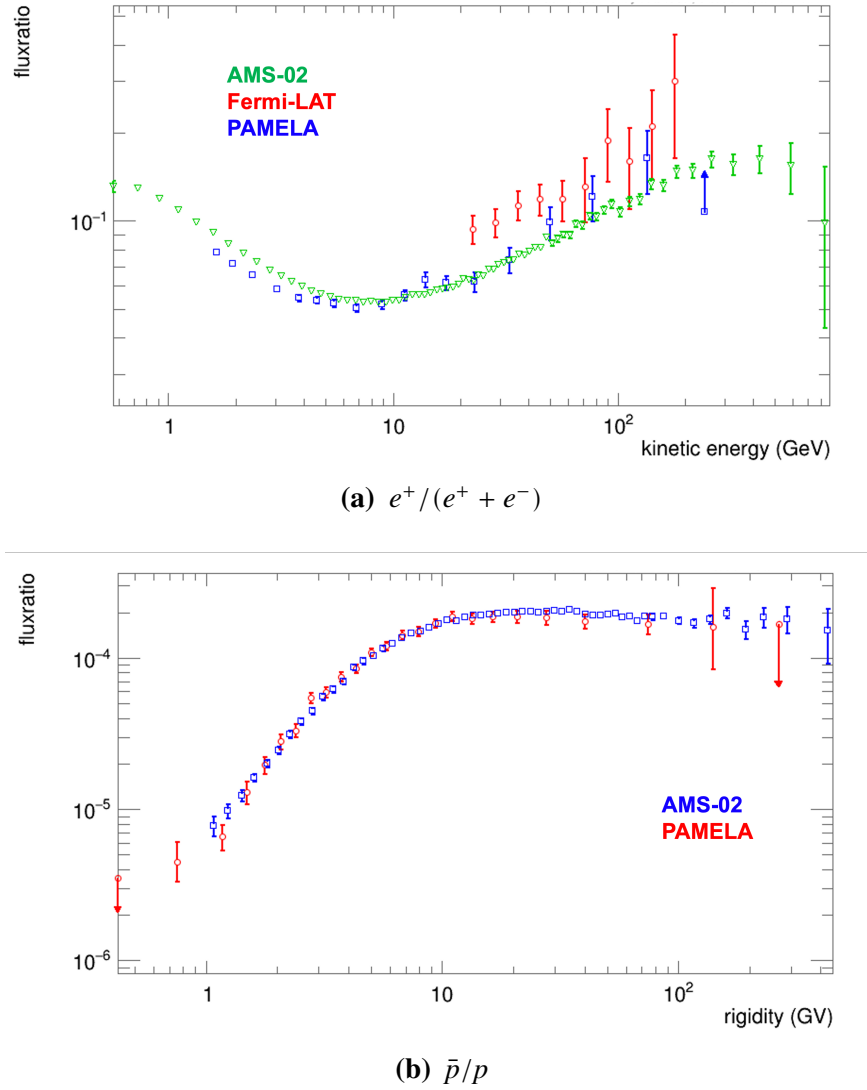


Figure 1.4: antimatter in GCRs; $e^+/(e^+ + e^-)$ flux ratio is shown as a function of kinetic energy while \bar{p}/p flux ratio is shown as a function of rigidity [15].

Spiralling particles along the lines of a magnetic field maintain an angle θ between their velocity and the field \vec{B} that follows the relation $\sin^2 \theta/B \simeq \text{const}$. Then, when B increases, the pitch angle θ increases too and the sin reaches its maximum value of 1 when the motion reflects itself. If the field is static, the kinetic energy of the particle remains unchanged during the reflection. Instead, if the field is slowly moving towards or away the particle, it respectively gains or loses energy. This phenomenon can be seen like a scattering between the particle and the magnetic field irregularities and even if gains and losses are random, they do not completely average themselves, so the overall effect is an acceleration of CRs.

On the basis of where the DSA takes place, it can be identified as a *first* or *second order Fermi process* [19]. The first order includes accelerations occurring in SNe shocks and for every "head-on" encounter, the mean fractional change in energy is of the order of u_s/v , with u_s and v velocities of the shock wave and of the particle. The second order instead involves magnetic fields in interstellar clouds and for those, the mean fractional change in energy is of the order of $(u/v)^2$, where this time u is the velocity of the cloud.

Finally, DSA can explain CRs with energies up to 10^{18} eV but beyond that limit the mechanisms

are still not clear.

1.3.3 Propagation

Propagation of each CRs species can be described by a Fokker-Planck equation [4]:

$$\frac{\partial}{\partial t} \psi(\vec{r}, p, t) = q(\vec{r}, p, t) + \vec{\nabla} \left(D_{xx} \vec{\nabla} \psi - \vec{V} \psi \right) + \\ + \frac{\partial}{\partial p} \left[p^2 D_{pp} \frac{\partial}{\partial p} \left(\frac{\psi}{p^2} \right) \right] - \frac{\partial}{\partial p} \left[\frac{\partial p}{\partial t} \psi - \frac{p}{3} (\vec{\nabla} \vec{V}) \psi \right] - \left(\frac{1}{\tau_f} + \frac{1}{\tau_r} \right) \psi \quad (1.2)$$

with ψ density per momentum units of the considered species.

The equation 1.2 takes into account the distribution of the sources, the diffusion in the galactic magnetic field, the energy losses, the nuclear interactions, the decays and the re-accelerations.

The Local Interstellar Spectrum (LIS) of each species before it enters the solar system can be described by the equation 1.2 with the steady-state assumption $\partial \psi / \partial t = 0$.

The following paragraphs describe the single terms meaning.

Source term q

The source term q includes every contribution that produces particles, i.e. primary sources, spallation and decays.

Primary sources distribution is assumed to be correlated to the density of known sources.

The energy injection spectrum of the source term is modelled with a power law $\partial q / \partial p \propto p^\gamma$ where γ is the CR spectral index that describe the all-particle spectrum.

Diffusive parameters $D_{xx, pp}$

CRs isotropy is due to the diffusion effect given by the interaction with the galactic magnetic field [20].

The field can be split into a regular component, that follows the distribution of the arms of the Galaxy and a turbulent component, that disturbs the first one. The resulting contributions to the CRs propagation are contained in the two parameters $D_{xx, pp}$. A fit to CRs data returns a value of $D_{xx} \sim 10^{28} \text{ cm}^2 \text{s}^{-1}$ at $E \sim 1 \text{ GeV/nucleon}$. Regarding the second parameter, the interaction with the turbulent component can lead to a stochastic re-acceleration of CRs that is modelled with $D_{pp} \propto p^2 \vec{v}^2 / D_{xx}$, where \vec{v} is the Alfvén wave's velocity [21].

Galactic winds convection, $\vec{\nabla} \vec{V}$ terms

Galactic winds are present in many galaxies and they dilute the energy of CRs through an adiabatic expansion. This *adiabatic deceleration* depends on the velocity of the galactic wind \vec{V} itself.

Nuclear processes, $\tau_{f,r}$ terms

$\tau_{f,r}$ indicate respectively the timescales for losses by fragmentation and radioactive decays. The overall effect is a reduction in density by a factor $\Gamma \psi$, with the total lifetime $\Gamma = \tau_f + \tau_r$.

Other energy losses, $\partial(\dot{p}\psi)/\partial p$ term

In addition to the previous contributions, CRs can lose energy by other mechanisms. For instance, protons and nuclei can lose energy by ionisation and electrons and positrons by synchrotron emissions and Inverse Compton losses. All the contributions are included in the $\partial(\dot{p}\psi)/\partial p$ term.

1.4 Propagation in the Heliosphere

CRs entering the Heliosphere are subject to the effect of the Solar Magnetic Field (SMF) and Solar Wind (SW) in a process that is called *solar modulation* that results in an anti-correlation between CRs flux and solar activity. In proximity of the Earth, CRs are deviated by the Earth magnetic field that further modifies the observed spectrum on satellites in Low Earth Orbit (LEO). The interaction of CRs with residual atmosphere in conjunction with the effect of the geomagnetic field creates bands of trapped particles around the Earth, the Van Allen belts, that are an important component of the radiation observed in LEO.

1.4.1 Solar modulation

The Heliosphere is characterized by the presence of the *Solar Magnetic Field (SMF)* and the *Solar Wind (SW)*, a flow of energetic particles ejected by the Sun. In addition, the wind itself generates the *Heliospheric Current Sheet (HCS)*, with a subsequent magnetic field.

CRs propagation inside the Heliosphere is described by the Parker's equation [5]

$$\frac{\partial}{\partial t}f(p; r, t) = \vec{\nabla} \left(K_S \vec{\nabla} f \right) - \vec{V} \vec{\nabla} f - \langle \vec{v}_d \rangle \vec{\nabla} f + \frac{1}{3} \vec{\nabla} \vec{V} \left(\frac{\partial f}{\partial \ln p} \right) \quad (1.3)$$

with $f(p; r, t)$ density of a CR with a specific momentum p , in space (r) and time (t), K_S diffusive component of the drift-diffusive tensor K , \vec{V} speed of the SW, \vec{v}_d drift velocity of the particle due to the gradients and curvatures of the SMF. Then, the terms on the right side of the equation represent respectively the diffusion due to the irregularities of the SMF, the outward convection due to the SW, the drift due to the gradients and the curvatures of the SMF and finally the adiabatic energy losses due to the SW.

Low energetic particles of the CRs spectrum are strongly affected by the solar activity. Specifically, there is an anti-correlation between the solar activity and the CRs intensities, where the activity maximum corresponds to CRs fluxes' minimum and vice versa. This phenomenon is called *solar modulation* (e.g. fig. 1.5).

The following paragraphs describe the approaches used to solve the equation 1.3 and to treat the solar modulation.

Analytical solutions of the transport equation (Force Field Approximation)

The transport equation 1.3 can be solved analytically using the force field approximation originally discussed in [23].

The Force Field Approximation uses a spherical symmetric configuration for the SW where its magnetic irregularities are seen like "scattering centers" for CRs. In this frame, the motion of particles can be described by the equations

$$\frac{\partial U}{\partial t} + \frac{1}{r^2} \frac{\partial}{\partial r} (r^2 S) = -\frac{V}{3} \frac{\partial^2}{\partial T \partial r} \quad S = VU - \kappa \frac{\partial U}{\partial r} - \frac{V}{3} \frac{\partial}{\partial T} (\alpha TU) \quad (1.4)$$

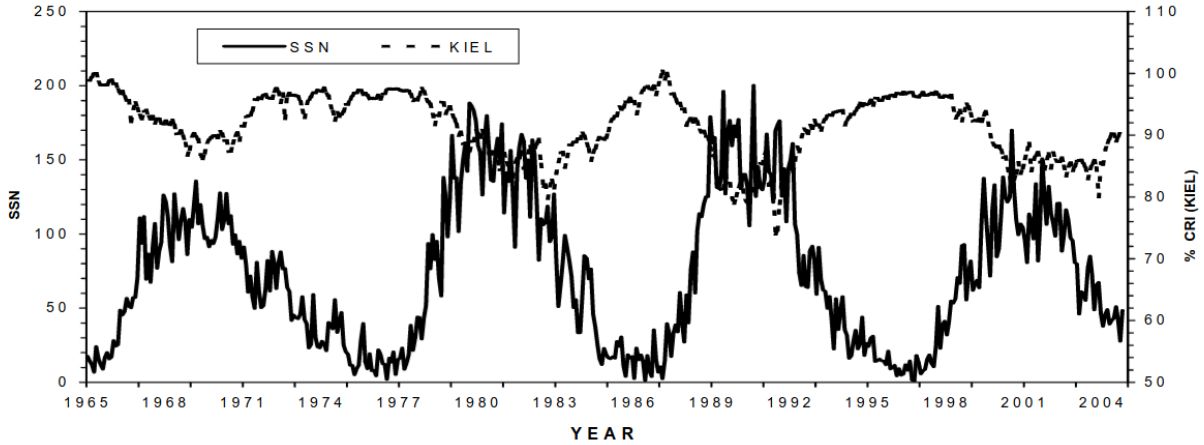


Figure 1.5: comparison of CR intensity collected by Kiel neutron monitor, with Solar Sunspot Number between 1965 and 2004 [22].

where $U(r, T)$ is the differential density and $S(r, T)$ the radial current density of CRs with kinetic energy in $(T, T + dT)$, r the radial distance from the Sun, κ the diffusion coefficient and $\alpha = (E + m)/m$, with m mass of the particle and E its energy.

The Force Field Approximation also considers S negligible and κ separable in its dependencies from r and the rigidity R^* of the particle. With these assumptions, a general solution for the local CRs flux J can be obtained with respect to the interstellar flux J_{IS} :

$$J(E) = \frac{E^2 - m^2}{(E + |q|\phi)^2 - m^2} J_{\text{IS}}(E + |q|\phi) \quad (1.5)$$

with q charge of the particle and ϕ a general parameter to describe the solar modulation. The value of ϕ changes according to the solar cycle, it has the units of a rigidity and it is of the order of 500 MV.

Numerical solutions of the transport equation (Stochastic Differential Equations)

The transport equation 1.3 can be solved numerically as well. However, the complexity of the equation makes the numerical models more unstable as their dimensionality increases. The current approach to overcome these problems is using *Stochastic Differential Equations (SDEs)*. SDEs introduce random parameters in the original equations, making their solving a stochastic process where a grid of values of the parameters has to be scanned.

Numerical models are much more effective than analytical ones as they can adapt very well to the experimental data. However, the increase of the predictive power comes at the expense of understanding the underlying physical phenomenon.

To conclude, solar modulation is studied using both methodologies, so the development of analytical models will improve the physical understanding which in turn can bring to an improvement in the numerical models and vice versa.

*i.e. $R = p/Ze$.

1.4.2 Geomagnetic field

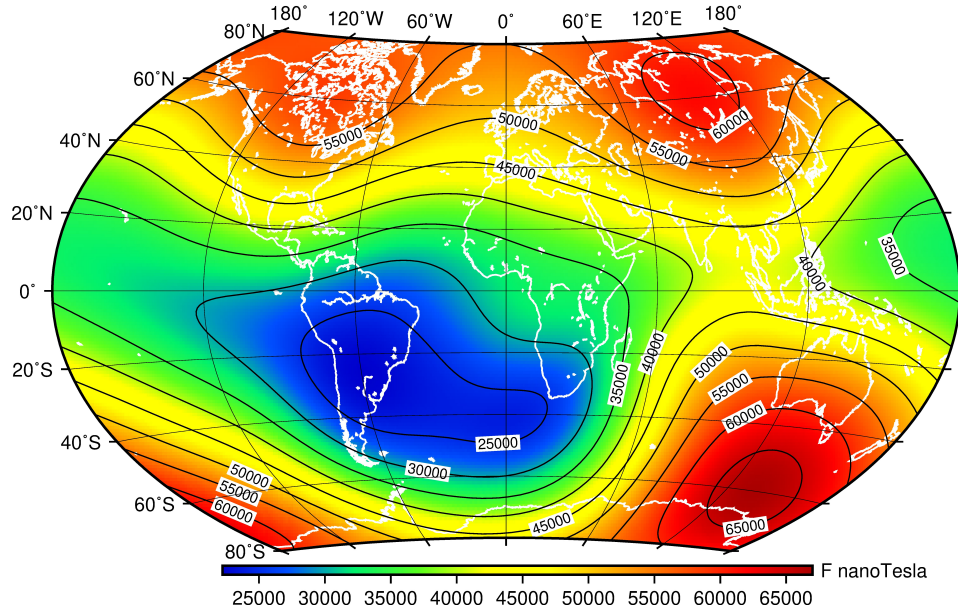


Figure 1.6: total intensity of the geomagnetic field in 2020 at Earth surface [24].

The geomagnetic field can be described as a dipole field with an offset and a tilt. The momentum of the dipole is $M = 8.1 \cdot 10^{25} \text{ G cm}^3$, the tilt is of 11° in respect to the rotation axis of the Earth and the offset is of about 400 km in respect to the center of the Earth. In this description the field has the components

$$B_r = -\frac{2M}{r^3} \sin \lambda \quad B_\lambda = \frac{M}{r^3} \cos \lambda \quad (1.6)$$

where λ is the magnetic latitude and the field lines follow the form $r \propto \cos^2 \lambda$. All previous properties are not constant over time and they change in a non-uniform way, so it is necessary to monitor and update them.

Low-rigidities particles are strongly curved by the geomagnetic field, that is capable of trapping them in the *Van Allen belts*. Because of that, every position near Earth can be characterized by a specific allowed minimum value of rigidity, the *rigidity cutoff*.

Van Allen belts

The geomagnetic field can trap charged particles along its lines. This phenomenon gives rise to the presence of the *Van Allen belts* [25], belts of trapped particles that spiral within the field until they are reflected while approaching the magnetic poles. Ultimately, the particles keep moving back and forth with no possibility of escape.

Two main belts have been observed between 640 and 58000 km of altitude: an inner belt populated by protons and electrons and an outer belt mainly populated by solar particles, specifically electrons. The inner belt particles are produced by neutrons decays, produced in turn by the interaction of CRs with the atmosphere. This belt has a quite stable center, especially to protons, with a slight westward drift, while, at its lower edge, intensities can vary up to a factor of 5. The outer belt shows variations by a factor between 6 and 16 during the day. Beyond the two permanent belts, transient ones could be temporarily created.

Solar activity and consequent magnetic storms can influence the populations of the belts [26]. During magnetic storms, average fluxes can be increased up to 2 or even 3 orders of magnitude and particles with low energies can penetrate inner regions. Specifically, a higher solar activity is connected to lower protons and higher electrons intensities.

Rigidity cutoff

The *rigidity cutoff* is the minimum value of rigidity that a particle has to have to reach a certain position, based on the action of the geomagnetic field. The rigidity cutoff was evaluated analytically for the first time by Stöermer using the dipole approximation [27, 28], obtaining that

$$R_C = \frac{M}{r^2} \frac{\cos^4 \lambda}{\left(1 + \sqrt{1 - \text{sign } q \sin \theta \cos \phi \cos^3 \lambda}\right)^2} \quad (1.7)$$

with M magnetic momentum of the dipole, λ and r respectively the magnetic latitude and the radial distance from the center of the dipole, θ and ϕ the polar and azimuthal angles of the arrival direction of the particle in respect to the local zenith and q the charge of the particle.

An interesting case is when the arrival direction of the particle is vertical. In that case, the azimuthal dependence vanishes and the vertical rigidity cutoff reduces itself to

$$R_{VC} = \frac{M}{4r^2} \cos^4 \lambda \quad (1.8)$$

The vertical rigidity cutoff is maximum at the geomagnetic equator, about 15 GV and null at the magnetic poles.

Another parameter related to the rigidity cutoff was defined by McIlwain in [29] as

$$L = \frac{r}{\cos^2 \lambda_m} \quad (1.9)$$

with r radial distance from the center of the Earth and λ_m magnetic latitude. Shea and others [30] established the simple relation

$$\frac{L}{R_{\text{Earth}}} = \sqrt{\frac{k}{R_C}} \quad (1.10)$$

with $k \approx 16.2$ GV, R_{Earth} radius of the Earth. Therefore, R_C and L can be used equivalently to identify similar areas in the Earth orbit for CRs detection.

1.5 Detection

Depending on their energy CRs can be detected efficiently with different experimental techniques. At energies below the knee, the abundance of CRs allows for the direct measurement by the use of apparatus that can be flown in stratospheric balloons or in space. At higher energies the required sensitive areas are too big for operation in high-atmosphere or on a satellite and the only viable option is the indirect measurement of the CRs interaction on atmosphere products using large area experiments built on ground.

Therefore, CRs experiments can be grouped into three main categories: ground experiments, balloon experiments and space experiments. These types are described in the following sections, reporting some relevant examples.

The work presented in this thesis makes use of data acquired by the Alpha Magnetic Spectrometer, currently operating on the ISS, that is treated in detail in chapter 3.

1.5.1 Ground experiments

CRs with energies above hundreds of TeV need to be studied using detectors with large surfaces and long data taking times to get statistically significant results. Build and maintain large experiments in space or at high altitudes is often not feasible, therefore ground experiments are still considered the preferred way to study the most energetic CRs.

When CRs enter the atmosphere they start interacting with the medium, producing an *extensive air shower* of secondary particles, some of which can reach the ground. At that level typically, the local density of the shower is measured using an array of scintillators. Then, the position of core of the shower and its total number of particles can be obtained. The energy of the shower is estimated using the number of particles and with just a few hundreds of detectors it is possible to collect events between 10^{15} and 10^{18} eV. This procedure is simple but effective and is usually combined with other techniques.

Another technique uses Cherenkov light detectors made of water tanks. In this case, the passage of the particle in the tank emit light that is measured using photomultipliers (PMTs). This procedure is more sensitive to showers with bigger zenith angles and has a wider sky coverage. The most representative example of this kind of experiments is the *Pierre Auger Observatory* [31], the largest ground-based experiment built so far. This arrangement allows also to detect horizontal showers of highly energetic neutrinos, as proved by the *IceCube Neutrino Observatory* [32, 33]. Another facility that will use the Cherenkov light to measure high-energy neutrinos is the *Cubic Kilometre Neutrino Telescope (KM3NeT)* [34, 35]. The IceCube observatory uses the ice at the South Pole as Cherenkov radiator while KM3NeT will use the water of the Mediterranean Sea for the same purpose.

Other experiments detect Cherenkov emissions of charged particles through the atmosphere using parabolic antennas and PMTs or silicon photomultipliers (SiPMs). In this case, usually photon initiated showers with energies of the order of TeV are meant to be measured. The *Cherenkov Telescope Array (CTA)* uses this kind of detectors [36, 37].

Finally, particles with energies above 10^{17} eV can excite nitrogen molecules in the atmosphere, causing emissions of fluorescence light that can be detected using instruments similar to the ones used for Cherenkov emissions. Differently from Cherenkov detectors, in this case the measurement requires a cloudless sky, moonless nights and well known atmospheric conditions, so it is much more difficult taking data. For instance, the Pierre Auger Observatory operates fluorescence detectors together with its Cherenkov water tanks [31].

1.5.2 Balloon experiments

Balloon experiments are largely used to study CRs. They are cheaper than space experiments but as those they can detect primary particles. The main difficulty of this kind of experiments is the need to model precisely the residual atmosphere the CRs interact with.

Before the space age, balloon experiments were the only way to detect primary particles, so many discoveries has been done with them in the past. Anyway their affordability keep making them appreciated in contemporary CRs research.

Examples of balloon experiments are the *General AntiParticle Spectrometer (GAPS)* [38] and the *High Energy Light Isotope eXperiment (HELIX)* [39].

1.5.3 Space experiments

Initially space experiments were used only to study cosmic electromagnetic radiation and the geomagnetic field. Then, the first orbiting experiments for CRs have proved that the technology of modern particle physics can be setup and used in space as well.

The first space experiment that tested the feasibility of CRs detection in space has been the *Alpha Magnetic Spectrometer (AMS)* with the test flight of AMS-01 [40]. Other examples of this type of experiments are the *Payload for Anti-Matter and Light-nuclei Astrophysics (PAMELA)* [41], the *Fermi Gamma-ray Space Telescope* [42–44], and the *DArk Matter Particle Explorer (DAMPE)* [45]. PAMELA was decommissioned in 2016, while Fermi, AMS and DAMPE are still taking data. The following paragraphs describe these experiments. In particular, chapter 3 is dedicated to describe the AMS detector. In addition to the already cited experiments, a final paragraph is dedicated the next generation detectors that have been proposed or are currently under development.

Payload for Anti-Matter and Light-nuclei Astrophysics (PAMELA)

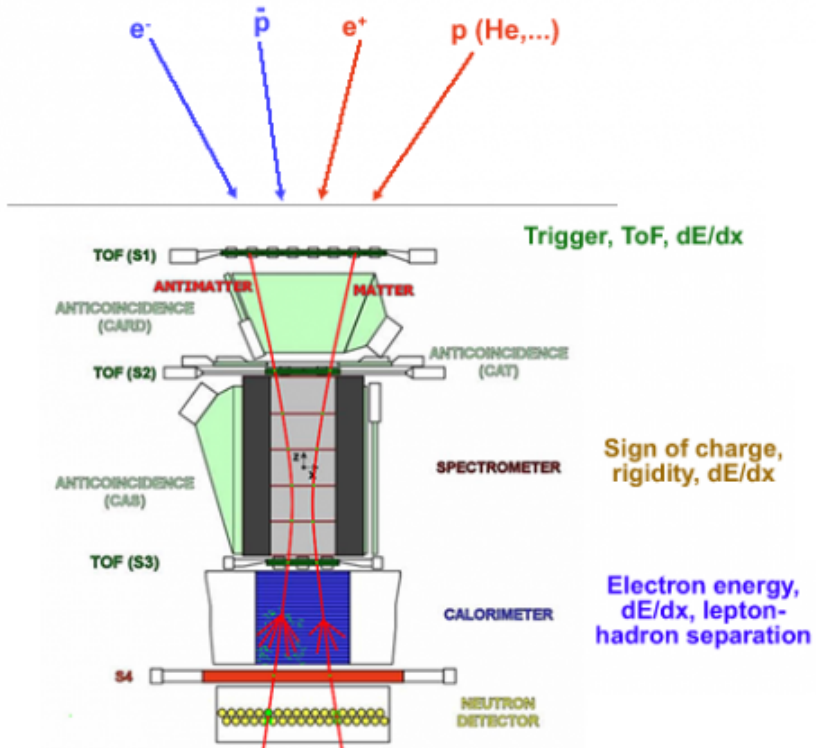


Figure 1.7: PAMELA detector [46]; the captions on the right side show which measurements are done using each one of the sub-systems.

PAMELA operated between 2006 and 2016, when the host satellite was decommissioned [41]. The detector was composed by a time of flight system, a magnetic spectrometer, plastic scintillators anti-counters, a calorimeter and a neutron detector. The image 1.7 shows a view of the instrument.

The most important results reached by PAMELA are the observed excess in the e^+/e^- ratio starting at 50 GeV [47] and the break measured for the spectral index of protons and helium nuclei before the spectrum knee, which is not compatible with a smooth power law for all the species up to knee [48].

Fermi Gamma-ray Space Telescope

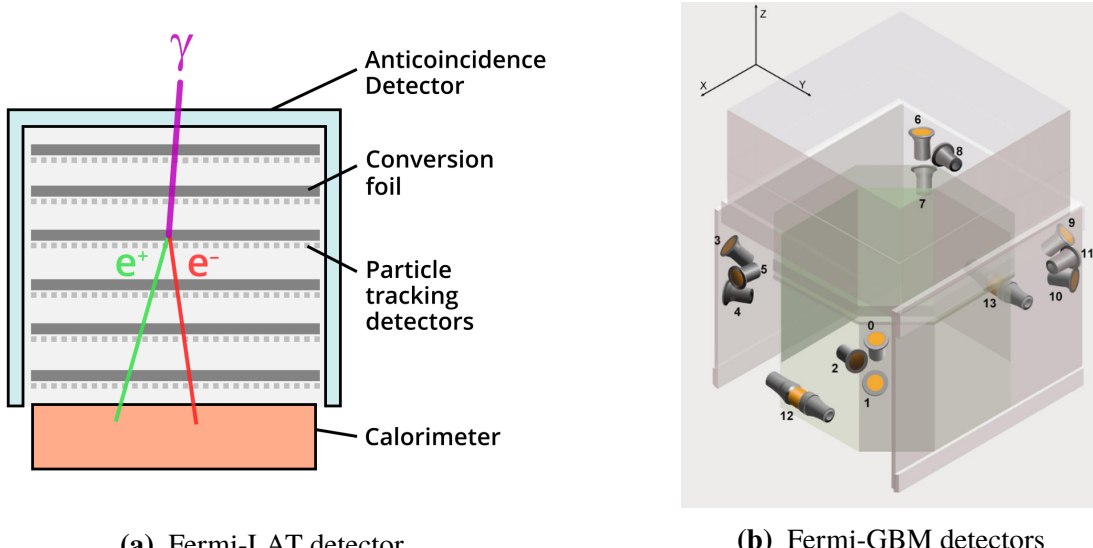


Figure 1.8: schematic view of the Fermi telescope [42, 44].

The Fermi telescope is intended to study cosmic photons and it is composed of two sub-detectors: the *Fermi Large Area Telescope (Fermi-LAT)* [43] and the *Fermi Gamma-ray Burst Monitor (Fermi-GBM)* [44]. The figure 1.8 shows a view of the two systems.

Fermi-LAT is the main system of the satellite and it is composed by a silicon-tungsten tracker-converter, an electromagnetic calorimeter and an Anti-Coincidence Detector (ACD). The tracker has the function to convert photons to e^\pm pairs and track them, while the calorimeter measures their energy. The ACD is used to reject charged particles entering the apparatus and it is composed of plastic scintillators. The Fermi-LAT is able to detect photons between 30 MeV and 300 GeV and has a field of view of over 2 sr.

The Fermi-GBM is an auxiliary instrument and is used to detect Gamma-Ray Burst (GRB). The system is composed of 12 sub-detectors made of sodium iodide and 2 made of bismuth germanate. The former ones are used to catch X-rays and low-energy γ -rays, the latter to catch γ -rays with higher energies. Ultimately, the Fermi-GBM covers a range between 8 keV and 30 MeV, extending the lower boundary of the energies detectable by the Fermi-LAT.

DArk Matter Particle Explorer (DAMPE)

DAMPE was launched in 2015 and orbits at 500 km of altitude [45]. Its main goal is to look for Dark Matter signatures measuring high energy photons, electrons and positrons.

The instrument is composed by a Plastic Scintillator Detector (PSD), a Silicon-Tungsten tracKer-converter (STK), an electromagnetic calorimeter (BGO calorimeter) and a NeUtron Detector (NUD). The STK converts photons to e^\pm pairs and track them. The calorimeter is made of bismuth germanate and measures the energy of particles. The figure 1.9 shows a schematic view of the system.

The instrument can detect electromagnetic particles (i.e. γ , e^\pm) with energies between 5 GeV and 10 TeV and protons and nuclei with energies from 50 GeV up to 100 TeV.

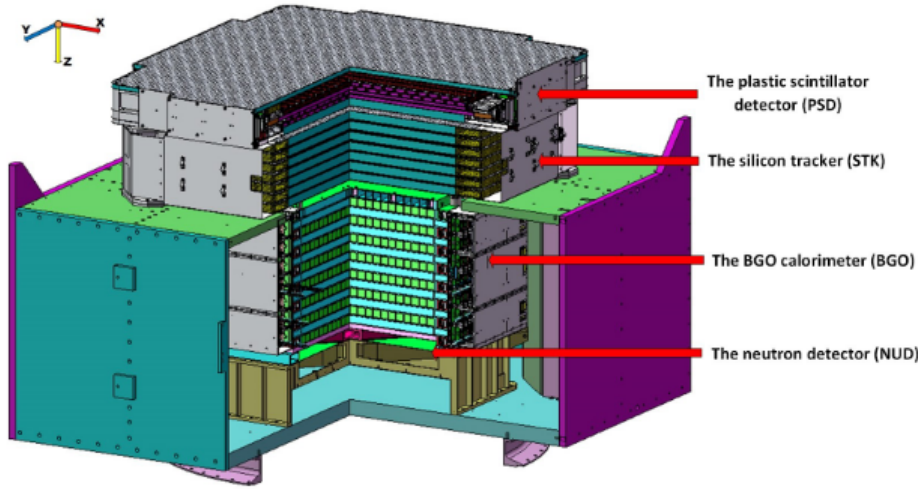


Figure 1.9: schema of DAMPE detector [45].

Alpha Magnetic Spectrometer (AMS)

A test flight was arranged in 1998 on the Discovery Space Shuttle during the STS-91 mission to test the feasibility of operating a large-scale particles detector in space. The instrument flown, known as *AMS-01* [40], was a prototype of the following one, *AMS-02*. *AMS-01* flight achieved many results, e.g. positrons, protons and helium fluxes, search for anti-helium [50].

AMS-02 is mounted on the ISS and it has been taking data since 2011. The end of operations of AMS has been delayed multiple times and currently it seems the detector will be kept operative until the decommission of the ISS itself, planned for 2031.

AMS instrument is composed by a magnetic spectrometer, which gives it its name, a Time-of-Flight (ToF) detector, a series of Anti-Coincidence Counters (ACC), a Transition Radiation Detector (TRD), a Ring Imaging Cherenkov (RICH) detector and an Electromagnetic Calorimeter (ECAL). The magnetic spectrometer in particular is composed of silicon tracker immersed in the field of a permanent magnet. The figure 1.10 shows a schematic view of the entire detector with the measurements that can be performed with each sub-system.

The performances reached by AMS are the best one ever reached with a magnetic spectrometer and it can detect particles with rigidities up to the TV.

Chapter 3 is dedicated to a detailed treatment of the AMS detector.

Next generation detectors

The next generation detectors differ from the previous ones mainly because of their structure. To increase the statistics, the proposed instruments span a larger solid angle, hence the name of 4π experiments. Examples of this kind of detectors are the *Antimatter Large Acceptance Detector In Orbit* (ALADInO; fig. 1.11) [51], the *High Energy cosmic-Radiation Detection* facility (HERD; fig. 1.12) [52] and the *Alpha Magnetic Spectrometer 100* (AMS-100; fig. 1.13) [53].

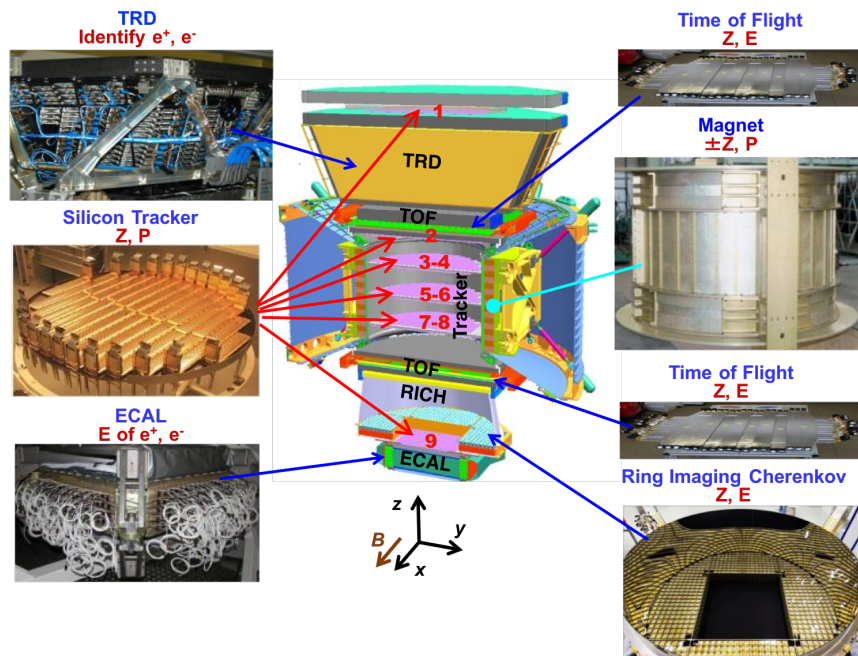


Figure 1.10: AMS-02 detector [49]; captions on both sides show which measurements can be done using each one of the sub-systems.

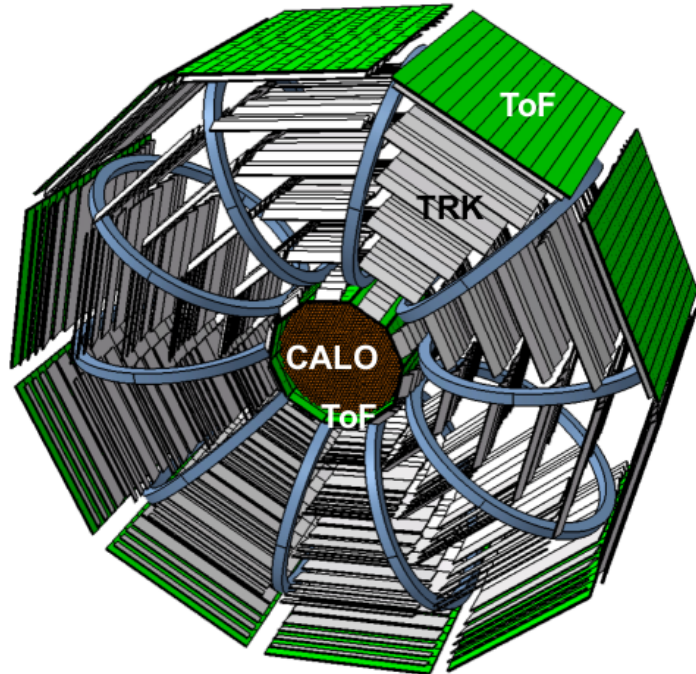


Figure 1.11: the Antimatter Large Acceptance Detector In Orbit (ALADInO) [51].

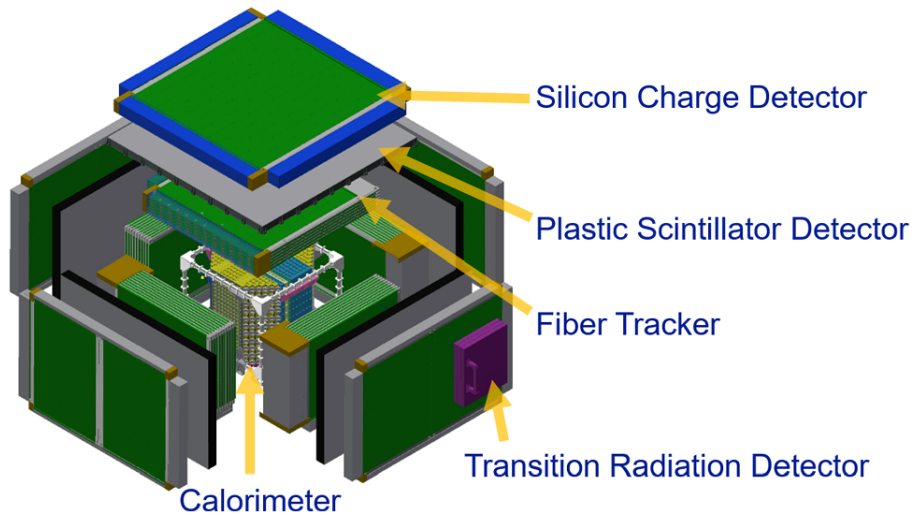


Figure 1.12: the High Energy cosmic-Radiation Detection (HERD) [54].

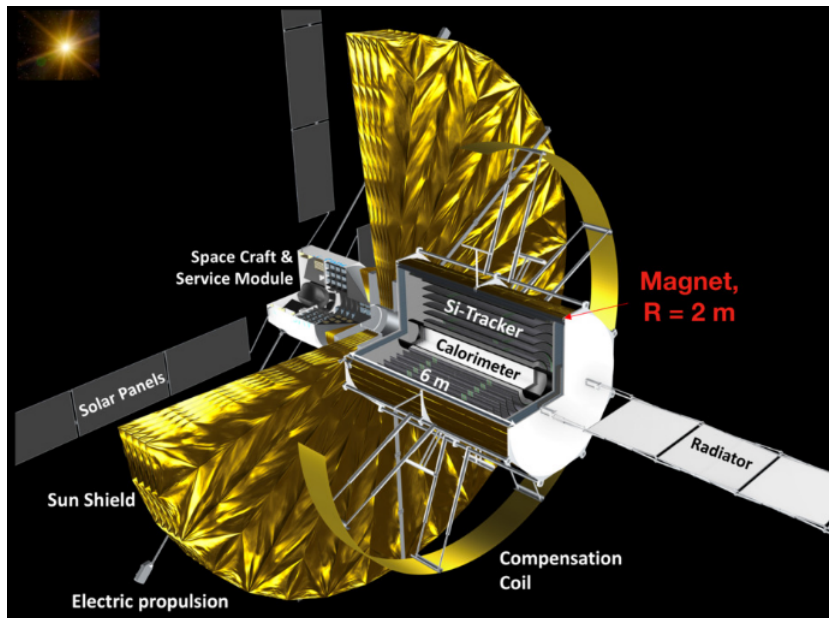


Figure 1.13: the Alpha Magnetic Spectrometer 100 (AMS-100) [53].

Chapter 2

Solar Energetic Particles

The energy generation and heating processes taking place in the Sun create convection and differential rotation of the outer solar plasma. The movement of these ionized particles creates the *Solar Magnetic Field (SMF)*, which gives rise in turn to all the main phenomena that form the solar activity. The solar activity can accelerate and eject flows of particles into the Heliosphere as *Solar Wind (SW)*.

SEPs are bursts of high-energy particles from the Sun that can last for hours or even days. They cover an energy range that goes from about 10 keV up to several GeV, with a maximum β of 0.9. Their composition is dominated by protons and electrons but also heavier elements from He to Au and Pb have been measured. SEP events can be categorized as impulsive or long-duration/gradual events. The two types show different properties in their composition and duration and in particular the relative abundances of elements and isotopes can effectively identify the different origins of acceleration and interplanetary transports.

2.1 Structure of the Sun

The Sun consists of a gaseous and ionized plasma with a total mass of $1.989 \cdot 10^{33}$ g. Figure 2.1 shows a scheme of its structure.

The inner *core* reaches temperatures of $15 \cdot 10^6$ K at which protons can tunnel the Coulomb barrier and penetrate H, C and N nuclei. The nuclear reactions taking place in this region catalyse the He synthesis. The energy released by the reactions is radiated outward and reabsorbed during its diffusion in the *radiative zone*; there, heat and pressure are produced, with an overall effect of balancing the tendency of the star to collapse because of the gravitational forces.

In the *convection zone* the plasma circulates and gives energy to the *photosphere* surface, where photons can pass freely into the upper layers. In some parts the photosphere cools down from ~ 5800 to ~ 4500 K. In these regions, characterized by a strong magnetic field, *sunspots* can be observed (see fig. 2.2). At those temperatures, elements with a First Ionization Potential (FIP) greater than 10 eV (e.g. $FIP_H = 13.6$ eV) can capture the electrons they miss and neutralise themselves.

The *tachocline* separates the radiative and convective zones; there the Sun stops rotating as a rigid body. In the convective zone in fact the plasma rotates faster at the equator than at the poles. The sidereal period is of 24.47 days at the equator and rises by 25% at the latitude of 60° .

In the *chromosphere*, above the photosphere, the electron temperature is kept at about 6000 K for a distance of more than $2 \cdot 10^6$ m. Arrived at the boundary with the solar corona, the electrons density falls from 10^{11} to 10^9 cm $^{-3}$ with an increase of temperature to reach 10^6 K [57].

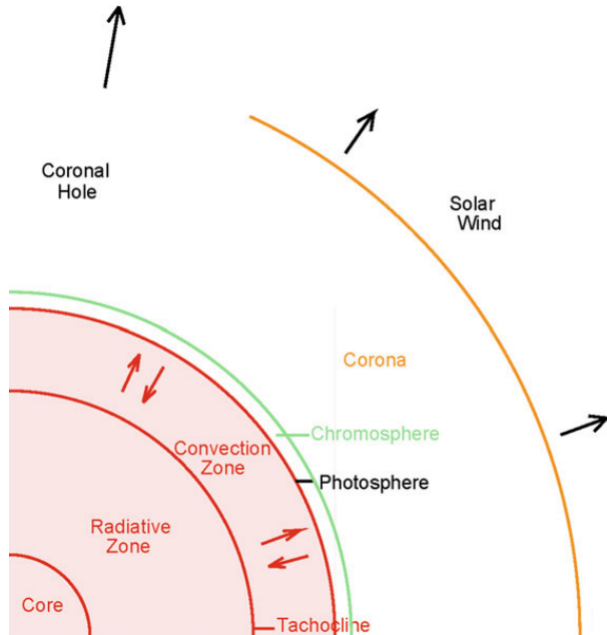


Figure 2.1: cross section of the Sun from its core to the external regions [55]. The flows of ejected solar plasma into the Heliosphere are shown as well.

The solar *corona* extends for about a solar radius and is heated by numerous nanoflares [58], small sites of magnetic reconnection and by absorption of Alfvén waves created in the turbulent layers below [21]. The corona is largely contained by rising closed magnetic loops and its outer layer evaporates into the SW.

The *coronal holes* are temporary dark regions visible in the extreme ultraviolet spectrum where the SMF extends into the interplanetary space as an open field (see fig. 2.3). Their plasma show a lower temperature and density and thanks to the open field the SW escaping from those areas have a greater average velocity.

2.2 Solar Magnetic Field

In quiet times the Solar Magnetic Field (SMF) is well described by a dipole (see fig. 2.6a) [60, 61]. The rotational shear at the tachocline produces fields of 0.2–0.3 T that form Ω -loops through the convection zone and the photosphere [62] (see fig. 2.4). The emerging and re-entering field lines produce *active regions* visible as sunspots on the photosphere. Active regions appear usually at mid-latitudes, where the effect of differential rotation is greater.

Magnetic field loops can reach very far distances from the Sun, frozen into the CMEs and the SW.

The polarity of the SMF inverts about every 11 years. Minima of the solar activity coincide with the maximum alignment between the field and the rotation axes. During those periods, the number and size of active regions are largely reduced. Maxima of the solar activity instead occur during the reversal phases. Following this periodicity, a solar cycle covers a period of about 11 years. Figure 2.6 shows the magnetic field during solar minimum and a reversal period; Fig. 2.5 shows the yearly SSN and the average polar field for 4 solar cycles.

The SMF variability originates several phenomena:

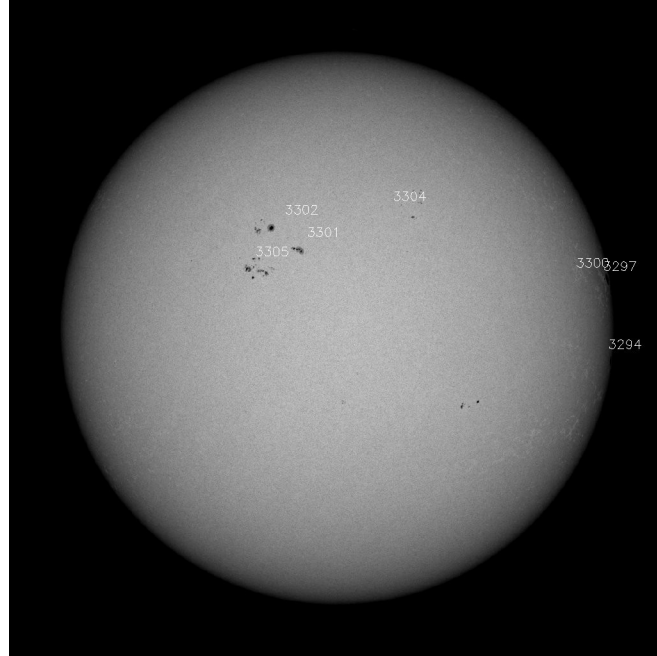


Figure 2.2: sunspots imaged by the Michelson Doppler Imager (MDI) of the Solar and Heliospheric Observatory (SOHO) on May 14, 2023 [56]. The sunspots are visible as dark areas in the photosphere and are reported with their identifier.

- closed loops can lead to sudden heating and X-rays emission in their *footpoints*^{*}, where the plasma is denser, by electron Bremsstrahlung [65];
- reconnection of oppositely directed fields in the corona can produce SEPs, mainly electrons [66];
- reconnection of open field lines can cause coronal jets with the release of electrons and ions into space, generating an impulsive SEP event [6].

2.3 Solar Plasma

The Sun emits continuously a stream of ionized particles propagating into the SMF. The different regimes of this plasma are defined by β_P , i.e. the ratio of thermal and magnetic energy densities:

$$\beta_P = \frac{8\pi\rho k_B T}{B^2} \quad (2.1)$$

where ρ and T are the density and the temperature of the plasma, k_B the Boltzmann constant and B the magnetic field intensity. When $\beta_P < 1$, the magnetic field dominates over the plasma, and its particles are confined in magnetic flux tubes with no possibility of escape. When $\beta_P > 1$, the plasma dominates and its turbulences distort the magnetic field which becomes more variable.

CMEs and most of the solar corona are characterized by a $\beta_P < 1$. The β_P increases along the corona and when it exceeds 1, typically 2 solar radii from the Sun, particles are no more bounded and can expand freely, forming the SW and opening the magnetic field lines.

*i.e. the region where magnetic field lines reach the photosphere, closing a loop.

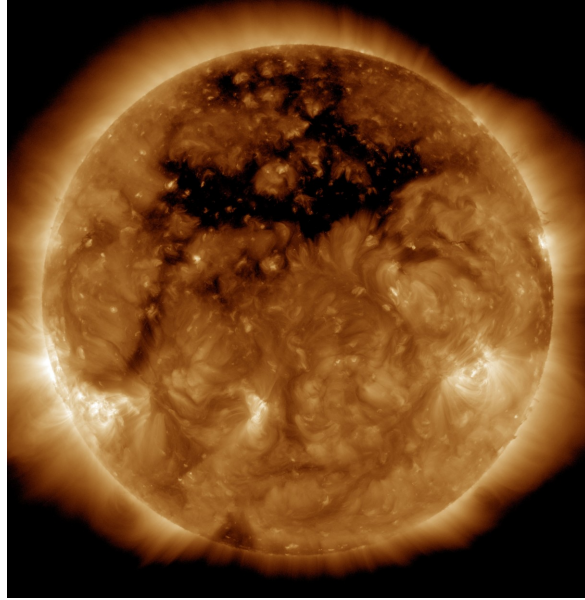


Figure 2.3: coronal hole imaged at 193 Å on Oct. 10, 2015 by the Solar Dynamic Observatory (SDO) of NASA [59]. The coronal hole is visible on top of the Sun as a large dark area.

2.4 Heliosphere

The *Heliosphere* is the region of the interplanetary space where the influence of the Solar Wind predominates over that exerted by the ISM.

The *Solar Wind (SW)* is an almost radial flow of plasma and magnetic field that expands into the Heliosphere with a velocity between 400 and 800 km/s [67]. In the inner Heliosphere, the plasma density and magnetic field are approximately proportional to r^{-2} , with r being the radial distance from the Sun. At 1 AU, the magnetic field dependence with radial distance is better approximated by $r^{-1.5}$ [68, 69]. Magnetic field and plasma density values found near Earth are $B \sim 10$ nT and $n_e \sim 10$ cm $^{-3}$. Plasma carried by the SW takes 4.3 days to reach Earth, a shock wave one day, a 10 MeV proton and a 5 keV electron one hour and a photon 8.3 minutes. Thus, accelerated particles reach Earth long before the shock that originates them.

During solar minima the Heliosphere conditions are stable. In these periods the magnetic field lines are almost radial and high-speed SW comes out from the coronal holes (i.e. 700–800 km/s). Hemispheres with field lines of opposite polarities are separated by a current sheet, the *Heliospheric Current Sheet (HCS)*, that extends throughout the Heliosphere from the Sun's equator. The HCS and the magnetic field lines form a spiral pattern due to the Sun rotation called *Parker spiral* [70], shown in Fig. 2.7.

2.5 Coronal Mass Ejections

Magnetic reconnections in the solar corona can lead to the ejection of large filaments of plasma with masses of $10^{14} - 10^{16}$ g, energies of $10^{27} - 10^{32}$ erg, accompanied by helical magnetic field lines [72]. These ejections are named *Coronal Mass Ejections (CMEs)* and carry most of the energy in solar eruptions; their velocity can go from the ones typical of the SW (i.e. 400–800 km/s) up to 3000 km/s. Figure 2.8 shows pictures of a CME event taken by Large Angle and Spectrometric CORonagraph (LASCO) C2 and C3 instruments of the SOHO.

Filaments are irregular, linear structures of cool, dense, chromospheric plasma lying parallel to

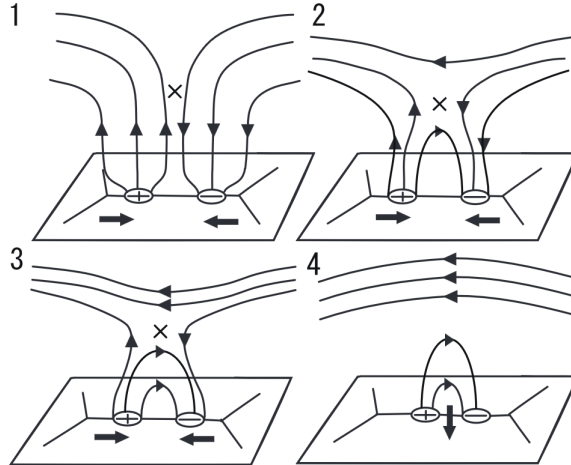


Figure 2.4: the Ω -loop submergence model [62]. In panel 1, two anti-parallel magnetic fluxes converge creating the loop. Then, magnetic reconnection occurs above the photosphere as the fluxes converge (panels 2 and 3). When the magnetic tension becomes stronger than the magnetic buoyancy due to the convergence, the magnetic loop begins to submerge (panel 4).

the solar surface [74]. They can be seen as dark regions in H α images and when they project the solar limb they are called *prominences*. Filaments are often ejected at the core of CMEs, usually with an associated flare. When no flare is emitted, signatures can be found by observing the solar surface and the lower corona. Fast and wide shock waves CMEs driven are an effective source of acceleration for long-duration SEP events [7].

CMEs theory and modelling have been treated in detail in [75].

2.6 Solar Energetic Particle events

Reconnection of field lines in the high corona can produce a jet of electrons and ions that is released into space [6]. At those altitudes the plasma is almost collisionless, therefore particles do not lose the earned energy by Coulomb interactions. After being produced, particles move along the field lines and reach the footpoint of the loop where they find a more dense ambient. There, the particles start to interact and lose energy, emitting photons and producing a solar flare that can be observed. However, the detection of the flare shows the site in the low corona where the SEPs die, not where they have been originally accelerated in the high corona. These types of events are characterized by shorter time durations and are called *impulsive SEP events*.

The solar corona is crossed by Alfvén waves produced in the turbulent layers beneath [21]. Alfvén waves propagate with the group velocity

$$v_A = \frac{B}{\sqrt{4\pi\rho}} \quad (2.2)$$

with B magnetic field intensity and ρ plasma density. Equation 2.2 can be used to determine when a CME is capable of accelerating a SEP; in fact, CMEs can effectively produce SEPs only when their velocity is greater than v_A [7, 76]. In correspondence of an active region, v_A decreases with height, reaching a value between 200 and 500 km/s at $1.5 R_S$ (R_S solar radius), rising again to a maximum of ~ 750 km/s at $4 R_S$ and finally decaying with r^{-1} . At Earth distance, $v_A \approx 30$ km/s. CMEs accelerated SEPs are characterized by longer time durations, hence the name *long-duration* (or *gradual*) *SEP events*.

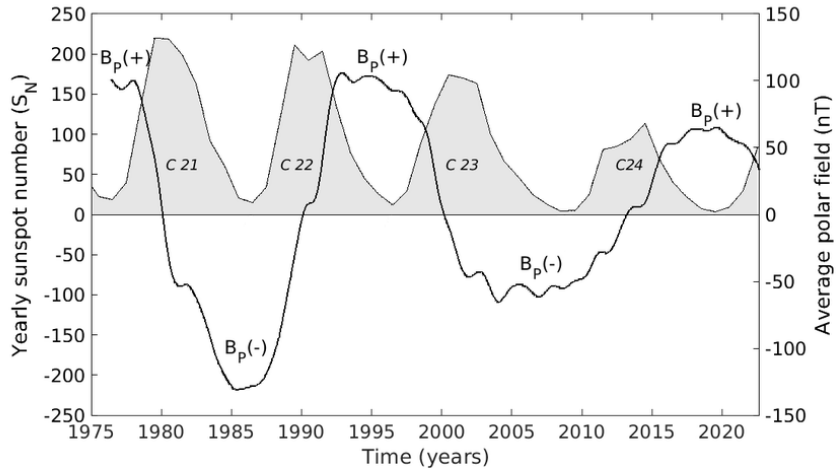


Figure 2.5: temporal evolution of yearly SSN and average polar field during solar cycles 21–24 [63]. The sign of the average polar field defines the polarity of the magnetic field. Data source of SSN is the World Data Center (WDC) of the Sunspot Index and Long-term Solar Observations (SILSO); data source for the magnetic field intensities is the Wilcox Solar Observatory (WSO).

The two classes for SEP events show differences in their elements and isotopes abundances, electron/ion ratios, energy spectra, duration, angular distributions and accompanying phenomena. Figure 2.9 shows a scheme of SEP events types with the corresponding production mechanism.

SEP production has been treated in [7, 78, 79].

2.7 Composition of Solar Energetic Particles

Elemental and isotopic abundances are indicators of the origin, acceleration, and transport of SEPs.

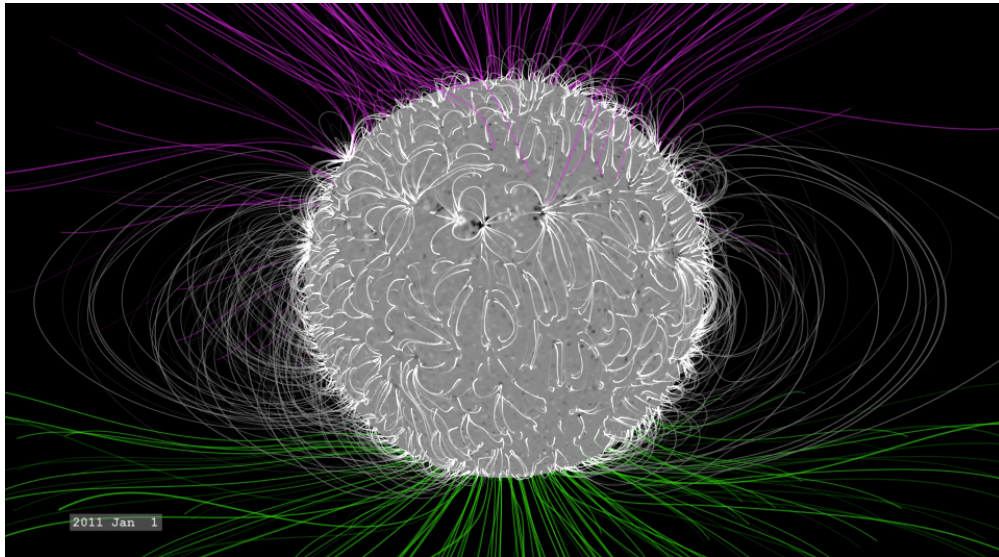
The average element abundances of long SEP events are a measure of the corresponding solar coronal abundances [80, 81]. Figure 2.10 shows long-duration SEP events composition compared to the one measured in the photosphere.

Impulsive SEPs show peculiar properties with respect to the SW composition. The Solar wind has a ${}^3\text{He}/{}^4\text{He}$ ratio of about $5 \cdot 10^{-4}$ while SEPs have a value above 1 for the same ratio. Other elements show a power law in the mass-to-charge ratio that becomes a 1000-fold enhancement for heavy elements up to Au and Pb, ratioed on He or O [83]. Impulsive SEP events have also intense electron beams capable of emitting type III radio bursts [84, 85].

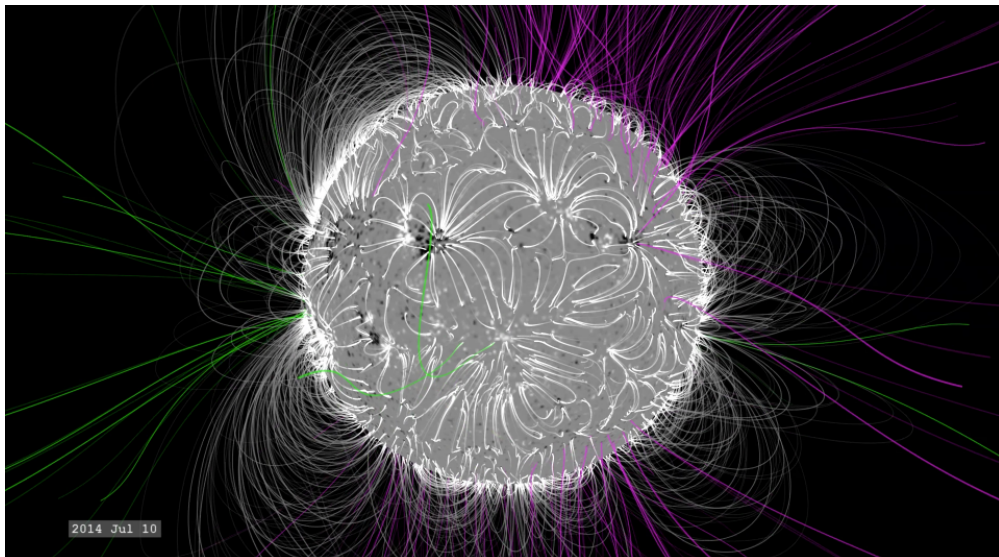
In the photosphere, elements with a FIP under 10 eV are ionized and subject to the Alfvén waves in their transport between the chromosphere and the corona. The neutral atoms instead do not interact with the waves, but at lower altitudes of the corona, where the temperature is above 10^6 K, all elements are ionized. Therefore, Alfvén waves below the chromospheric-coronal limit are the predominant boosting process of low-FIP ions (e.g. Mg, Si, Fe) into the corona, over the slower evaporation of high-FIP neutral atoms (e.g. O, Ne, He) [86]. For closed magnetic loops, Alfvén waves can resonate with the loop length, constraining ions fractionation to occur only at the top of the chromosphere; open fields lack this kind of resonance, so their fractionation is more extensive.

The measurement of SW abundance confirms the different origins of SEPs, despite the similar FIP effect present in both of them [87–89]. In fact, SEPs arise mainly on closed loops in active regions, so that P, S and C are suppressed like high-FIP neutral atoms, while the SW arises on

open field lines, where the same elements behave like low-FIP ions [90]. Therefore SEPs and SW's particles result in samples of different coronal material.



(a) January 1, 2011



(b) April 15, 2014

Figure 2.6: the SMF during solar minima and maxima[64]. Panel (a) shows the field lines 3 years after a solar minimum; (b) shows the field lines about 1 year before a solar maximum. In both panels, open magnetic field lines are colored differently for different polarities.

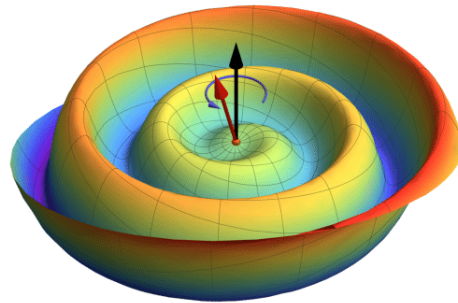


Figure 2.7: shape of the Heliospheric Current Sheet in a Parker Solar Wind model [71].

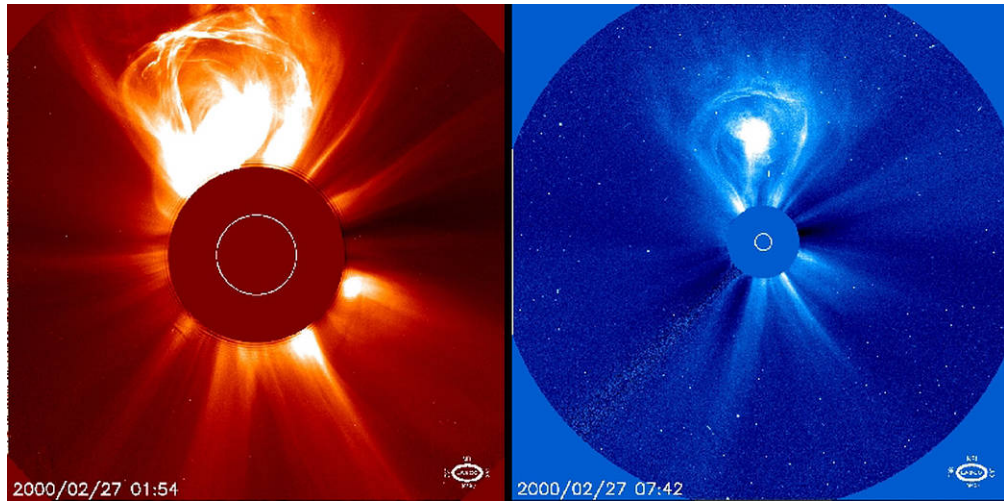


Figure 2.8: pictures of a CME event taken by SOHO LASCO C2 and C3 on February 27, 2000 [73].

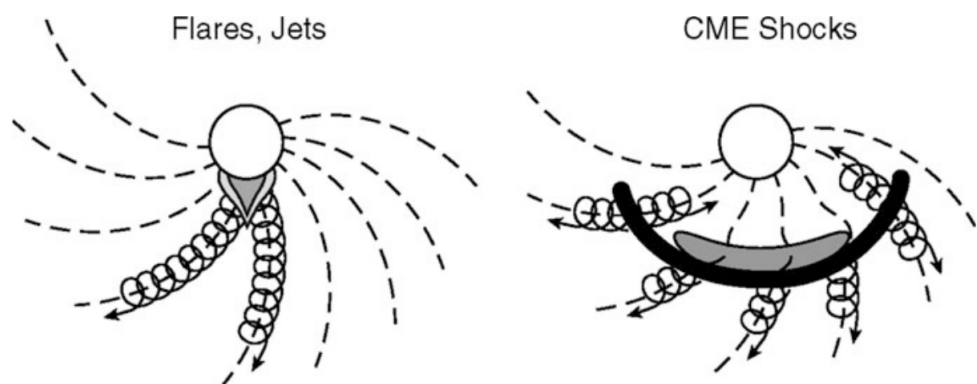


Figure 2.9: impulsive (left) and long-duration/gradual (right) SEP events [77]. Impulsive SEPs are drawn with the associated flare while long-duration events are drawn with the CME shock at their origin. Particle trajectories are shown as spirals along the magnetic field lines.

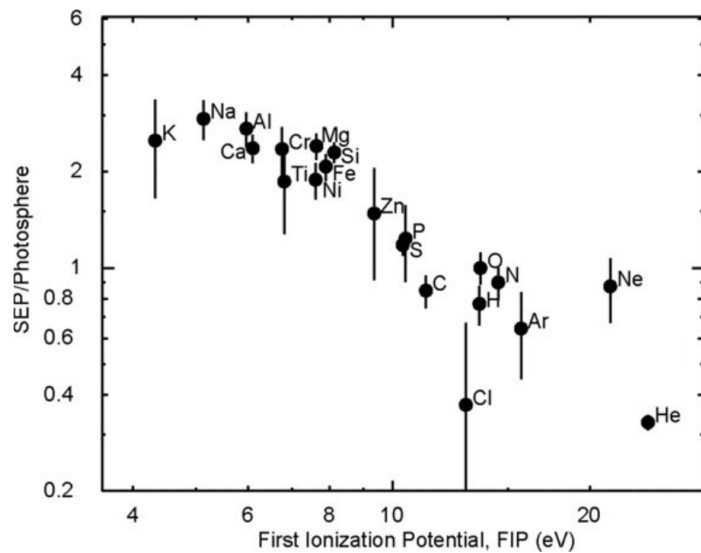


Figure 2.10: average element abundances in long-duration SEP events [82]. The abundances are expressed relatively to the corresponding ones observed in the solar photosphere, as a function of the FIP of the element.

Chapter 3

Alpha Magnetic Spectrometer

The Alpha Magnetic Spectrometer (AMS) is a particle physics detector on the International Space Station (ISS) conducting a unique, long-duration mission of fundamental physics research in space. The main goals of the experiment are the study of dark matter, antimatter and Cosmic Rays in general.

A precursor flight, AMS-01, was flown on the Space Shuttle Discovery in June 1998 and its results are reported in ref. [40]. After that experience, AMS-02 detector was built, launched on the Space Shuttle Endeavour and installed on the ISS on May 19, 2011. Currently, AMS-02 is taking data orbiting the Earth at an altitude of about 400 km, with an orbit inclination of 52° and an angle of about 12° with the ISS zenith, to avoid having the solar arrays in the field of view (see fig. 3.2). Before launch, AMS was tested extensively at the CERN test beam with e^\pm , p and π [91].



Figure 3.1: picture of AMS-02 installed on the ISS on May 19, 2011 [92, 93].

AMS consists of a permanent magnet and a series of particle detectors:

- a Silicon Tracker, to measure rigidity;
- a Time-of-Flight (ToF), to measure velocity and charge;
- Anti-Coincidence Counters (ACC), to veto particles entering from the sides;
- a Transition Radiation Detector (TRD), to separate e^\pm from p and nuclei and to measure charge;



Figure 3.2: picture of the ISS [92, 94]. AMS-02 can be seen on the left.

- a Ring Imaging Cherenkov (RICH) detector, to measure velocity and charge;
- an Electromagnetic Calorimeter (ECAL), to measure energy and to distinguish hadronic from electromagnetic particles.

Figure 1.10 shows the AMS elements.

Digitization of analog signals of AMS components can reduce significantly the live-time of the detector, causing the loss of interesting physics. To reduce the dead-time, a multi-level trigger system was implemented: *Fast Triggers (FTs)* are evaluated within about 40 ns using the ToF and the ECAL; then, level 1 triggers are generated in about 1 μ s only if strictly necessary using signals from ToF, ACC and ECAL. When a LV1 trigger is active, DAQ system starts acquiring the event, taking about 220 μ s; during this time no other events can be captured.

After AMS installation, two *Payload Operations and Control Centers (POCCs)* were opened to constantly control and monitor the system status: one at CERN (Geneva, specifically in the Prévessin site) and another one in Taiwan. The first is kept operative 24 hours a day and the other one covers detectors shifts during the European nighttime. The active POCC receives data downlinked by ISS from NASA and saves the records in the databases of *AMS Monitoring Interface (AMI)*. The AMI is then accessed by POCC team to look at real-time parameters and check AMS status.

3.1 Permanent magnet

Figure 3.3 shows the magnet used by AMS-02 and its precursor flight AMS-01 [40].

The magnet is composed of 64 sectors disposed in a cylindrical shape with an inner radius of 115 cm, an outer radius of 129.9 cm and a height of 80 cm. Each sector is formed by 100 blocks of Nd-Fe-B attached together using epoxy. The final magnet generates a dipole field almost uniform with an intensity of 0.15 T in its center and negligible outside the detector ($\sim 10^{-2}$ T).

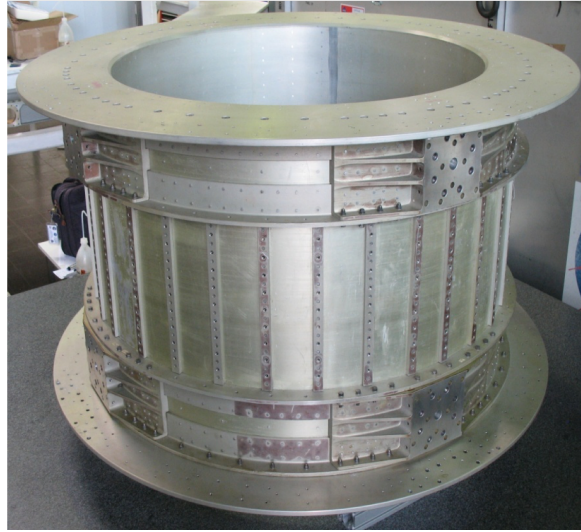


Figure 3.3: AMS permanent magnet [95].

The magnet also defines the reference frame (see fig. 3.4):

- the origin coincides with the magnet center;
- z -axis is parallel to the symmetry axis of the cylinder and points to the top of the detector;
- x -axis is parallel to the magnetic field;
- y -axis is given by $\hat{z} \times \hat{x}$

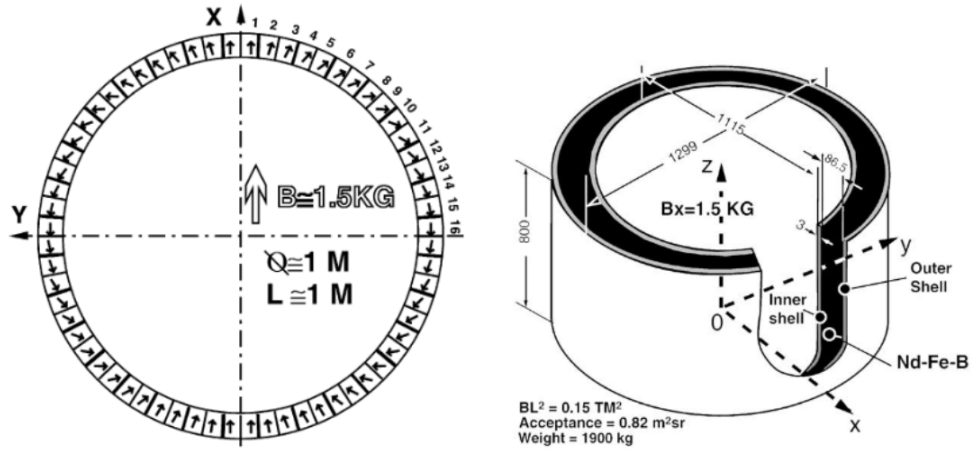


Figure 3.4: details of AMS magnet [40]. On the left, a slice of the magnet is drawn with the orientation of the magnetic field generated by each sub-sector. On the right, the whole magnet is drawn with the reference frame.

3.2 Silicon Tracker

The Silicon Tracker [97] is made of 2284 double-sided micro-strip silicon sensors distributed over 9 layers. The layers are disposed on three planes inside the magnet and three outside, as shown in

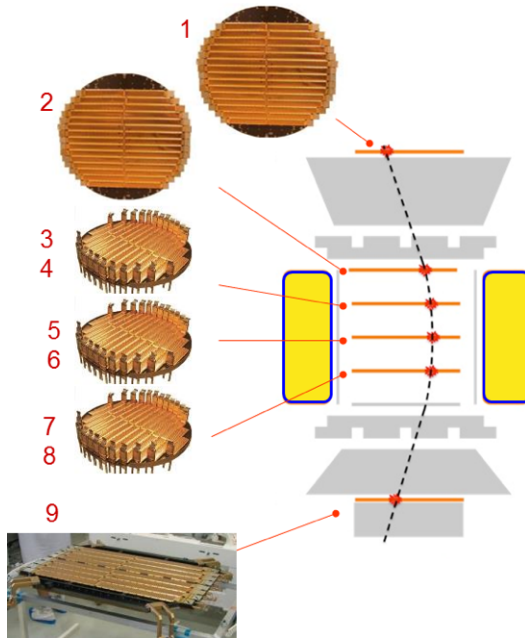


Figure 3.5: AMS Silicon Tracker with its planes disposition [96].

figure 3.5. The first layer is on top of the TRD, the second above the magnet, the next six inside of it and the last one between the RICH and the ECAL. The total active area of the Tracker is of 6.4 m^2 .

The silicon sensors are assembled in basic functional elements named *ladders*. The Tracker has a total of 192 ladders, grouped and monitored along the x direction by the readout electronics.

The core elements of the Tracker are its double-sided silicon sensors. Each sensor is $72.045 \times 41.360 \times 0.300 \text{ mm}^3$ and biased using a dynamic resistive coupling of n -type and punch-trough and surface-trough techniques. The sensors are crossed by p^+ strips on one side and orthogonal n^+ strips on the other. The implantation pitch is of $27.5 \mu\text{m}$ for p^+ strips and $110 \mu\text{m}$ for n^+ strips while the readout pitch is of $104 \mu\text{m}$ for p^+ strips and $208 \mu\text{m}$ for n^+ strips. The p -side is used to measure the bending, i.e. the y coordinate and this is why it has a finer pitch, while the n -side is used to measure the x coordinate.

A charged particle crossing a sensor release by ionization about $\sim 10^4$ electron/hole pairs. The pairs are collected using the electrical field generated in the bulk in about 10 ns and the resulting current signal is used to measure the total energy deposit, then the passing position is obtained combining that information with the strips disposition; the overall resolutions are of $10 \mu\text{m}$ along the bending direction (y) and of $30 \mu\text{m}$ along the transverse (x). The series of crossing points of a single event can finally be used to trace a path, to measure its curvature and consequently the rigidity. The Maximum Detectable Rigidity (MDR)* for the Silicon Tracker is of 2.2 TV [98]. The curvature of the trace is also used to determine the sign of the charge of the particle. For that measurement, also signals from ToF are used since a positively-charged particle entering from the top has a curvature similar to the one of a negatively-charged particle entering from the other side.

The Tracker is accompanied by two auxiliary sub-systems: the *Upgraded Tracker Thermal Pump System (UTTPS)* [99] and the *Tracker Alignment System (TAS)* [100]. The first is a heat exchanging system that uses CO_2 to cool the electronics. The second provides optical signals in the 8 layers that mimic straight traces to detect changes of the alignment with a position accuracy

*i.e. the rigidity value at which $\Delta R/R = 100\%$.

of better than $5 \mu\text{m}$.

Silicon Tracker performance was studied using several test beams of electrons, photons, protons and ions [91].

3.3 Time of Flight

The Time-of-Flight (ToF) [101] measures the velocity, the flight direction and the charge of passing particles. It is composed of 4 planes of scintillator counters, 2 placed above the magnet and 2 below, as shown in figure 3.6.

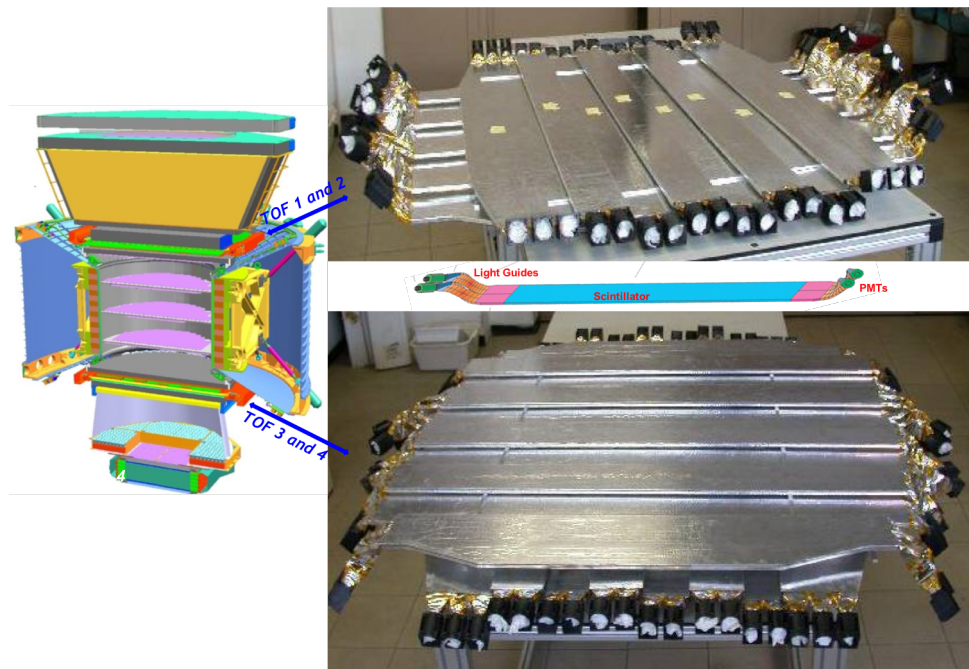


Figure 3.6: AMS ToF [102].

The planes 1,2,4 contain 8 scintillators paddles, the third one, below the magnet, contains 10 of them. The planes are alternatively aligned to the x - and y -axis. The internal paddles have a rectangular shape and are 1 cm thick, 12 cm wide and 110–135 cm long, while the external ones have a trapezoidal shape, the same thickness and are 18–26 cm wide and 110 cm long. To ensure complete coverage, neighbouring counters are overlapped by 0.5 cm. The paddles are then coupled to 4 (rectangular paddles) or 6 (trapezoidal paddles) PMTs using plexiglass light guides. The light guides can be straight, tilted or twisted in order to minimize the photo-induced multiplication due to the stray magnetic field (i.e. $\sim 2 \text{ kG}$) [103]. PMTs can be powered with a voltage between 1700 V and 2250 V and the gain is about 10^6 at 2000 V.

ToF measures the speed of a crossing particle counting the elapsed time between the passage in the upper and in the lower scintillators. The overall resolution is of about 160 ps for protons and 100 ps for particles with $Z \geq 2$. Then, the scintillation light is used to measure the energy lost by ionization and consequently the charge ($E \propto Z^2$).

3.4 Anti-Coincidence Counters

The Anti-Coincidence Counters (ACC) [104] is used to reject particles entering the detector from the side and is composed of 16 scintillating paddles arranged on a cylinder around the permanent magnet.

The passage of charged particles produces in the ACC a scintillation light that is collected in wavelength shifter fibers of 1 mm of diameter and routed to 8 PMTs (equal to those of the ToF) which generate the output signal.

ACC is used to veto particles entering the detector sideways. In that case vertically moving secondary products can be misidentified as a particle entered vertically (see fig. 3.7).

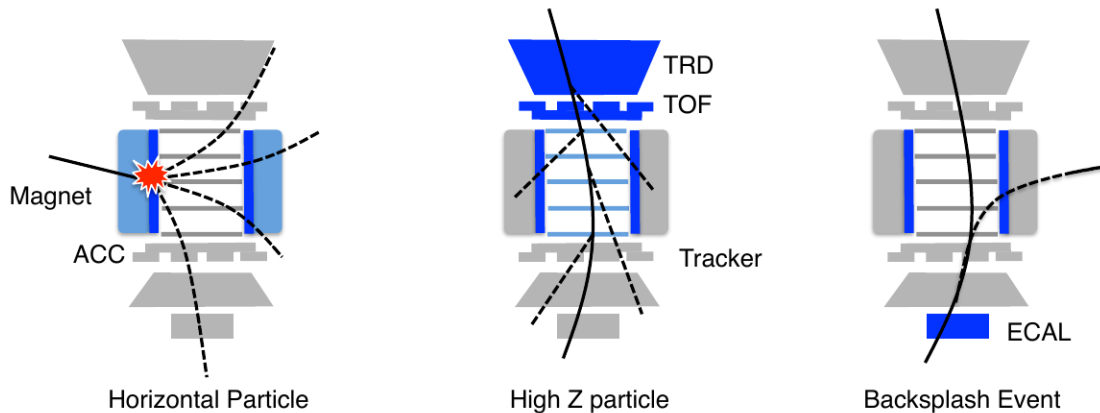


Figure 3.7: events seen by AMS ACC [105]. Activated systems are coloured in blue.

3.5 Transition Radiation Detector

The Transition Radiation Detector (TRD) [106] is used to distinguish e^\pm from protons and nuclei using the electromagnetic transition radiation emitted when a charged particle passes from a material to a different one [107]. The apparatus shown in figure 3.8 is placed between the first plane of the Silicon Tracker and the upper ToF.

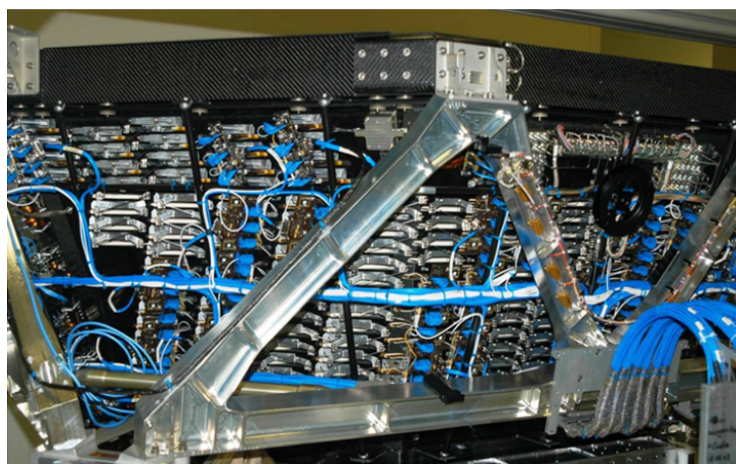


Figure 3.8: view of AMS TRD [108].

The TRD is made of 20 layers and a total of 328 modules. The first and the last four layers are oriented along the magnetic field while the others are disposed orthogonally to provide 3D tracking. The layers are supported by a conical structure visible in figure 3.9 made of an octagonal base, aluminum-honeycomb walls and carbon-fiber skins and bulkheads.



Figure 3.9: support structure of AMS TRD [106].

TRD modules are composed of a radiator and a proportional chamber, as shown in figure 3.10. The radiators are made of polypropylene/polyethylene fiber fleeces and are 22 mm thick, with a density of 0.06 g/cm^3 . The proportional chambers are made of straw tubes, 6 mm wide, operated in full avalanche mode at 1500 V. The walls of the tubes are used as cathodes and are made of a $72 \mu\text{m}$ thick double-layered kapton-aluminum foils; the central wires are used as anodes and are gold plated and $30 \mu\text{m}$ thick. Relativistic particles passing in the radiators can emit X-rays detectable by the chambers, where the Xe gas is used as absorber and the CO_2 as quencher for charge multiplication.

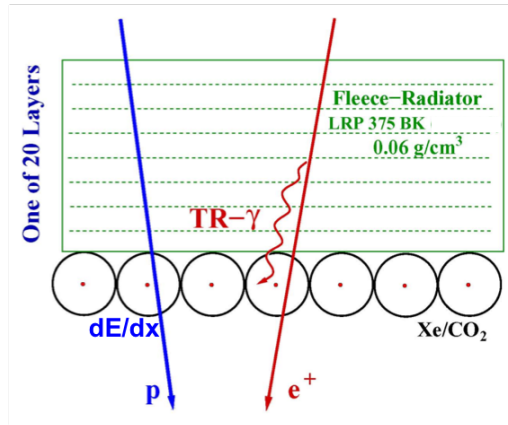


Figure 3.10: one module of AMS TRD [108].

The energy deposit in each tube can be used to determine the charge of passing particle, thanks to the relation

$$\frac{dE}{dx} \propto Z^{-2}$$

The output signal of the tubes is digitized by a 12-bit ADC that saturates at $Z = 6$ (carbon). The work presented in [109] shows how to extend this limit up to $Z = 26$ (iron) using for δ -rays.

TRD performances were studied using Monte Carlo simulations and beam tests, obtaining a maximum rigidity of 1 TV for e^\pm identification. Figure 3.11 shows the proton rejection power obtained from experimental data.

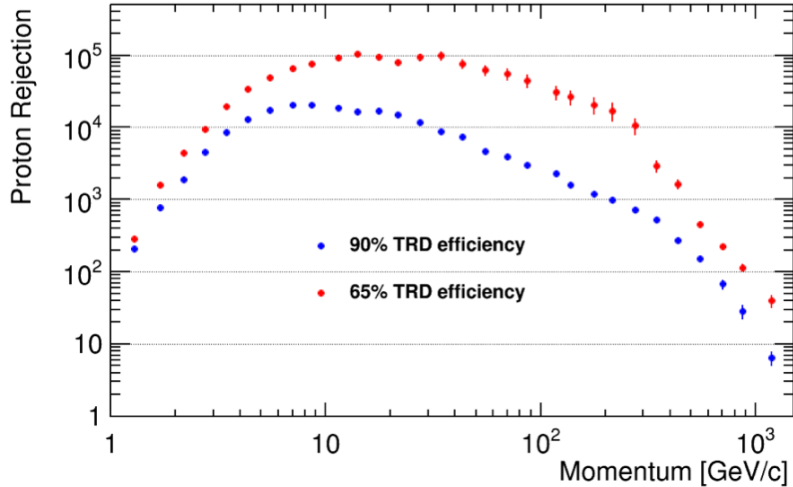


Figure 3.11: proton rejection power of AMS TRD measured on experimental data at 90% and 65% efficiencies [108].

TRD proportional chambers leak gasses into space continuously with a pressure variation of $-4.5 \text{ mbar per day}$. For that reason the detector is coupled to a gas supplier system that refill the apparatus, maintaining the correct gas mixture [110].

3.6 Ring Imaging Cherenkov

The Ring Imaging Cherenkov (RICH) detector [111] is used to measure particles β and Z and is placed under the lower ToF. Figure 3.12 shows the apparatus.

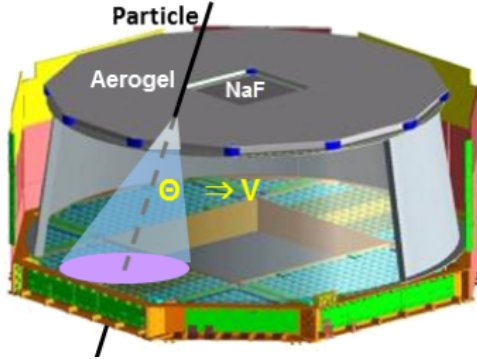


Figure 3.12: AMS RICH [112].

A charged particle moving in a material with a velocity $v > n(\omega)/c = c'$, with $n(\omega)$ refraction index and c' speed of light in the material, emits a cone of electromagnetic radiation. The so called Cherenkov cone can be then used to infer particle's β and Z measuring the opening angle θ_C and the number of photons N_C emitted per frequency and length units and using the equations:

$$\beta = \frac{1}{\cos \theta_C n(\omega)}$$

$$Z = \frac{1}{\sin \theta_C} \sqrt{\frac{1}{\alpha} \frac{\partial^2 N_C}{\partial \omega \partial x}}$$

The global performances of AMS RICH are a resolution on β of $\sim 0.1\%$ for particles with $Z = 1$ and of $\sim 0.01\%$ for ions and a resolution on Z of about 0.3 charge units for He, up to about 0.5 for Si ions.

To produce the Cherenkov cone, RICH uses a dual radiator made of silica aerogel ($n = 1.05$) outside and of sodium fluoride ($n = 1.335$) inside (see fig. 3.12). The external tiles that compose it are 2.7 cm thick while the internal ones are $35 \times 35 \text{ cm}^2$ big and 5 mm thick. The final acceptance of the radiator is of $0.4 \text{ m}^2 \text{ sr}$.

To increase the overall acceptance, a multi-layer conical reflector is placed all around the detector, so that photons emitted with a high inclination can not escape the experimental area. The mirror has a height of 47 cm.

Finally, a detection plane is placed below the radiator to detect Cherenkov light. The detection plane has a hole of $64 \times 64 \text{ cm}^2$ in the center in correspondence of the active area of the ECAL, while the remaining part of a circle of 134 cm of diameter is covered using 680 PMTs.

3.7 Electromagnetic Calorimeter

The main core of AMS Electromagnetic Calorimeter (ECAL) [113, 114] is its *pancake* (see fig. 3.13), a composite block of scintillating fibers and lead foils. It can measure the original particle energy and trace the shower it produces in the active material.

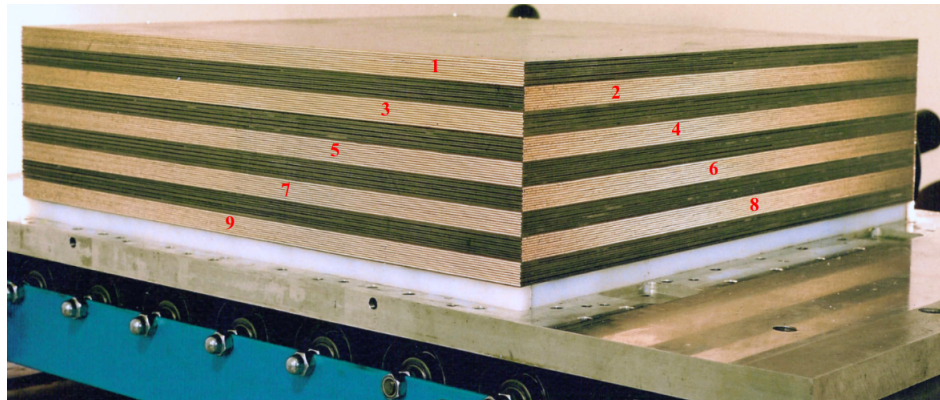


Figure 3.13: pancake of AMS ECAL [114].

The pancake has a volume of $648 \text{ (length)} \times 648 \text{ (width)} \times 166 \text{ (thickness)} \text{ mm}^3$ and is subdivided in 9 *SuperLayers* (SLs). Each SL is 18.5 mm thick and is composed of 11 lead foils of 1 mm of thickness, separated by scintillating fibers of 1 mm of diameter. The fibers are glued to the foils using optic epoxy and in each SL they run all along the same direction. To trace the shower's particles, SLs are alternatively stacked parallel to the x - (5 SLs) and y -axis (4 SLs). The final lead-fiber-glue composition of the pancake is of 1 : 0.57 : 0.15. Regarding the read-out, each SL is monitored by 36 four-anode PMTs, so that each anode covers an area of $9 \times 9 \text{ mm}^2$, i.e. 35 scintillating fibers; the area covered by one anode makes a *cell* (see fig. 3.14). Finally, the pancake has an overall average density of about 6.8 g/cm^3 , with an electromagnetic interaction length $X_0 \simeq 1 \text{ cm}$ and a Molière radius $R_M \simeq 2 \text{ cm}$. Therefore, one cell corresponds to about $1X_0$ and $0.5R_M$ and the Calorimeter in its entirety covers a length of about $17X_0$ and $0.7\lambda_{\text{int}}$, with λ_{int} nuclear interaction length.

In order to have a good linearity in a large energy range (i.e. from few MeV up to about 60 GeV), each PMT anode signal is split into two different channels: the *High Gain* (HG) and the *Low Gain*

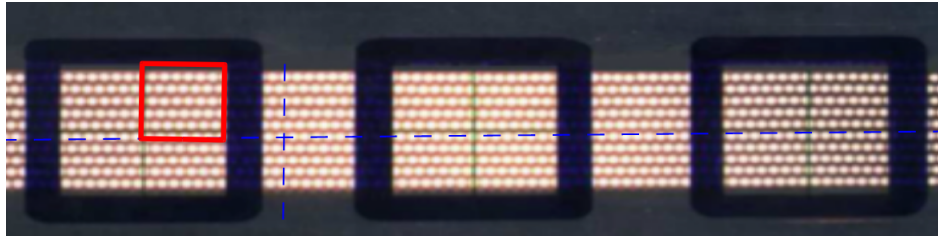


Figure 3.14: view of one SL of AMS ECAL [114]. The big square shows the footprint of one PMT and the red square highlights the area covered by one anode, i.e. a cell.

(LG) channels. The HG channel is amplified and sensitive to Minimum Ionizing Particle (MIP), which release about 7 MeV per cell. The LG channel is not amplified and used for high energy measurements, up to 1 TeV (60 GeV per cell). The gain ratio between the two channels is of about 33.

The longitudinal profile of an electromagnetic shower can be described using a Γ distribution as

$$\left\langle \frac{1}{E} \frac{dE}{dt} \right\rangle = \frac{(\beta t)^{\alpha-1} e^{-\beta t}}{\Gamma(\alpha)} \quad (3.1)$$

with $t = x/X_0$, the scaling parameter $\beta \approx 0.5$ and α the shape parameter [115]. Using 3.1 it can be demonstrated that the ECAL is able to contain the 75% of energy deposited by the shower initiated by a particle of 1 TeV.

The energy resolution as obtained by beam tests can be described by the formula

$$\frac{\sigma(E)}{E} = \frac{(10.4 \pm 0.2)\%}{\sqrt{E}} \oplus (1.4 \pm 0.1)\% \quad (3.2)$$

Data has been collected using e^\pm beams between 6 and 250 GeV and p beams of 400 GeV; the results are shown in figure 3.15.

The angular resolution of the ECAL tracking was measured to be better than 1° for energies above 50 GeV [117].

The measured trigger efficiency for photons is better than 99% above 5 GeV. That is valid only for photons that do not produce a pair e^\pm before reaching the Calorimeter. Considering the radiation lengths before, only 40% of the photons that cross AMS completely produce an early pair. Then, those pairs are detected first by the Silicon Tracker.

Beyond measuring the energy of the particles, one of the main goals of the ECAL is to separate electrons from protons. That is done considering the shape of the shower in the Calorimeter and the ratio between the total energy deposited in the Calorimeter and the rigidity measured by the Tracker. Figure 3.16 shows the proton rejection obtained using AMS ECAL.

The ECAL is equipped with its own trigger board, the ETRG [118], that generates signals sent to AMS trigger board, the JLV1. The complete functioning of the trigger system, ETRG board included, is described later in section 3.8.

3.8 Trigger system

AMS trigger system makes use of the signals coming from ToF, ACC and ECAL to select which events need to be acquired by the Data Acquisition (DAQ) system. The system is implemented by the JLV1 board [119].

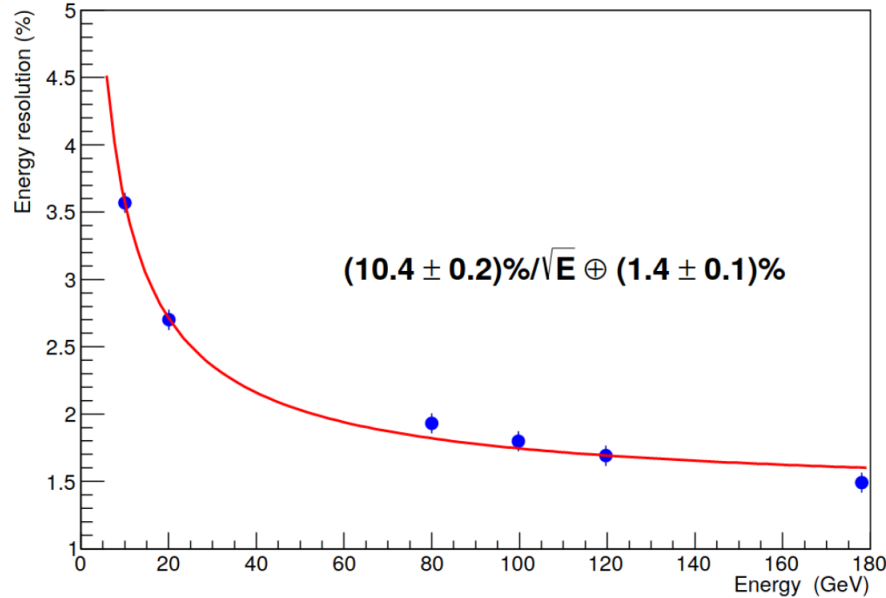


Figure 3.15: energy resolution of AMS ECAL [116]. Blue points show experimental data collected using e^\pm beams between 6 and 250 GeV and p beams of 400 GeV. Red line plots equation 3.2.

There are two types of triggers: *Fast Triggers (FTs)* and *Level 1 (LV1) triggers*. FTs take around 40 ns to be evaluated while LV1 triggers can need up to 1 μ s. Data acquisition is started only if at least one FT and one LV1 trigger are active and take about 220 μ s to save all signals from the detectors. To minimize AMS dead-time, LV1 triggers are evaluated only when a FT has been activated and event acquisition is triggered only with a positive LV1 signal.

3.8.1 Fast Trigger

Fast Triggers (FTs) [119] take about 40 ns to be generated and are built using only data from ToF and ECAL.

ToF generates 6 signals per plane and each plane gives 3 types of information:

- *Charged Particle (CP)*, logical OR between ToF paddles signals above *High Threshold (HT)**;
- *Charged particle in Tracker acceptance (CT)*, CP signals with the additional condition of being inside the Silicon Tracker acceptance;
- *Big-Z (BZ)*, logical OR between ToF paddles signals above *Super-High Threshold (SHT)*†.

ECAL has its own trigger board, the ETRG [118]. ECAL Trigger (ETRG) takes into consideration ECAL SLs 2 to 7, ignoring the first and the last two SLs. Usually photons do not convert or convert too late in the first SL and particles of few GeV do not deposit a significant amount of energy in the last two layers. ECAL Trigger (ETRG) generates two ECAL Fast (ECAL-F) signals, one for the x view (3 SLs) and one for the y view (3 SLs). The signal is set to true when the energy deposit read by a PMT is above 40 MeV in at least 2 SLs out of 3. JLV1 board receives ECAL-F signals and combine them applying the logical AND (ECAL-F_and signal) and OR (ECAL-F_or signal).

*HT is set at about 60% of the signal of a MIP to detect $Z \geq 1$ particles.

†SHT is set at about 400% of the signal of a MIP to detect $Z \geq 2$ particles, as for example *strangelets*‡.

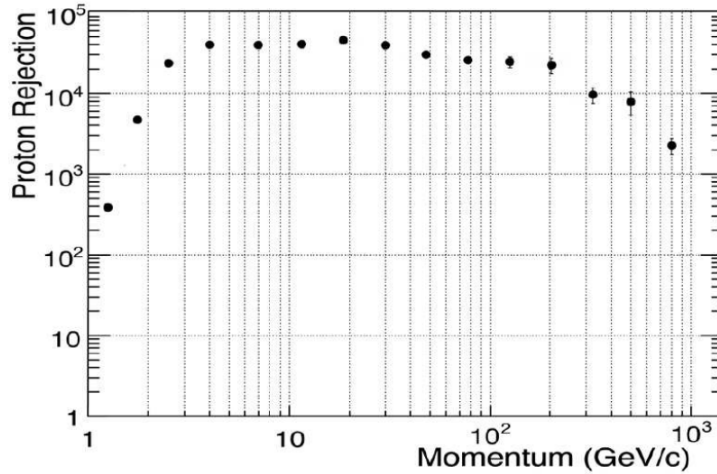


Figure 3.16: proton rejection obtained with AMS ECAL (figure taken from [116]). Electromagnetic particles are identified imposing $E/p > 75\%$ and using a Boosted Decision Tree model on experimental data.

Signals from ToF and ECAL (i.e. CP, CT, BZ, ECAL-F_and, ECAL-F_or) are used to generate the final the FTs:

- *FTC signal*, logical OR of CP, CT signals from ToF;
- *FTZ signal*, generated using BZ signals from ToF and an extended time window to look for highly-charged particles slower than ions but with their same charge and rigidity;
- *FTE signal*, generated using ECAL-F signals;
- *FT signal*, logical OR of FTC, FTZ, FTE signals.

3.8.2 Level 1 trigger

Level 1 triggers are evaluated by JLV1 board only when a FT is true. LV1 signals generation takes about 1 μ s and the data acquisition decision is made on them. LV1 logic produces six types of signals: [119]:

- *CP signals* – CP, CT signals from ToF are used to produce FTCP0, FTCP1, FTCT0, FTCT1 signals;
- *BZ signals* – BZ signals from ToF are used to produce similar signals for LV1 triggers;
- *ACC signals* – signals from ACC and two settable thresholds on the number of hits are used to produce ACC0, ACC1 signals;
- *ECAL-F signals* – ECAL-F signals from ECAL are used to produce similar signals for LV1 triggers;
- *ECAL-A signals* – ECAL-A signals* from ECAL are used to produce similar signals for LV1 triggers.

*ECAL Angular signals are generated in the ETRG similarly to the ECAL-F signals, but require in addition a shower-like deposit.

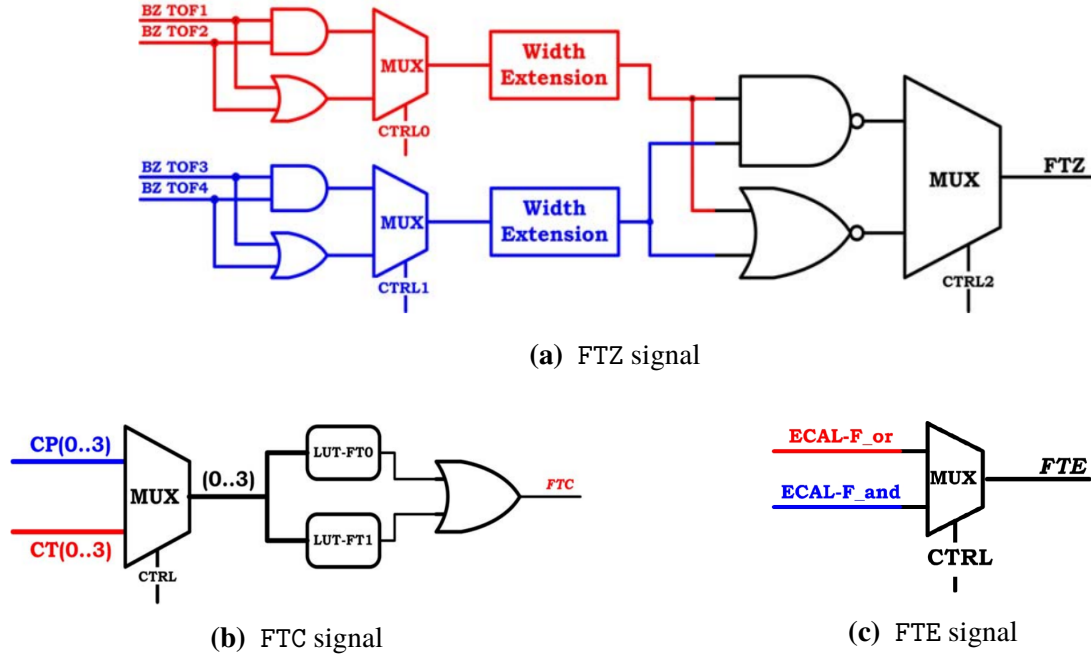


Figure 3.17: logic schemes of AMS Fast Triggers [119].

All input signals are latched using a gate of 240 ns, except for BZ signals for which a gate of 640 ns is used, due to their usage for slow ions detection.

JLV1 provides 8 slots to define as many LV1 sub-triggers (subLV1 signals) [120]. Currently only 7 slots are used and indexed from 0 to 6:

0. *unbiased charged trigger*, activated when 3 ToF planes (out of 4) have a signal above HT (pre-scaling factor* of 100 applied);
1. *single charged trigger*, activated when all ToF planes have a signal above HT and no hits are detected in ACC;
2. *normal ions trigger*, activated when all ToF planes have a signal above SHT and less than 5 hits are detected in ACC;
3. *slow ions trigger*, activated when all ToF planes have a signal above SHT, with an extended gate applied to account for slow strangelets as well;
4. *electrons trigger*, activated when all ToF planes have a signal above SHT and both ECAL views (x,y) are triggered;
5. *photons trigger*, activated when both ECAL views (x,y) are triggered and the axis of the shower detected in the calorimeter is contained in AMS field of view;
6. *unbiased EM trigger*, activated when both ECAL views (x,y) are triggered (pre-scaling factor* of 1000 applied).

A inclusive LV1 signal is generated by the logical OR between all subLV1 signals.

*pre-scaling factors are applied to triggers with a high rate to reduce it.

3.9 Data Acquisition System

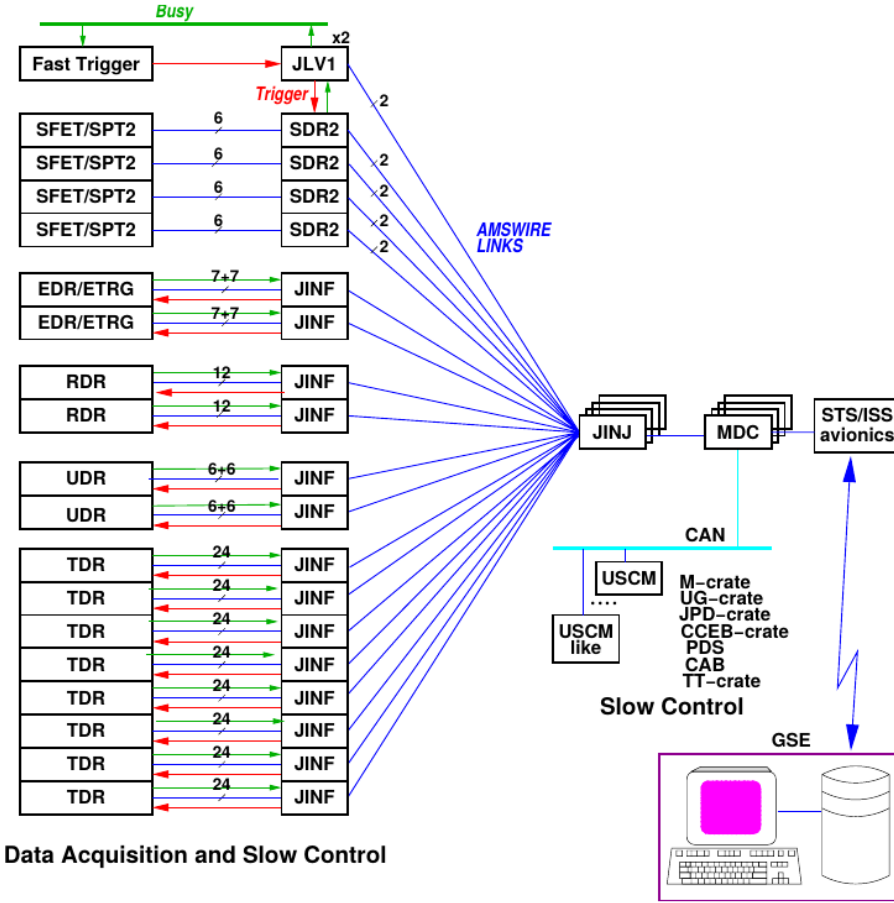


Figure 3.18: block diagram of AMS DAQ [121].

AMS DAQ system [121] reads data from over 200 thousand analog channels and has a tree-like structure made of 264 Data Reduction (DR) nodes; a letter prepended to the DR name identify the corresponding sub-detector*. DR nodes collect data from analog electronics front-ends, 28 JINF nodes that collect data from DRs, 8 SDR2 nodes that collect data from ToF and ACC to produce trigger signals, 2 JLV1 nodes that produce LV1 trigger signals and 4 JINJ nodes that collect data from JINF, SDR2 and JLV1 nodes (see fig. 3.18). The baseline operation mode of DAQ system assumes there is no redundancy in DR nodes, double redundancy in JINF nodes and quadruple redundancy in JINJ nodes. Actually UDR, EDR and SDR2/SPT2/SFET nodes are double redundant. Redundancy was implemented to make the system more reliable, since in case of damages backup nodes are available.

LV1 trigger signals are distributed to all DR nodes and when one of them is active, digitization of analog signals from front-end electronics is started and the resulting information is buffered. At high trigger rates the digitization time defines the dead time of the system. It can go up to 220 μ s (TDR nodes) and at 2 kHz the dead time is of 16%. On a LV1 trigger, events from sub-detectors are collected and buffered by DR nodes, then JINF nodes retrieve and pack them with data coming from other DR units and the same is done by JINJ nodes. Finally, JMDC collects all data, performs

*U is used for TRD, S for ToF and ACC, T for Tracker, R for RICH and E for ECAL

final preprocessing and sends it to NASA avionics for downlink.

Buffering is used at every level of DAQ hierarchy to minimize extra dead time due to data processing that adds itself to the one due to digitization. A Monte Carlo study was performed using a benchmark Fast Trigger with a rate of 2 kHz to study the system and find the best parameters for its setup. Figure 3.19 shows the results of the study.

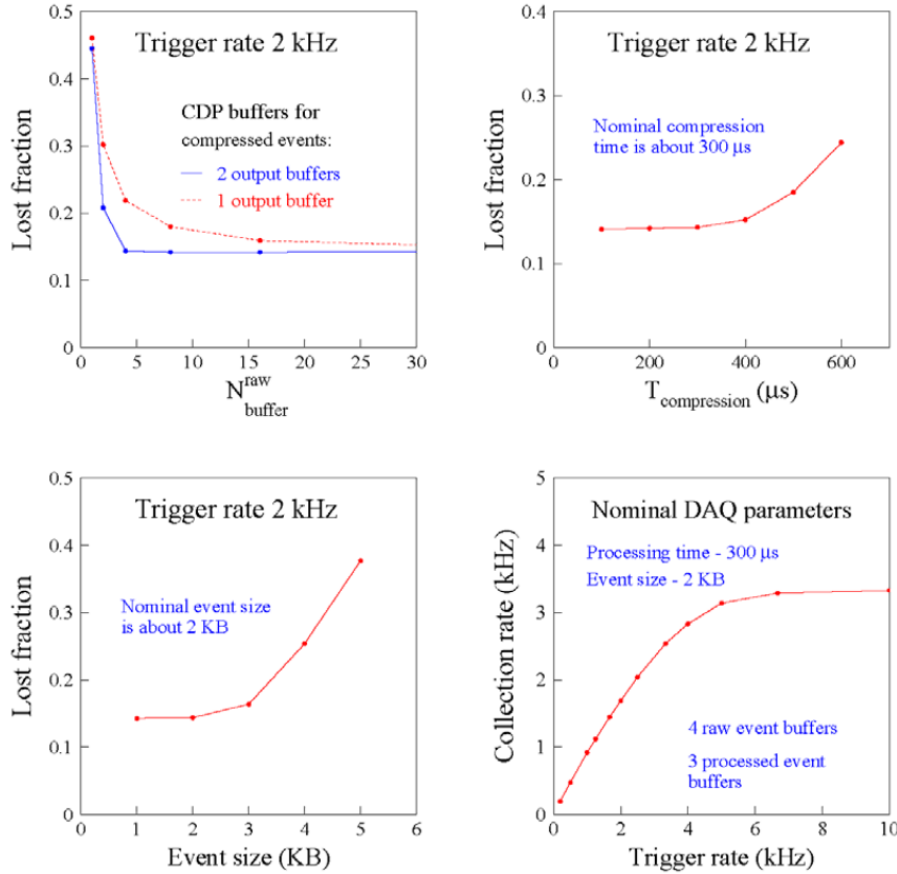


Figure 3.19: performances of AMS DAQ system [121].

Data delivered to ISS avionics are split into two main streams before being sent to ground: real-time and buffered. The real-time stream has a lower bandwidth and contains mostly information about the status of the detectors. The buffered stream has a larger bandwidth and contains science data that shall not be lost in case of lack of connection to the ground. However, the cons of this stream is the presence of a time delay in data delivering and this is why it is not suitable for the transmission of information about the live status of the systems.

3.10 Monitoring Interface

AMS Monitoring Interface (AMI) [122] is a system built specifically to store and give access to AMS data. It uses InfluxDB databases [123] as backend and Grafana instances [124] as frontend. Figure 3.20 shows a scheme of its structure.

Raw data coming from ISS are parsed by a feeder which then fills two independent InfluxDB databases, one hosted by CERN [125] and one by AMS POCC's servers to provide dual redundancy. Similarly two independent Grafana instances hosted by CERN [126] and AMS POCC's servers are

Node	Buffer length	Processing time (typical)	Transmission time to the next node (typical)
frontend electronics	–	90 µs	–
DR	4 events	280 µs	220 µs
JINF	4 events	–	220 µs
JINJ	4 events	–	260 µs
JMDC	2 events	250 µs	250 µs
NASA avionics	–	–	–

Table 3.1: setup and timing of AMS DAQ nodes.

connected to each database and synced to provide the same plots and dashboards. The CERN instance acts as a web client for AMS members and it is accessible within CERN’s network [127].

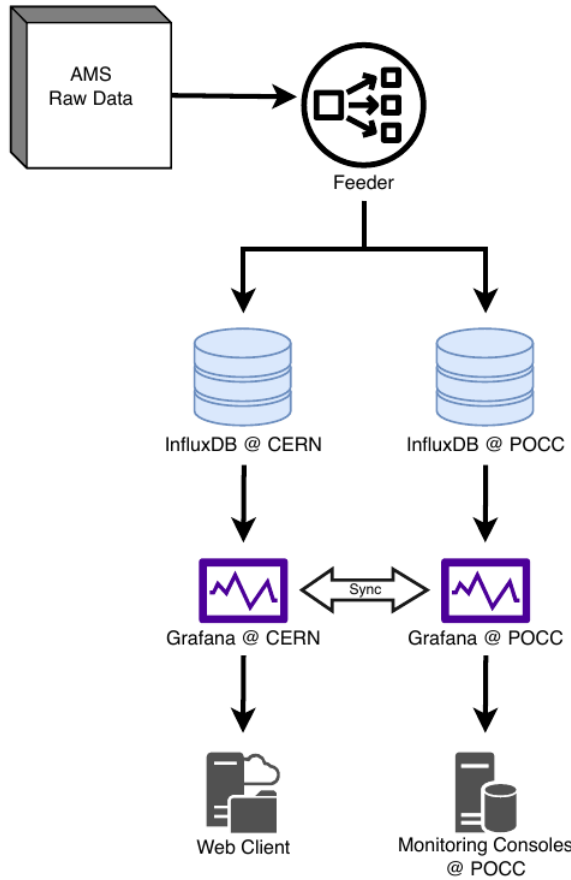


Figure 3.20: scheme of AMS Monitoring Interface structure [122].

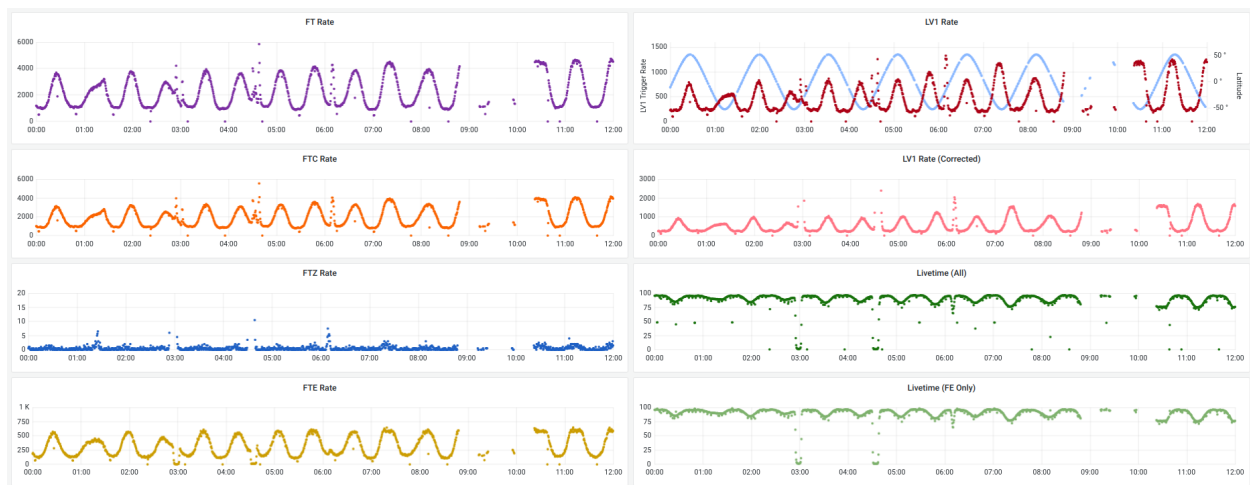


Figure 3.21: AMI dashboard on JLV1 status. Plotted data are taken in 00:00–12:00 UTC of April 23, 2023.

Chapter 4

Detection of Solar Energetic Particles

Intense SEPs near the ISS can be detected looking for excesses in the trigger rates of AMS [8]. To perform a real-time monitoring of these events, an appropriate identification algorithm is needed. The repository *ami-sep* [128] realized for the development of this thesis, provides such a type of algorithm in a Python package.

The *ami-sep* package can be executed on an arbitrary time range of data. If not explicitly specified, data processing starts from the current time and keeps running until user's signal. The processing performs a loop on data chunks following these steps:

1. data queries to the AMI database;
2. preprocessing of the retrieved records;
3. analysis of trigger rates for the detection of excesses;
4. buffering of data for the generation of reference distributions used in the analysis of the following chunks.

The package accepts various command line options to change the parameters of data queries, preprocessing, analysis and real-time monitoring; those parameters are documented in the Python package help messages and the most relevant are described in the following sections.

4.1 Data source

The database used for the AMI is an InfluxDB [123] instance. InfluxDB is an open source database optimized to store and access time-series data. A single instance can actually store in itself multiple *databases*, each of which is separate from the others. Each database can in turn contain multiple *measurements* that can be seen as a table, indexed by time along rows and by *fields* and *tags* along columns. Differently from the fields, tags are indexed, therefore querying data by them is more efficient.

AMI database contains all the scientific and life status data of AMS detectors. The main database stored in the AMI is named *AMS_ISS* and contains most of the data stored. The analysis package realized takes into account only some of its measurements for SEPs identification:

- *GPS_Info_v1*, containing ISS coordinates,
- *ISSLive* and *ISS_LVLH*, containing ISS flight orientation,
- *JLV1*, containing AMS trigger rates and live-time.

Position

GPS_Info_v1 contains cartesian coordinates in meters units in the fields X, Y, Z. Position data is used to determine the properties of the detection area (e.g. geomagnetic field, McIlwain's L -values).

Flight orientation

ISSLive and ISS_LVLH contain ISS flight angles yaw, pitch and roll in degrees respectively in the fields curr_yaw, curr_pitch, curr_roll and yaw, pitch, roll. The two measurements have different properties: records in the former are given once per second and the oldest date back to May, 2011; records in the latter are given once per minute and the oldest date back to June, 2016. Real-time data only use ISSLive, therefore it is favored to retrieve ISS flight orientation, while ISS_LVLH is accessed only if necessary. Then, flight angles are used to compute the zenith of AMS.

Live-time and trigger rates

JLV1 contains AMS live-time η_{live} as a 0–100 value and AMS trigger rates λ in Hz units. The corresponding fields in the database are livetime_0, FT, FTZ, FTC, FTE, LV1, subLV1_0, subLV1_1, subLV1_2, subLV1_3, subLV1_4, subLV1_5, subLV1_6. Trigger rates are needed to detect SEP events, while live-times are used to rescale the raw rate λ to its corrected value

$$\lambda_{\text{corr}} = 100 \cdot \frac{\lambda}{\eta_{\text{live}}} \quad (4.1)$$

4.2 Data preprocessing

As described in the previous section, data queries produce three dataset about ISS position, ISS orientation and AMS trigger rates and live-times. The analysis of trigger rates for SEPs identification requires for each record all the information, therefore a complete dataset is produced by the union of the original three. Position, orientation and trigger fields are stored in AMI with different periodicities, so the complete dataset can contain records missing some fields. The probability density functions (PDFs) and cumulative distribution functions (CDFs) of time differences between consecutive AMI entries for one month of data are reported in figures 4.1 and 4.2.

The following steps are applied on the complete dataset for its preprocessing:

1. conversion of position coordinates from meters to Earth radii ($R_{\text{Earth}} = 6371.2$ km);
2. rescaling of live-times from the range 0–100 to 0–1;
3. insertion of elapsed time from the last valid position;
4. insertion of elapsed time from the last valid orientation;
5. filling of missing positions and orientations with the last valid observation;
6. removal of records with no position or orientation, possibly left by the previous steps;
7. insertion of geomagnetic field intensities and McIlwain's L -parameter [29];
8. insertion of AMS zenith angles;
9. insertion of corrected rates and rate ratios values.

Geomagnetic field intensities and L -values

Geomagnetic intensities and L -values for a specific time and position are calculated using the Python module *irbempy* of the *SpacePy* package, which provides an interface to the International Radiation Belt Environment Modeling (IRBEM) library [129–131]. The geomagnetic field used for all calculations is the *International Geomagnetic Reference Field (IGRF)* [132, 133], which is initialized in the middle of the year, once per year and used with no additional external fields. The L -value is computed considering charged particles with a pitch angle of 90°. Figure 4.3 shows geomagnetic field intensities and L -values calculated for one month of AMS data.

AMS zenith angles

AMS zenith can be computed from the yaw, pitch and roll angles of flight of the ISS. The ISS adopts a Local Vertical Local Horizontal (LVLH) coordinate system and the flight angles are given respect to that system (see fig. 4.4). AMS is mounted on a lateral arm of the ISS with an inclination of 12° towards its center (see fig. 4.5), consequently its zenith angle θ in respect to the sky is given by

$$\theta = \arccos \left((0 \ 0 \ -1) R_z(\alpha) R_y(\beta) R_x(\gamma) R_x(-12^\circ) \begin{pmatrix} 0 \\ 0 \\ -1 \end{pmatrix} \right) \quad (4.2)$$

with $R_a(\phi)$ matrix of a rotation of ϕ along the axis a and α, β, γ respectively yaw, pitch and roll angles of the ISS.

Corrected rates and rate ratios

Raw rates from the AMI database are not rescaled by default using the live-time. In general the use of rates rescaled using eq. 4.1 should be favored over the raw ones, but some triggers present a low rate with discrete values, in which the original value can not be obtained simply dividing by the live-time. Therefore, the selection of the raw rates to rescale is left to the user through the package options.

Another option accepted by the package is the selection of a pairs of rates (λ_1, λ_2) for which calculate the ratio λ_1/λ_2 . Ratios of sub-triggers can highlight the overtaking of one kind of events over another not visible in their parent trigger (i.e. the signal resulting by their logical AND).

Additional information added to the dataset during preprocessing is used as follows:

- elapsed times from last valid position or orientation, geomagnetic field intensities and zenith angles are used to apply filters on the buffering of data for quiet-level distributions generation;
- L -values are used to characterize different areas of data taking;
- corrected rates and rates ratios can be used as features for SEPs detection.

4.3 Data analysis

The goal of the data analysis is the detection of sudden excesses in the trigger rates. Actually not all the available rates are processed and the user can select which of them to take into consideration.

Anomalous excesses are recognized by the comparison with *reference distributions* defining the *quiet level*. A maximum age T_{\max} is taken as parameter for the length of a buffer where recent past entries are collected. Then, this buffer is read to evaluate the quiet level value for each trigger and assess the deviation of the observed rates. The actual length T of the buffer can be less than T_{\max} . In fact, even if most of the time $T \approx T_{\max}$, AMI database can lack of some data leading to a decrease of T .

For each trigger not just one distribution is evaluated for the quiet level definition. ISS crosses regions with different L -values that are characterized by different quiet levels, as can be seen by looking at the live-time of the detector in figure 4.6. In subsection 1.4.2, equation 1.10 shows the unique relation among L and the rigidity cutoff R_C , i.e. the lowest rigidity a charged particle must have to reach a certain position in the geomagnetic field. Consequentially, data for the evaluation of quiet levels is split considering the L -values of the entries, which are grouped in bins whose width is a free parameter set through the options of the package.

Data analysis runs across preprocessed entries sequentially. For the first record, reference distributions are initialized querying a chunk of past data and buffering it skipping the analysis. Then, each analyzed record is appended to the buffer and the oldest entries with an age bigger than T_{\max} are discarded, following a FIFO logic. During the analysis of one record, the reference distributions are selected on the basis of the bin the L -value belongs to and the following properties are appended to the original entry:

- mean μ of the reference distribution;
- rms σ of the reference distribution;
- length T of the time range covered by the reference distribution,
- number of entries N in the reference distribution;
- score s of the observed rate.

The score s quantifies the deviation of a measurement from the quiet level and is defined using the p -value definition:

$$s(\bar{\lambda}) = \int_{\bar{\lambda}}^{+\infty} f(\lambda; \mu, [\sigma]) d\lambda \quad (4.3)$$

where $\bar{\lambda}$ is a measured trigger rate and f its PDF. Trigger rates probability density functions are another parameter of data processing and different ones can be selected by the user for each rate. Currently the package only supports normal and Poisson distributions and σ is only used in the former (this is the reason for the $[\sigma]$ notation). Ultimately, the definition of the score causes that excesses tend to null scores and decreases to unitary scores.

Because of the L -values binning, the time-series of μ , σ and N follow a stepwise trend (see fig. 4.7). This characteristic can lead to the observation of apparent excesses or lacks while approaching the boundaries of a bin. Consequently, another score \tilde{s} is added to the final dataset, combining the information of two bins. In particular, considering a measurement $(\bar{\lambda}, L)$, the two bin centers $[L]_i$, $[L]_{i+1}$ closest to L , such that $[L]_i \leq L < [L]_{i+1}$ and the distance $l_i = |L - [L]_i|$, the following values are computed:

$$\tilde{\mu} = \frac{l_{i+1}}{l_i + l_{i+1}} \mu_i + \frac{l_i}{l_i + l_{i+1}} \mu_{i+1} \quad (4.4a)$$

$$\tilde{\sigma} = \frac{l_{i+1}}{l_i + l_{i+1}} \sigma_i + \frac{l_i}{l_i + l_{i+1}} \sigma_{i+1} \quad (4.4b)$$

$$\tilde{N} = \frac{l_{i+1}}{l_i + l_{i+1}} N_i + \frac{l_i}{l_i + l_{i+1}} N_{i+1} \quad (4.4c)$$

$$\tilde{s}(\bar{\lambda}) = \int_{\bar{\lambda}}^{+\infty} f(\lambda; \tilde{\mu}, [\tilde{\sigma}]) d\lambda \quad (4.4d)$$

When the calculus of tilde values miss information for one of the two bins (e.g. $L \geq [L]_{N_{\text{bins}}}$), $\tilde{x} = x$ is imposed. Figure 4.7 shows the comparison between regular and tilde values of reference distributions properties.

4.4 Data buffering filters

Part of data can be excluded from buffering to avoid biasing the subsequent distributions. In particular the package allows setting the following values:

- minimum value for the geomagnetic field intensity;
- maximum value for the zenith angle;
- maximum value for the age of last valid position;
- maximum value for the age of last valid orientation;
- minimum value for the scores.

The cuts on geomagnetic field intensity and zenith angle can be used to exclude false events due to particles not coming from space, but trapped along the geomagnetic field lines. In particular, the geomagnetic field cut is useful to exclude the *South Atlantic Anomaly (SAA)* area, a region where the field is less than 32000 nT at sea level and the Van Allen belts decrease their altitude.

The cuts on the age of last valid positions and orientations are useful to exclude records where the information is too old to be reliable.

Cut on scores is applied whenever any of the trigger rates shows an excess. This cut is needed to avoid biasing the quiet level definition with SEPs events.

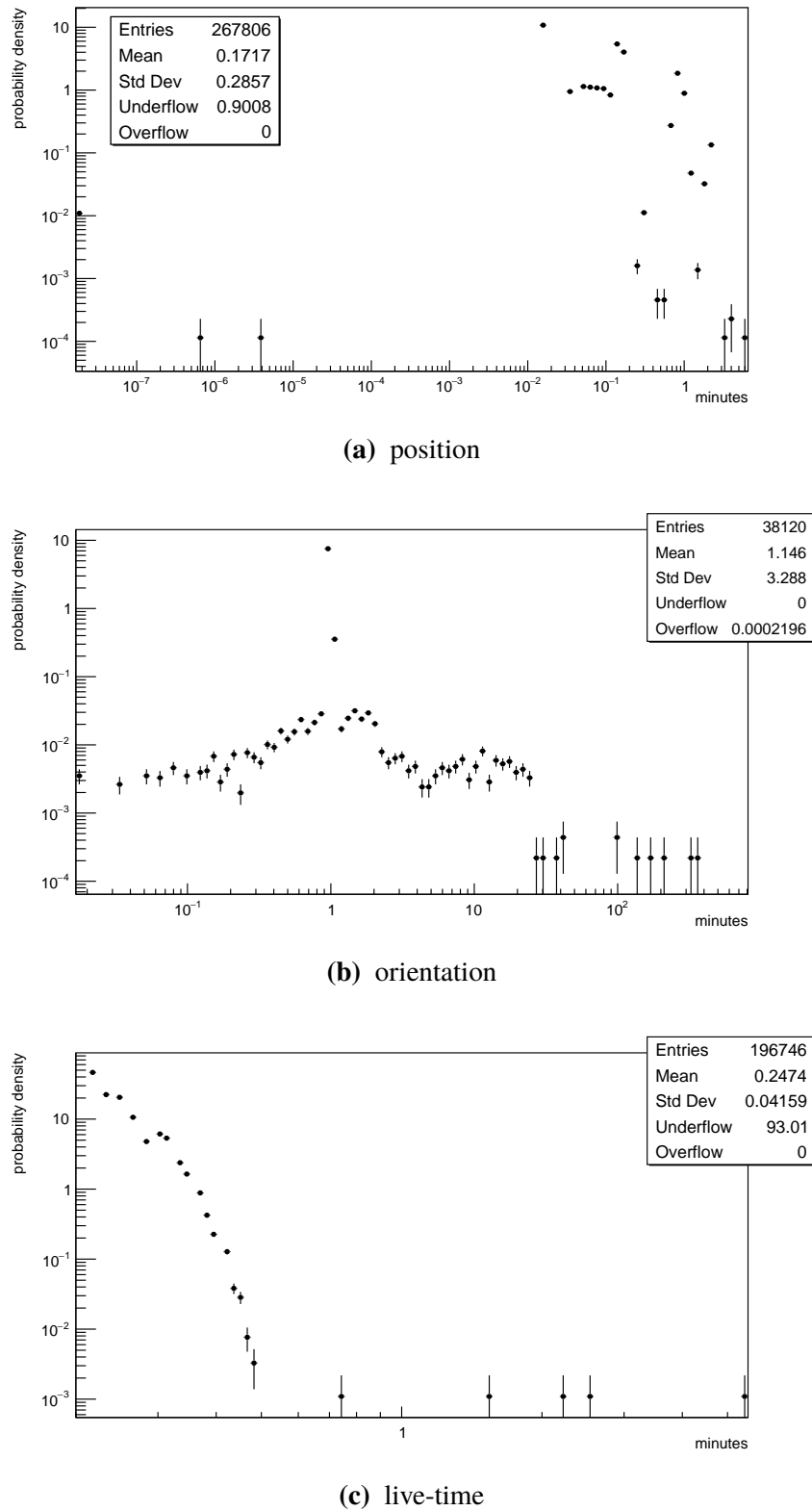


Figure 4.1: probability densities of time differences between consecutive records of AMI data of January, 2020.

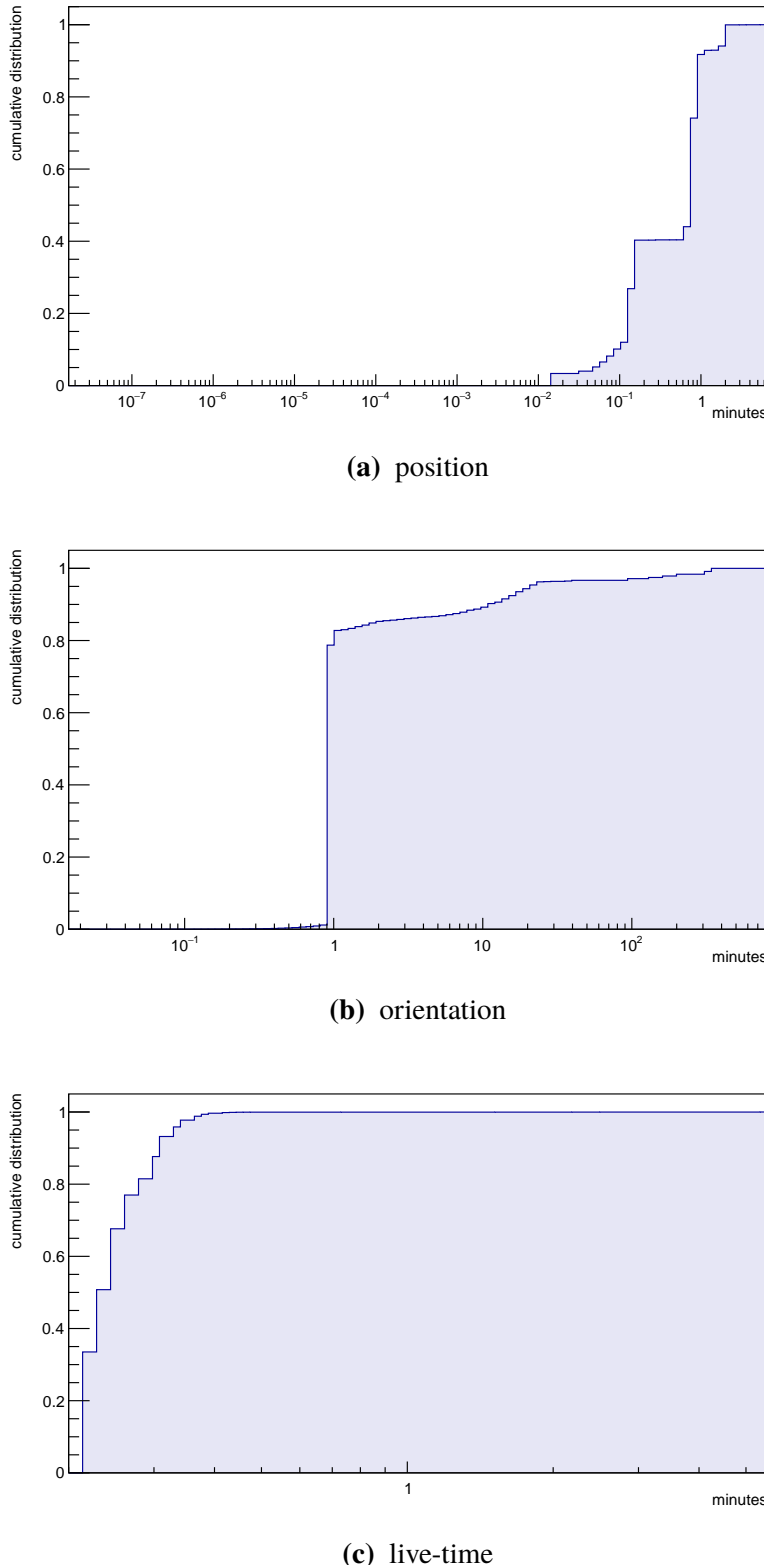
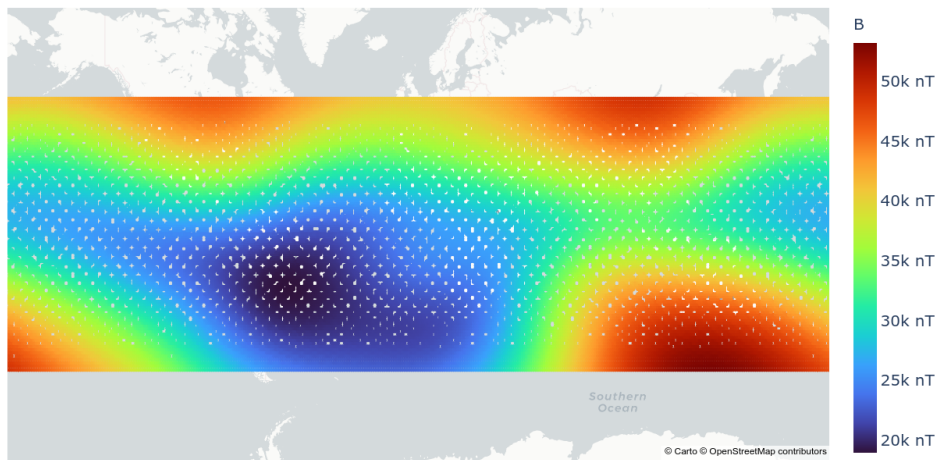
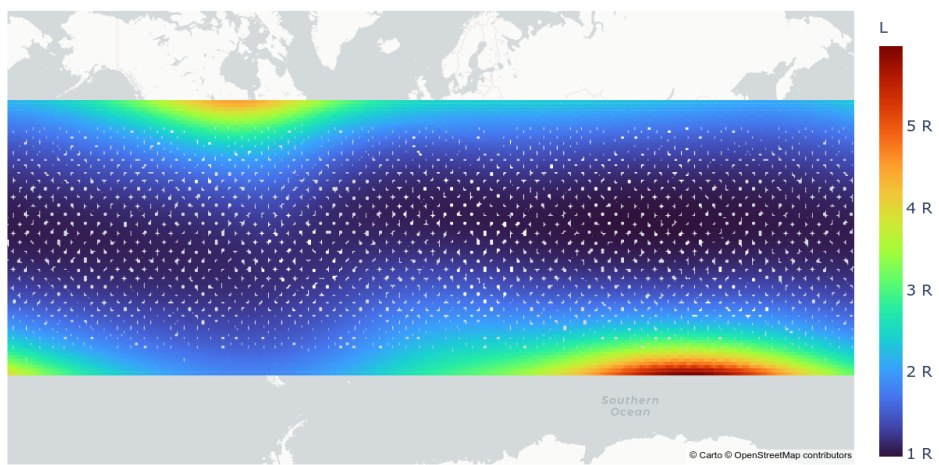


Figure 4.2: cumulative distributions of time differences between consecutive records AMI data of January, 2020.

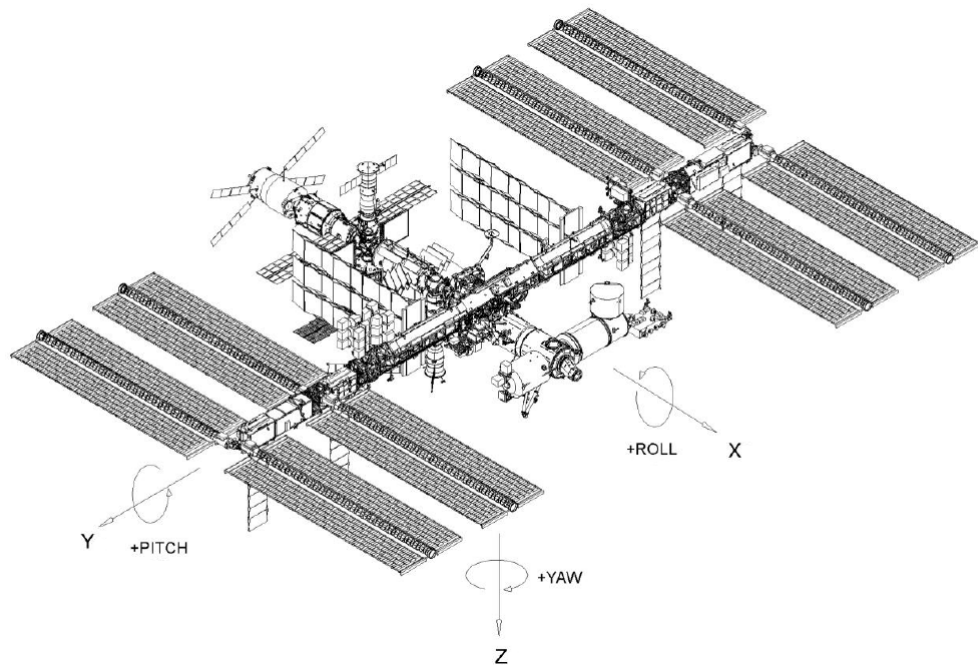


(a) geomagnetic field

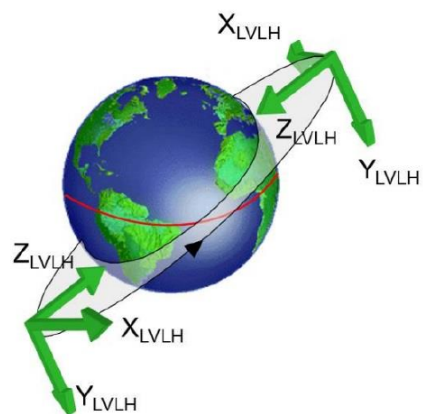


(b) L -values

Figure 4.3: maps of geomagnetic field intensities and L -values calculated for the ISS orbits of January, 2020. The values are averaged in cells $1^\circ \times 1^\circ$ of latitude and longitude. The relative errors are $\lesssim 4\%$.



(a) spacecraft view



(b) orbit view

Figure 4.4: LVLH reference system used by the ISS [134].

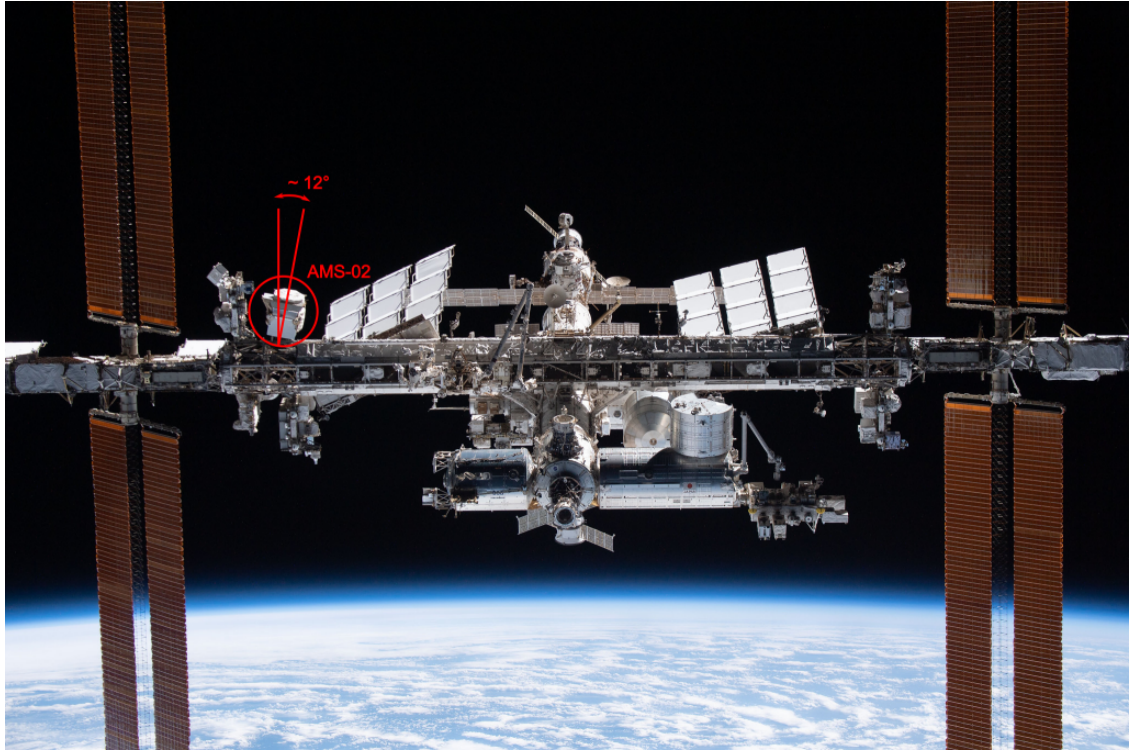


Figure 4.5: picture of the ISS [92, 94]. AMS-02 can be seen on the left with its inclination ($\sim 12^\circ$).

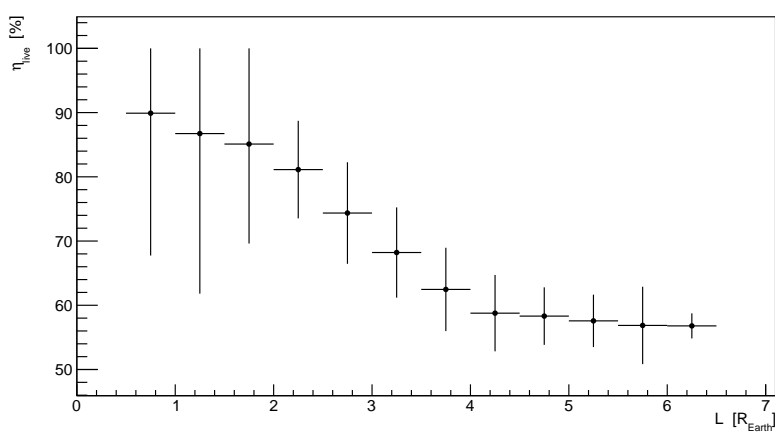
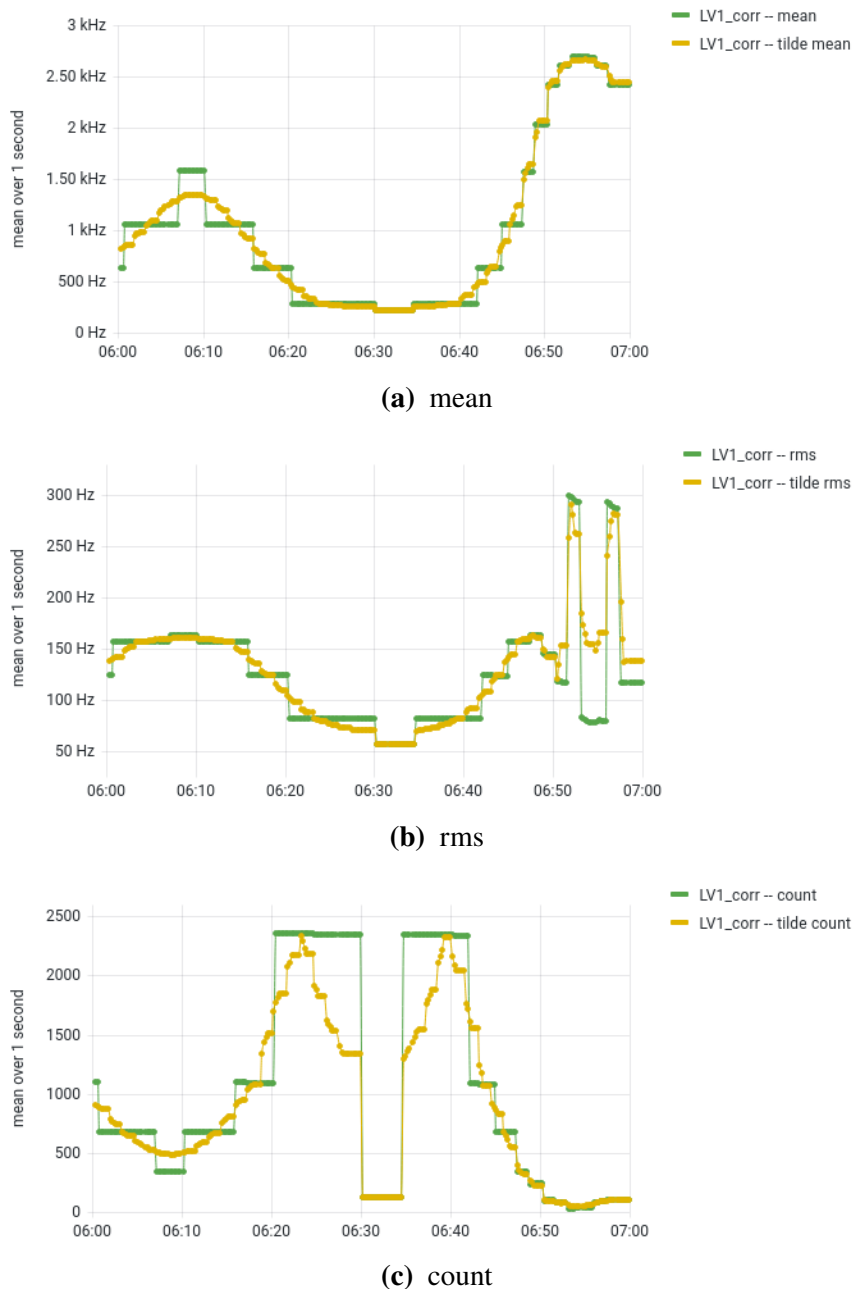


Figure 4.6: live-time collected in areas with different L -values during January, 2020. The error bars of live-time values show the rms of the complete distributions, reported in fig. A.1.



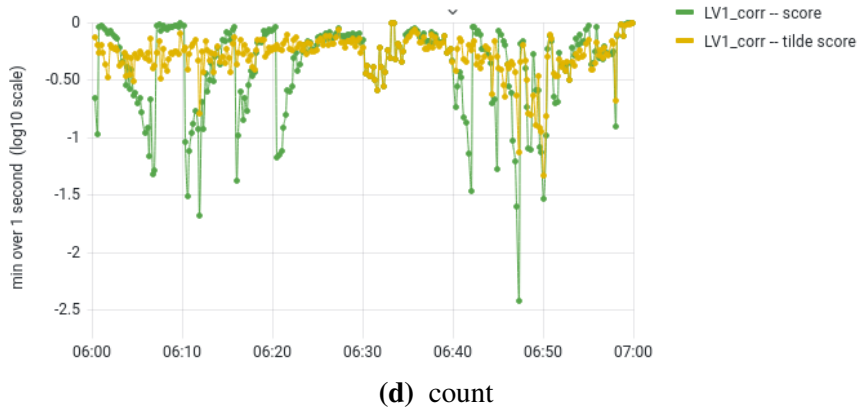


Figure 4.7: regular and tilde properties of the reference distributions computed for LV1 rate (correct by live-time) between 06:00 – 07:00 UTC of January 1, 2020 [135]. Reference distributions are collected considering the previous 3 days of data, binned in L $0.5 R_{\text{Earth}}$ wide and data points are averaged over 1 s. The greater linearity of tilde values make them less subject to over- and underestimations of rates excesses due to the binning of L -values. The ultimate effect on score can be seen in fig. 4.7d, where the tilde score time-series shows a more stable trend.

Chapter 5

Real-time monitoring of Solar Energetic Particles

The ISS is continuously occupied by astronauts. The geomagnetic field and the residual atmosphere shield the Station from cosmic radiation, but not always completely. The doses absorbed by the crew are currently monitored using dosimeters. The Alpha Magnetic Spectrometer mounted on the ISS measures CR flux continuously and can be effectively used to detect SEPs looking at its trigger rates, as seen in the previous chapter.

A real-time monitoring system can be realized taking advantage of AMS data, to provide an additional data source for radiation hazard monitoring. Such a system has been realized for the proof of this thesis and it is described in this chapter [135]. The system uses the identification algorithm described in the previous chapter, along with Kubernetes containers to run the analysis in real-time, an InfluxDB database to store the resulting data and a Grafana instance for SEP monitoring and alerts. The usage of InfluxDB and Grafana allows merging the system into the official AMI at a later time.

5.1 Quiet level definition

The identification algorithm presented in the previous chapter defines a nominal rate for each trigger to detect sudden excess not hardly explainable by statistical fluctuations. The definition of the quiet level is based on multiple parameters:

- the L -value bins used to group geomagnetic areas with similar properties;
- the length of the time interval of data taken into account for the nominal distributions;
- the filters applied on data to drop non-nominal measurements from the reference distributions.

The ISS completes an orbit in about 90 minutes and its precession in 16 orbits, following a periodicity of about 1 day. For the definition of the quiet levels, data from the precedent 3 days are taken into account, covering three times the period of ISS orbits. Then, measurements are aggregated in L -bins $0.5 R_{\text{Earth}}$ wide. Figure 5.1 shows the data collected in each bin for 3 days of data. Almost all bins contain more than 100 entries and are sufficiently populated to subdivide reference distributions. A greater statistics could be collected using a longer time range of data or increasing the size of the bins; generally the former should be favored, since grouping measurements with too different L -values could lead to the mixing of different nominal conditions.

Differently from the previous ones, the last bin is characterized by a lower statistics (less than 10 entries in a month of data). Increasing the time range covered up to 1 month would not solve the issue, so a larger bin (e.g. $[5.5, 6.5) R_{\text{Earth}}$) could be used to collect more statistics. However, a larger bin would reduce the granularity of the stepwise μ , σ , N and the power of their tilde values. Since tilde values use two bins at the same time, the removal of the bin $[6.0, 6.5) R_{\text{Earth}}$ would take away an important foothold for their calculus, in a region where the observation of SEPs is more frequent. Even if not statistically significant, the available information gives an indication on the nominal rate in high- L areas.

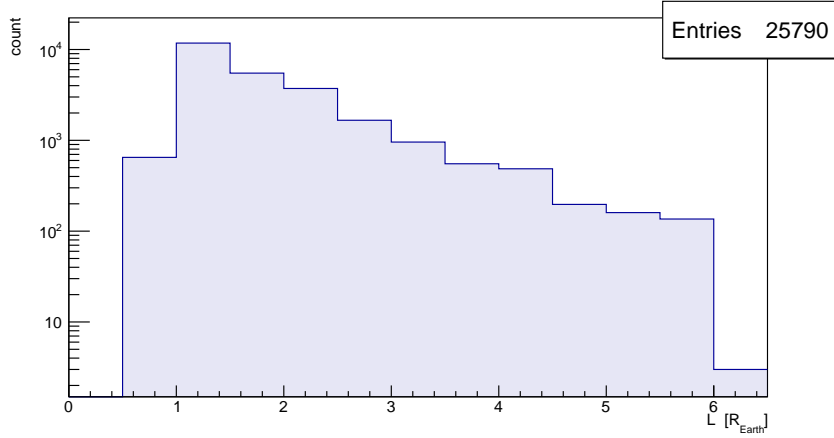


Figure 5.1: distribution of L -values for 3 days of AMS data collected during January 1–3, 2020. L bins are $0.5 R_{\text{Earth}}$ wide and present more than 100 entries except for the last bin ($L \geq 6 R_{\text{Earth}}$) characterized by a lower statistics (~ 10 entries per month).

The following cuts are applied on the data used for the quiet level definition:

$$B \geq 25000 \text{ nT} \quad (5.1a)$$

$$z \leq 15^\circ \quad (5.1b)$$

$$T_{\text{pos}} \leq 10 \text{ s} \quad (5.1c)$$

$$T_{\text{orient}} \leq 60 \text{ s} \quad (5.1d)$$

$$\forall i, \quad s_i \geq 10^{-6} \text{ s} \quad (5.1e)$$

with B geomagnetic field intensity, z zenith angle, $T_{\text{pos,orient}}$ maximum age of the last valid position and orientation and $s^{(i)}$ score assigned to the i -th trigger rate.

Geomagnetic field and zenith cuts

The cuts on the geomagnetic field and the zenith angle are used to exclude areas where AMS is not looking at the space but along the magnetic field lines. In particular, the geomagnetic field cut drops data collected in the SAA area, while the zenith cut drops data collected when the field of view of the instrument is more oriented towards the magnetic field lines rather than the space. In both cases, data taking conditions are not nominal, therefore should not enter in the statistics used for the quiet levels definition.

Positions and orientations age cuts

The requirements for T_{pos} and T_{orient} exclude entries where the values derived from position and orientation data (i.e. L -value, B , z) could not be reliable. Referring to figure 4.2a, two regimes can be seen for positions data periodicity: some entries have a period between 1 and 10 s, others between 40 and 70 s. In particular 40% of periods are within 10 s. Regarding the orientation data, figure 4.2b shows that 80% of entries are given within 60 s from the previous one. Therefore, 10 and 60 s are chosen as maximum periods for position and orientation values to minimize the error committed in the assessment of data taking environment without loosing too much of the original statistics.

Score cuts

The score cut is applied to avoid biasing the nominal distributions with non-nominal rates, due to the presence of a SEP. Since the score is defined using the p -value of a distribution, it can be seen as the probability to have a rate bigger than the one observed due to statistical fluctuations and not to the presence of a SEP. Measurements with a score less than 10^{-6} should be detected once every 1 million entries; considering an average period of ~ 15 s between data points (see fig. 4.1c), those correspond to almost half year of data.

5.2 Scoring

The set of scored trigger rates is kept as large as possible. Specifically, only `subLV1_6` is excluded, since it contains discrete values equal to 0 or 1 and does not provide any granularity in the provided information. While most of the trigger rates are scored using a normal distribution on the values divided by the live-time, `FTZ` and `subLV1_3` are modeled using Poisson distribution with the raw values. This is due to the very low rates of those two triggers, i.e. $\lesssim 10$ Hz.

Appendix A reports the distributions obtained for one month of trigger rates, divided per L bin. As it can be seen in those plots, normal and Poisson distribution are not always eligible to describe experimental data. Some of statistics partially show the overlap of two peaks, leading to the possible presence of two distinct regimes not separable just using the L -value. The scatter plots between one trigger rate or the live-time and the geomagnetic field intensity, the L -value, the ISS position, velocity and orientation do not show any particular trend to distinguish different behaviors. Ultimately, the L -values are maintained as the unique parameter used to characterize different data taking areas. However, a deeper investigation of this issue should be performed to find additional selectors.

5.3 Background subtraction

Not all excesses visible in the scores are connected to an actual SEP event. The main sources of background are the following:

1. apparent excesses and lacks near the L bin boundaries;
2. excesses related to the detection of particles trapped along the geomagnetic field lines;
3. records with an old information about position or orientation.

Source 1 is due to the stepwise trend of reference distributions properties and can be easily removed favoring the use of tilde scores over the regular ones.

Source 2 can be easily excluded applying the same cuts on the geomagnetic field intensity and the zenith angle for the quiet level definition, i.e. equations 5.1a and 5.1b.

Aged information about position and orientation can take to a mis-evaluation of the actual L -value and zenith, subsequently leading to a mis-identification of the correct L bin and corresponding quiet level or an ineffective application of the zenith angle cuts. Both sources of error can be excluded applying the cuts used in quiet level definition, i.e. equations 5.1c and 5.1d.

Results of the cuts applied to remove sources 2 and 3 are shown in figure 5.2.

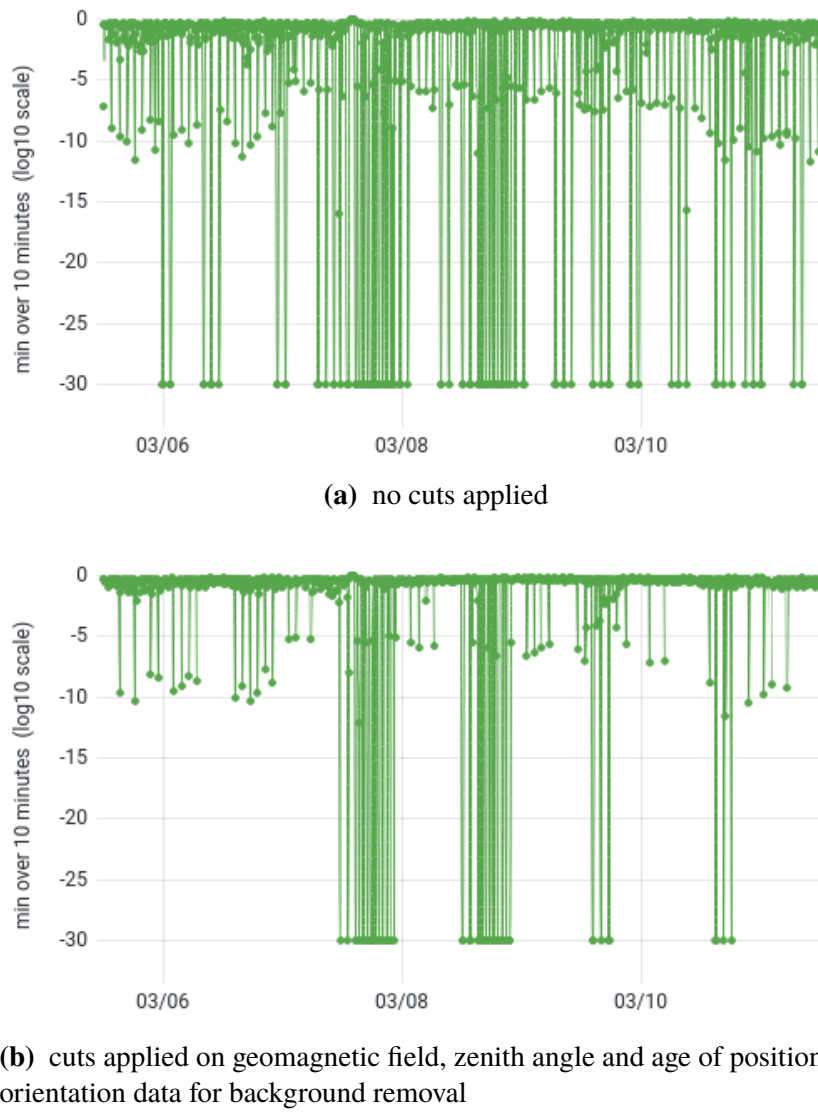


Figure 5.2: FT tilde scores for the SEP event of March 7–8, 2012 (ref. to tab. B.1) [135]. Sub-figures show the tilde score time-series without and with standard cuts applied on geomagnetic field, zenith angle and ages of position and orientation data for background removal. Plot 5.2a shows more excesses the ones shown by 5.2b, where only the peaks related to the SEP event are visible. Both plots show minimum values over 10 minutes time intervals on a logarithmic scale; null scores, due to very large deviations from the nominal level, are replaced by 10^{-30} .

Trigger LV1 shows a peculiar behavior with respect to the others. This trigger is much noisier,

considering the SEP event of March 7–8, 2012 (ref. to tab. B.1), the background can be completely removed imposing

$$L \leq 1.5 R_{\text{Earth}} \quad (5.2)$$

Figure 5.3 shows the effect of the cut 5.2 in a SEP event.

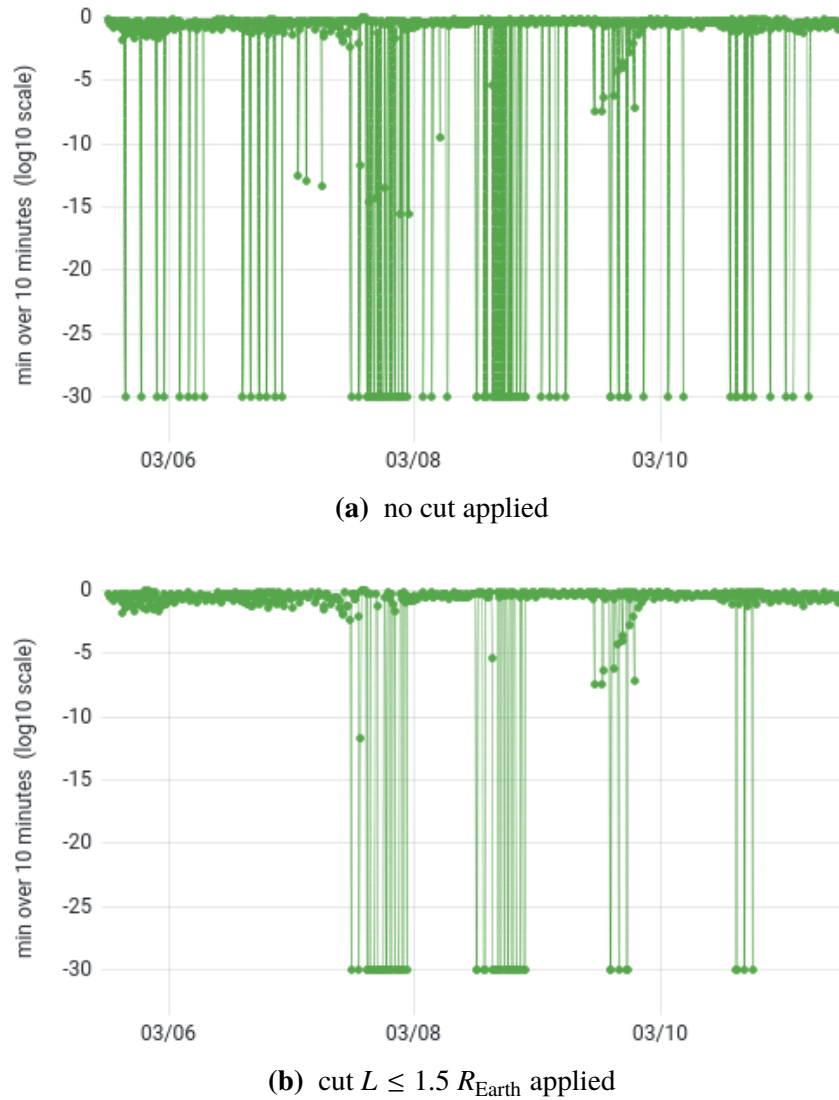


Figure 5.3: LV1 tilde scores for the SEP event of March 7–8, 2012 (ref. to tab. B.1) [135]. Sub-figures show the tilde score time-series without and with an additional cut on L -values, beyond the standard ones applied for background removal on geomagnetic field, zenith angle and ages of position and orientation data. Plot 5.3a shows more excesses with respect of the ones shown by 5.3b, where only the peaks related to the SEP event are visible. Both plots show minimum values over 10 minutes time intervals on a logarithmic scale; null scores, due to very large deviations from the nominal level, are replaced by 10^{-30} .

Figure C.2 shows the complete regular score time-series for the LV1 trigger, with the application of the cuts described so far. The plots of the figure still show some excesses not related to any SEP event. The cuts applied remove a big part of the background, but not all of it. Therefore, further investigation must be performed to increment the rejection of the system.

5.4 Event detection

Figure C.1 shows a SEP event that took place in March 7–8, 2012 (ref. to tab. B.1). During the event, the detector has not stayed always in a region with a rigidity cutoff smaller than the one of the SEPs; because of that the event leaves three peaks instead of one in the tilde score time-series. Taking into account also other events, FTE shows the same inaccuracy visible in the considered event. FTE is focused on the detection of electromagnetic particles and SEPs are mostly hadronic (i.e. protons) therefore its inadequacy in event identification makes sense. All of other rates show the first two peaks but the last excess, i.e. the weakest, is not found in subLV1_3, subLV1_4, subLV1_5 and is more reduced in FTZ.

5.5 Real-time monitoring

The real-time monitoring takes advantage of 6 Kubernetes containers that run as many instances of the analysis package to fill the backend database. All fillers queries data on AMI with timestamps in $[\bar{t} - 1 \text{ min}, \bar{t}]$ every minute; considering t_0 the time the query is performed, $\bar{t} = t_0 - t_{\text{delay}}$, where t_{delay} is different for each instance. Then, the following fillers are used:

1. *edge-filler*, with $t_{\text{delay}} = 0$;
2. *delayed-30s-filler*, with $t_{\text{delay}} = 30 \text{ s}$;
3. *delayed-1m-filler*, with $t_{\text{delay}} = 1 \text{ min}$;
4. *delayed-2m-filler*, with $t_{\text{delay}} = 2 \text{ min}$;
5. *delayed-5m-filler*, with $t_{\text{delay}} = 5 \text{ min}$;
6. *delayed-1h-filler*, with $t_{\text{delay}} = 1 \text{ h}$.

AMI feeder saves entries at the end of 1-minute intervals, therefore real-time data is not immediately available. In addition, the ISS looses the connection to Earth during its orbit for periods no longer than 20–30 minutes; during these times, records are buffered and sent after the re-establishment of the connection. Data collected by the filler delayed by 1 hour is not influenced by those events, so can be used as reference to evaluate the efficiency of the other fillers. Considering that, the real-time filler loses $\sim 80\%$ of data, the one delayed by 30 seconds $\geq 70\%$, by 1 minute $\geq 60\%$ and by more 2 minutes $\leq 20\%$ (see fig. 5.4). The big gap between the efficiencies of the fillers delayed by 1 minute or less and by 2 minutes or more can be explained considering the periodicity of the AMI database feeder, i.e. $\sim 1 \text{ minute}$. Therefore, fillers delayed by 2 and 5 minutes show data losses only related to the lack of connection between ISS and the ground, while the others suffer mostly of the delays of the AMI feeder.

The main measurement of the backend database is fed by all fillers simultaneously. Entries written by a filler are overwritten at a later time by the more delayed ones. In this way, the database ends up containing the most complete data, without loosing the possibility of performing real-time operations on less accurate records.

5.6 Alert system

Grafana provides a trigger system that evaluates user-defined alert rules periodically, registering the state of the alerts. External connections can be arranged to transfer alerts to other locations.

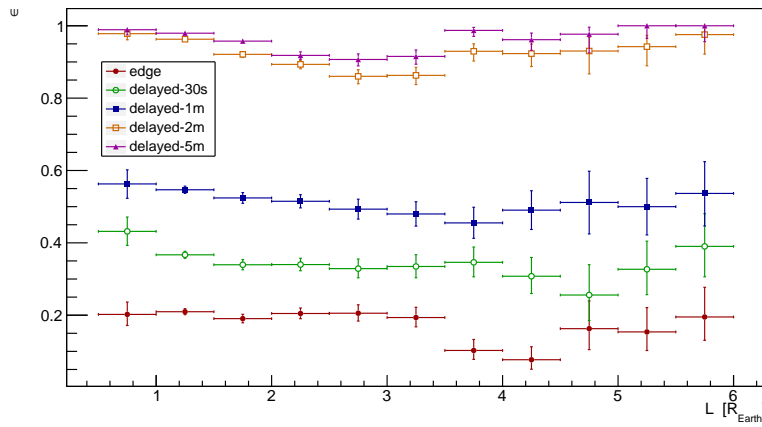


Figure 5.4: efficiency of the fillers used in the real-time monitoring system [135]. Processed data refer to the period May 10–20, 2023 and are binned in L -value using the same resolution of quiet level evaluation. Efficiencies are estimated using the counts of the filler delayed by 1 hour. The efficiency increases with the delay used, in particular with no delay $\lesssim 20\%$ of data are collected, using 30 seconds 20–30%, 1 minute 40–60% and more than 2 minutes $\gtrsim 80\%$.

Currently, the built real-time monitor stores alerts locally, leaving the implementation of a more powerful system to a later time.

The grafana instance located at [135] implements a rule shown in alg. 5.1. The rule is evaluated every 10 s on trigger rates observed in $[\text{now} - 70 \text{ s}, \text{now} - 60 \text{ s}]$ and the standard cuts described in section 5.3 are applied for background removal. All trigger rates are evaluated, except for FTE, since its insensitivity to SEP events. Actual real-time measurements are not considered by the alert because of the data losses described in the previous section.

Query q_1

```

SELECT: tilde score
WHERE
    time ∈ [now – 70 s, now – 60 s]
    && trigger = LV1_corr
    && L ≥ 1.5 REarth
    && B ≥ 25000 nT
    && z ≤ 15°
    && Tpos ≤ 10 s
    && Torient ≤ 60 s

```

Query q_2

```

SELECT: tilde score
WHERE
    time ∈ [now – 70 s, now – 60 s]
    && trigger ≠ LV1_corr
    && trigger ≠ FTE_corr
    && B ≥ 25000 nT
    && z ≤ 15°
    && Tpos ≤ 10 s
    && Torient ≤ 60 s

```

Alert: $\min(q_1) \leq 10^{-6} \parallel \min(q_2) \leq 10^{-6}$

Algorithm 5.1: alert rule for SEP events defined in Grafana real-time monitor [135]. Alert rule is evaluated every 10 s and takes two queries in input. An actual alert is fired if the minimum values of one of the two input time-series is below 10^{-6} . Analyzed data are taken in $[now - 70\text{ s}, now - 60\text{ s}]$ to account data losses described in sect. 5.5. Cuts applied on L -values, geomagnetic field intensities (B), zenith angles (z) and position and orientation data ages ($T_{\text{pos,orient}}$) are used to remove the background (ref. to sect. 5.3). All triggers are evaluated by the alert except for FTE.

Conclusions

The goal of this thesis was the developing of a real-time monitor for Solar Energetic Particle (SEP) events using the Alpha Magnetic Spectrometer (AMS) mounted on the International Space Station (ISS).

The ISS orbits in the Low Earth Orbit (LEO) and is continuously occupied by astronauts. The spacecraft is partially shielded from cosmic radiation by the residual atmosphere and the geomagnetic field. However, that protection is not effective against all charged particles at every time, therefore the radiation doses absorbed by the crew is monitored using dosimeters. The solar activity can produce unpredictable bursts of energetic particles, the Solar Energetic Particles (SEPs), with energies between 10 keV and several GeV, that can last for hours or even days. Intense events represent an hazardous source of radiation and their monitoring is needed for carrying out space activities in safety.

The Alpha Magnetic Spectrometer (AMS) is mounted on the ISS since 2011 and measures CR flux continuously. Faldi et al. show in [8] how it is possible to detect SEPs just using the trigger rates of AMS. Currently the presence of sudden intense events, can be highlighted by the increasing doses measured over time by ISS dosimeters, but this kind of monitoring is not so powerful and can be enhanced using AMS data.

Given all the previous aspects, this thesis focused on the proof of the possibility to monitor in real-time SEPs near the ISS. First chapters gave references on CRs, SEPs and AMS detectors (chapters 1–3). Then, chapter 4 described the algorithm developed for the identification of SEPs in AMS trigger rates. Finally, chapter 5 presented the real-time monitor built.

The detection algorithm recognizes SEPs using the sudden excesses registered in AMS trigger rates. The quiet level evaluation is done using a moving buffer that collects processed entries to analyze the following ones. Nominal conditions are not constant along the ISS orbit, so buffered data are grouped using the McIlwain's parameter L , uniquely related to the rigidity cutoff. Then, the mean and the rms of the distributions are computed and used to assess a score to the measured rate. In particular, each trigger rate is modeled using a normal or a Poisson PDF on the basis of their rates and the score is obtained using the right-tailed p -value. Ultimately, rate excesses correspond to low scores ($s \rightarrow 0$) and decreases to high scores ($s \rightarrow 1$). The detection algorithm also provides a tilde version of the score, where the mean and the rms used in the calculus are obtained as from the linear interpolation between the reference distributions of two bins. The tilde value decreases the error introduced by the choice of the L scale binning and so it is favored over the regular score in SEPs detection.

AMS Monitoring Interface (AMI) provides storage and real-time access to AMS data. An InfluxDB database is used to store time-series data and a Grafana instance, on top of it, provides access and data visualization. The real-time monitor built for the validation of this thesis runs the developed algorithm on the entries of the AMI database, stores the results in a dedicated InfluxDB database and attaches another Grafana instance to it. With this configuration, the realized system reproduces the same structure of the official AMI and can be tested for a later implementation of the data processed by the custom algorithm into the original database. The ultimate outcome of the

realized system is a functioning real-time monitor for the detection of SEP events using trigger rates of AMS instrument. In particular, all trigger rates show increments in presence of an intense SEP event, except for the FTE. Then, a basic alert system was implemented using the features provided by Grafana to perform a local trigger on processed data for possible SEPs detected in real-time.

An issue that affects the real-time monitoring, is the discrepancy between the nominal distributions used, i.e. normal and Poisson and the experimental ones. Not all L -value bins can be properly modeled, therefore a deeper analysis is suggested to find out new indicators for the nominal conditions definition of the data taking area. In addition, the cuts defined for background removal are not definitive, therefore a further study of the data is needed to increase the rejection of the system.

The performance of the monitor is also affected by the inefficiencies of data retrieval from the AMI database. The periodicity of the AMI feeder and interruptions of connection of the ISS with ground introduce delays in the data storing, making real-time alerts unreliable. A solution to this problem could be the placement of data analysis at a higher level in the transmission chain, e.g. upstream the ISS-Earth data flow. In that case, the detection algorithm should be re-arranged to read AMS raw data stream and to transfer results through ISS communications.

The provided system can be enhanced enlarging the input dataset. Currently, only AMS triggers are taken into consideration, thanks to their low latency, needed for a real-time monitoring. However, AMS is a complete CR detector and provides much more information. AMI database can be further investigated for other measurements useful in the recognition of SEPs.

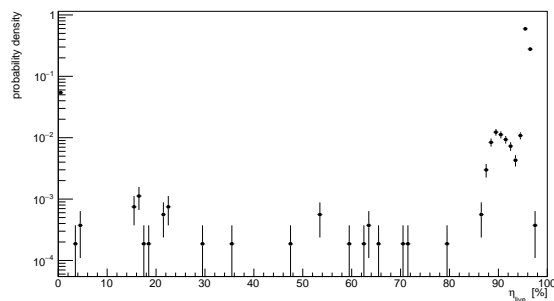
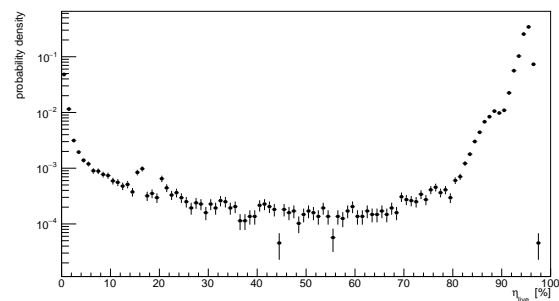
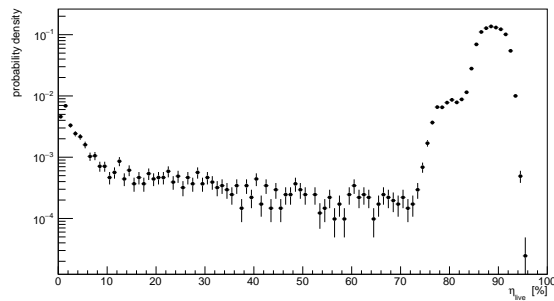
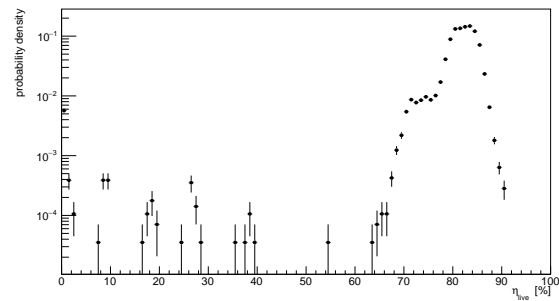
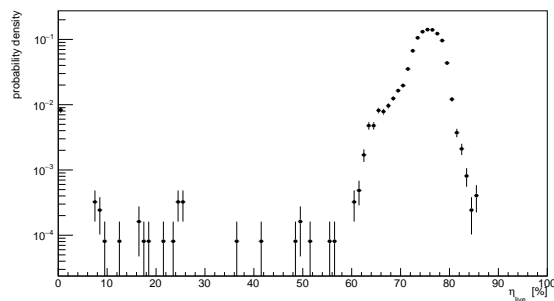
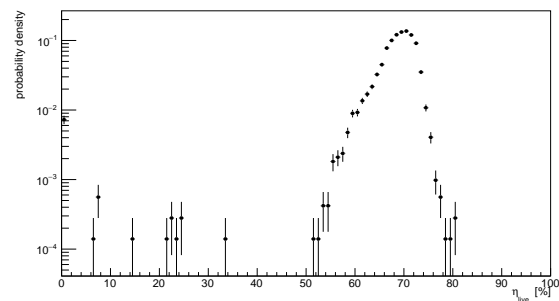
In case of an implementation of the data processing on board of the ISS, a lightweight alert system can be prepared. Real-time alerts fired directly on the spacecraft without the need of data transfer to ground would be much more efficient for astronauts protection against radiations.

The detection algorithm only looks for single excesses in the trigger rates. However, due to the continuous variation of the L -value, one SEP event can rise multiple non-consequent peaks in the rates. This behavior can be characterized evaluating the minimum sensitive L -value and aggregating consecutive excesses above that value to a single event. Furthermore, a predictive algorithm can be designed to estimate when the next excess will occur, how much high will be and when the event is about to stop. Such an algorithm would need an accurate propagation of the ISS orbit, to predict the L -values and also a detailed characterization of the effect of a SEP event on the triggers. Such a work could also use Machine Learning (ML) to achieve great predictive power, but at the expense of the physics comprehension.

To conclude, this thesis successfully proofed how it is possible to monitor in real-time SEP events using the trigger rates of AMS on the ISS. As described above, there are many ways to further develop the presented work and its implications on space activities makes it worth of further research, also in view of the future space missions.

Appendix A

AMS live-time and triggers

(a) $L \in [0.5, 1.0] R_{\text{Earth}}$ (b) $L \in [1.0, 1.5] R_{\text{Earth}}$ (c) $L \in [1.5, 2.0] R_{\text{Earth}}$ (d) $L \in [2.0, 2.5] R_{\text{Earth}}$ (e) $L \in [2.5, 3.0] R_{\text{Earth}}$ (f) $L \in [3.0, 3.5] R_{\text{Earth}}$

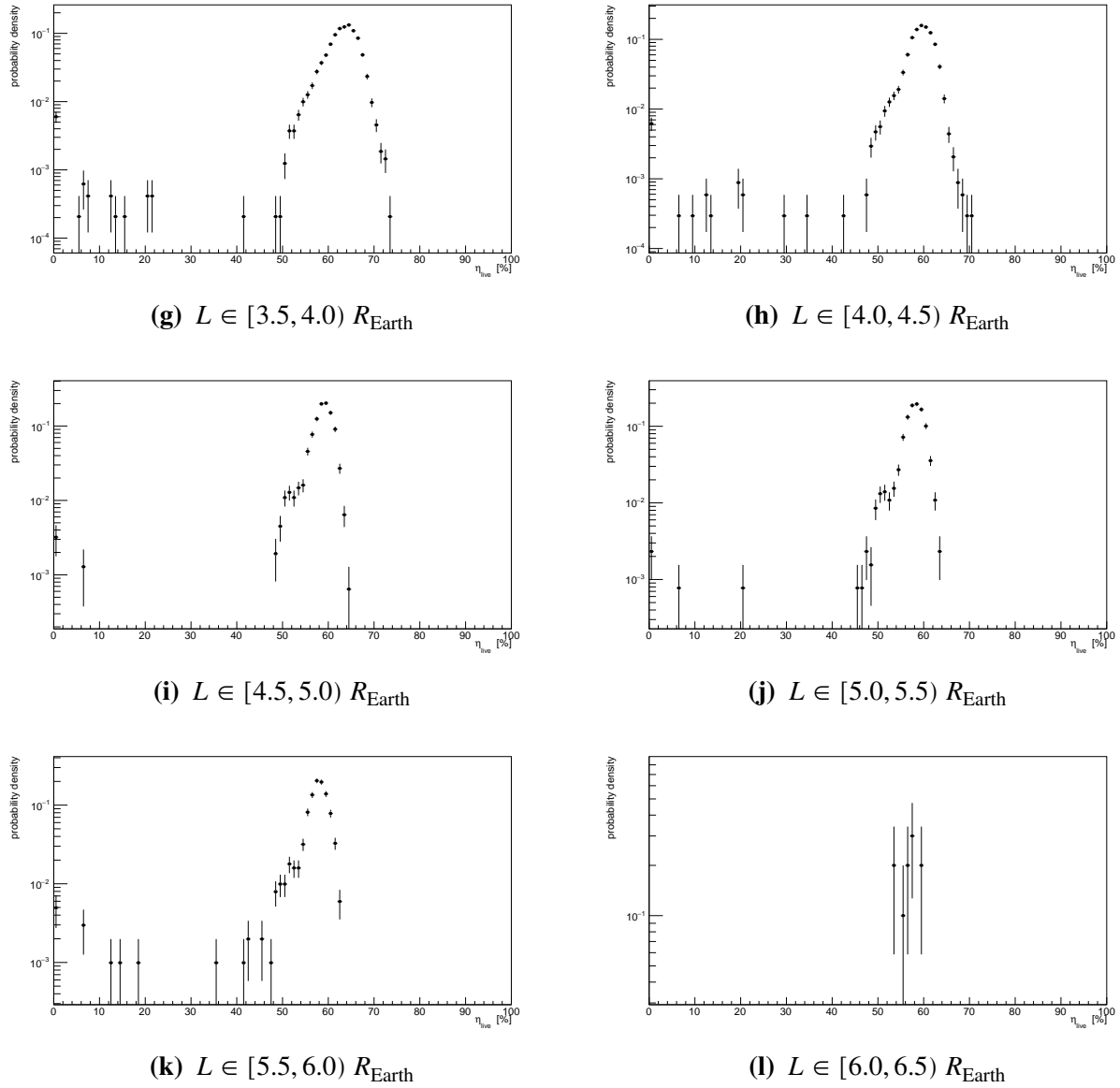
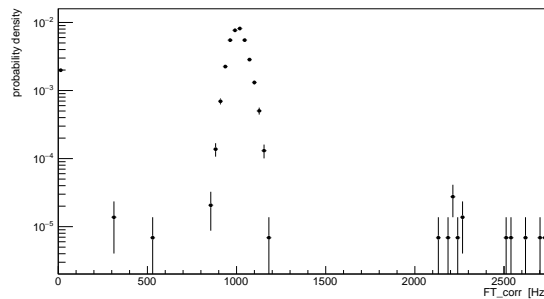
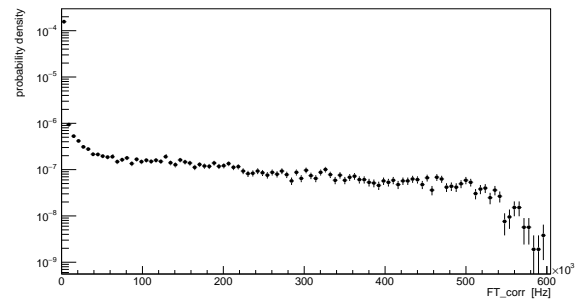
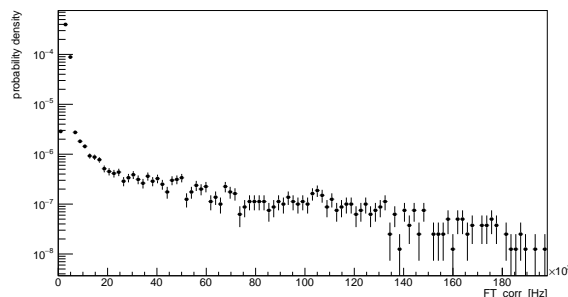
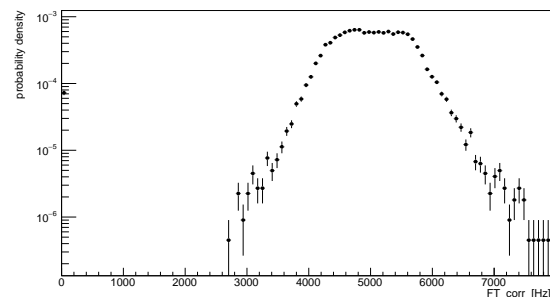
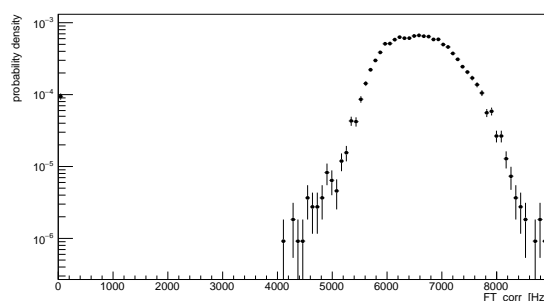
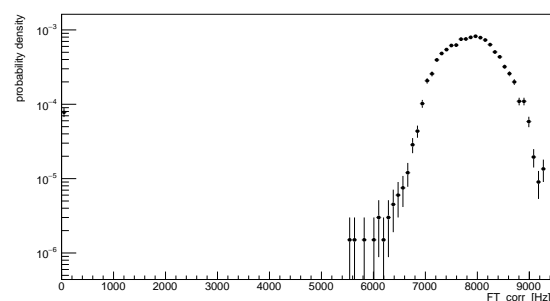


Figure A.1: distributions of AMS-02 live-time for different L -values during January, 2020.

(a) $L \in [0.5, 1.0] R_{Earth}$ (b) $L \in [1.0, 1.5] R_{Earth}$ (c) $L \in [1.5, 2.0] R_{Earth}$ (d) $L \in [2.0, 2.5] R_{Earth}$ (e) $L \in [2.5, 3.0] R_{Earth}$ (f) $L \in [3.0, 3.5] R_{Earth}$

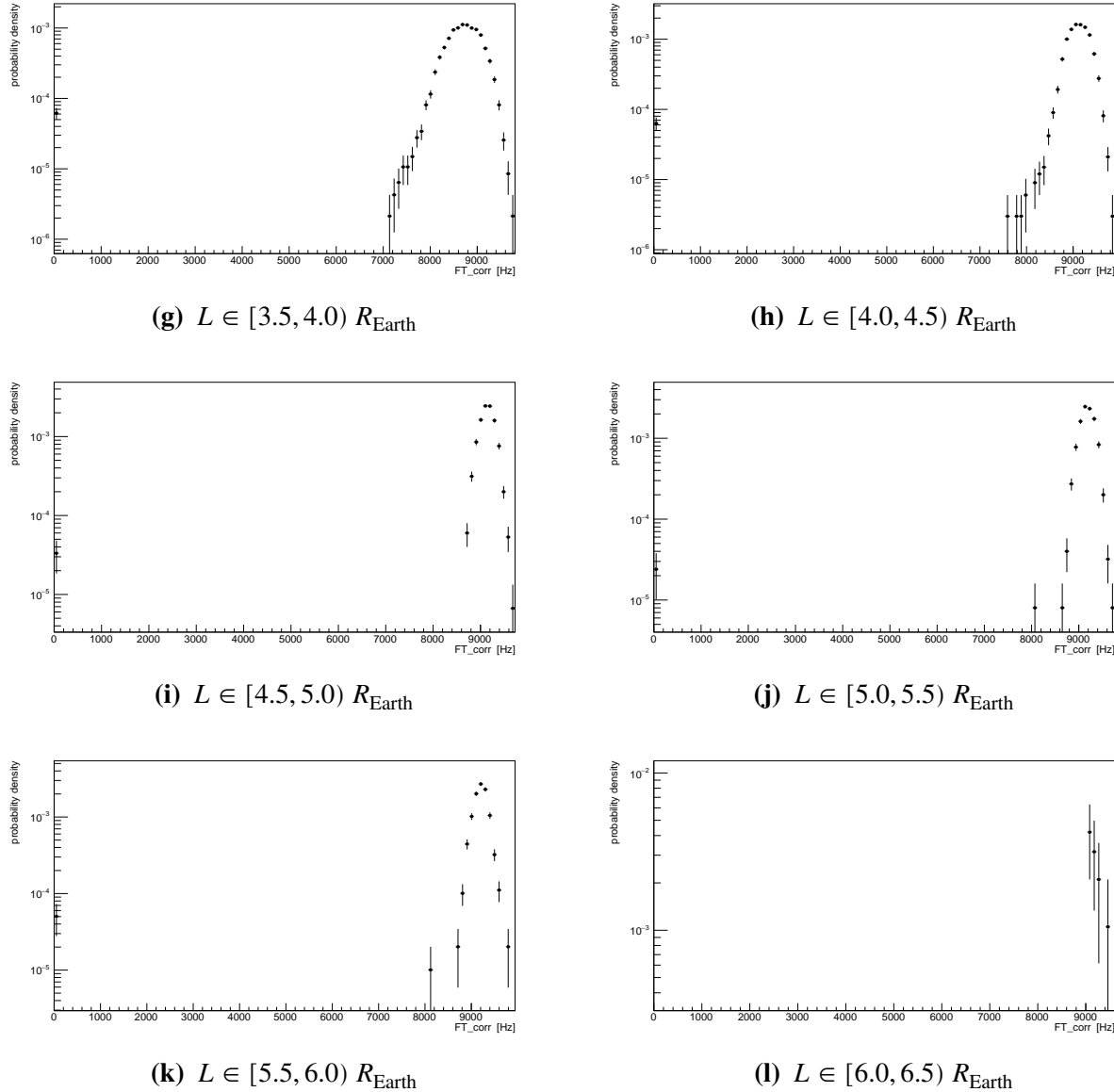
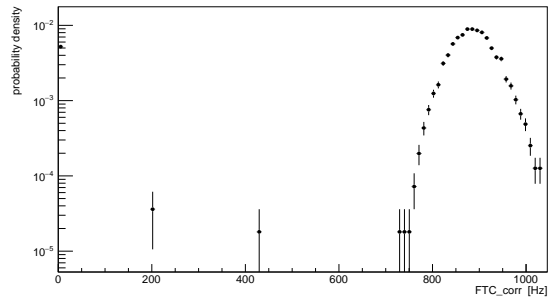
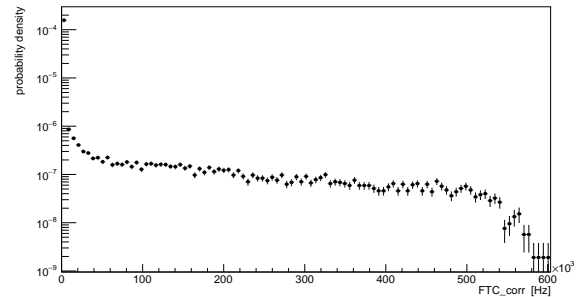
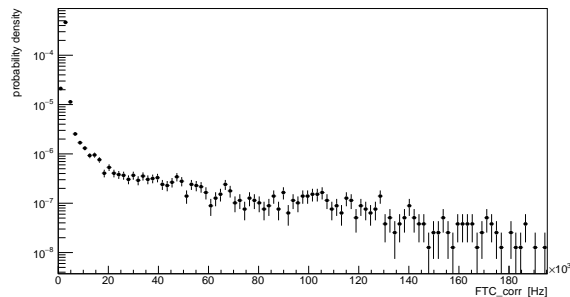
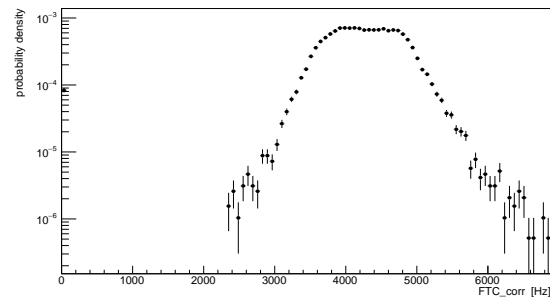
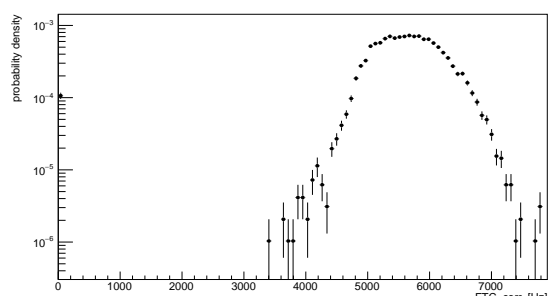
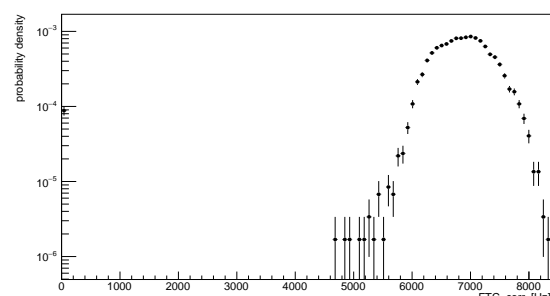


Figure A.2: distributions of AMS-02 trigger rate FT (corrected by the live-time) for different L -values during January, 2020.

(a) $L \in [0.5, 1.0] R_{\text{Earth}}$ (b) $L \in [1.0, 1.5] R_{\text{Earth}}$ (c) $L \in [1.5, 2.0] R_{\text{Earth}}$ (d) $L \in [2.0, 2.5] R_{\text{Earth}}$ (e) $L \in [2.5, 3.0] R_{\text{Earth}}$ (f) $L \in [3.0, 3.5] R_{\text{Earth}}$

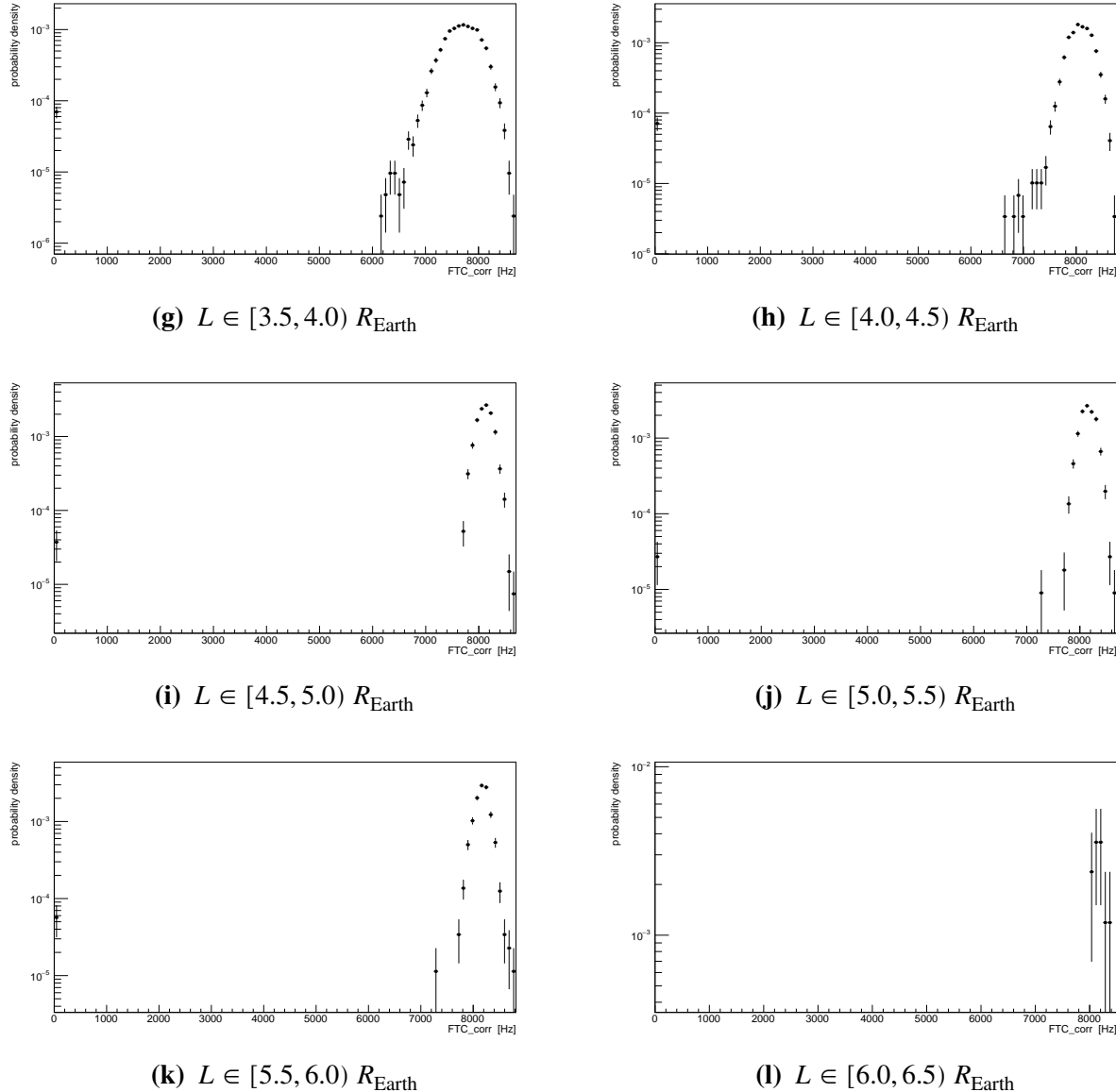
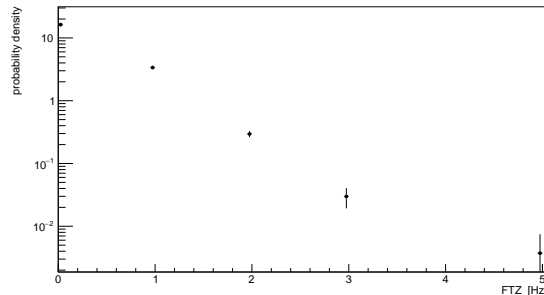
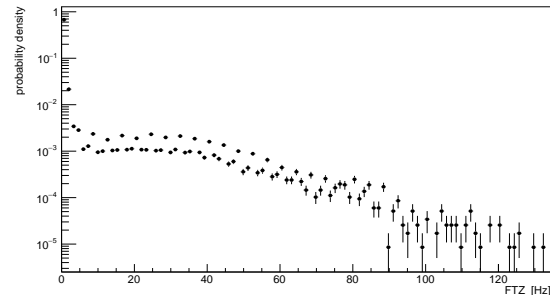
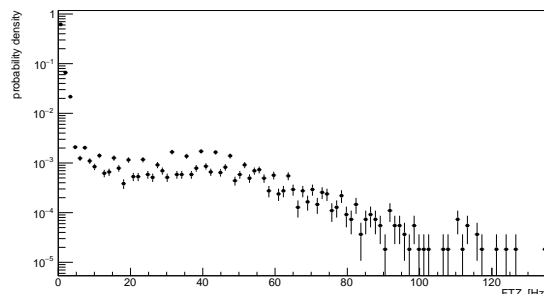
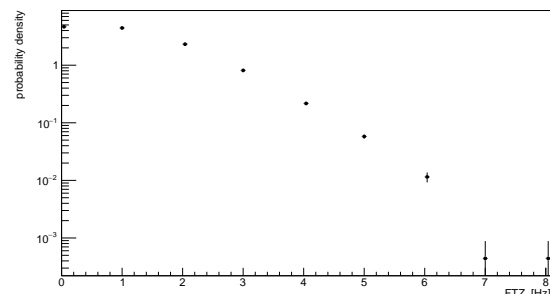
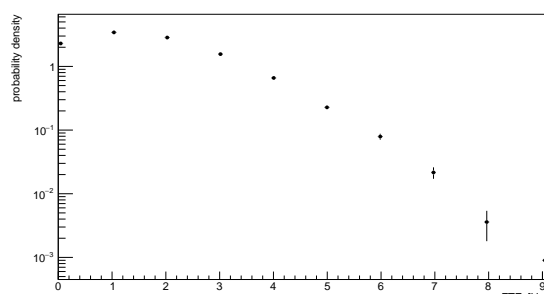
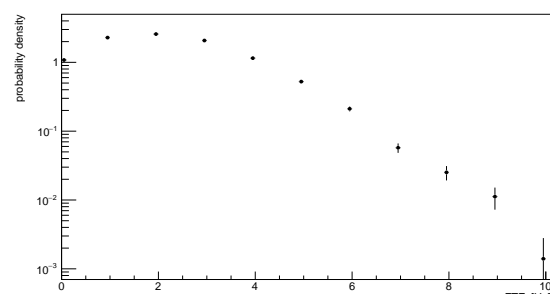


Figure A.3: distributions of AMS-02 trigger rate FTC (corrected by the live-time) for different L -values during January, 2020.

(a) $L \in [0.5, 1.0] R_{\text{Earth}}$ (b) $L \in [1.0, 1.5] R_{\text{Earth}}$ (c) $L \in [1.5, 2.0] R_{\text{Earth}}$ (d) $L \in [2.0, 2.5] R_{\text{Earth}}$ (e) $L \in [2.5, 3.0] R_{\text{Earth}}$ (f) $L \in [3.0, 3.5] R_{\text{Earth}}$

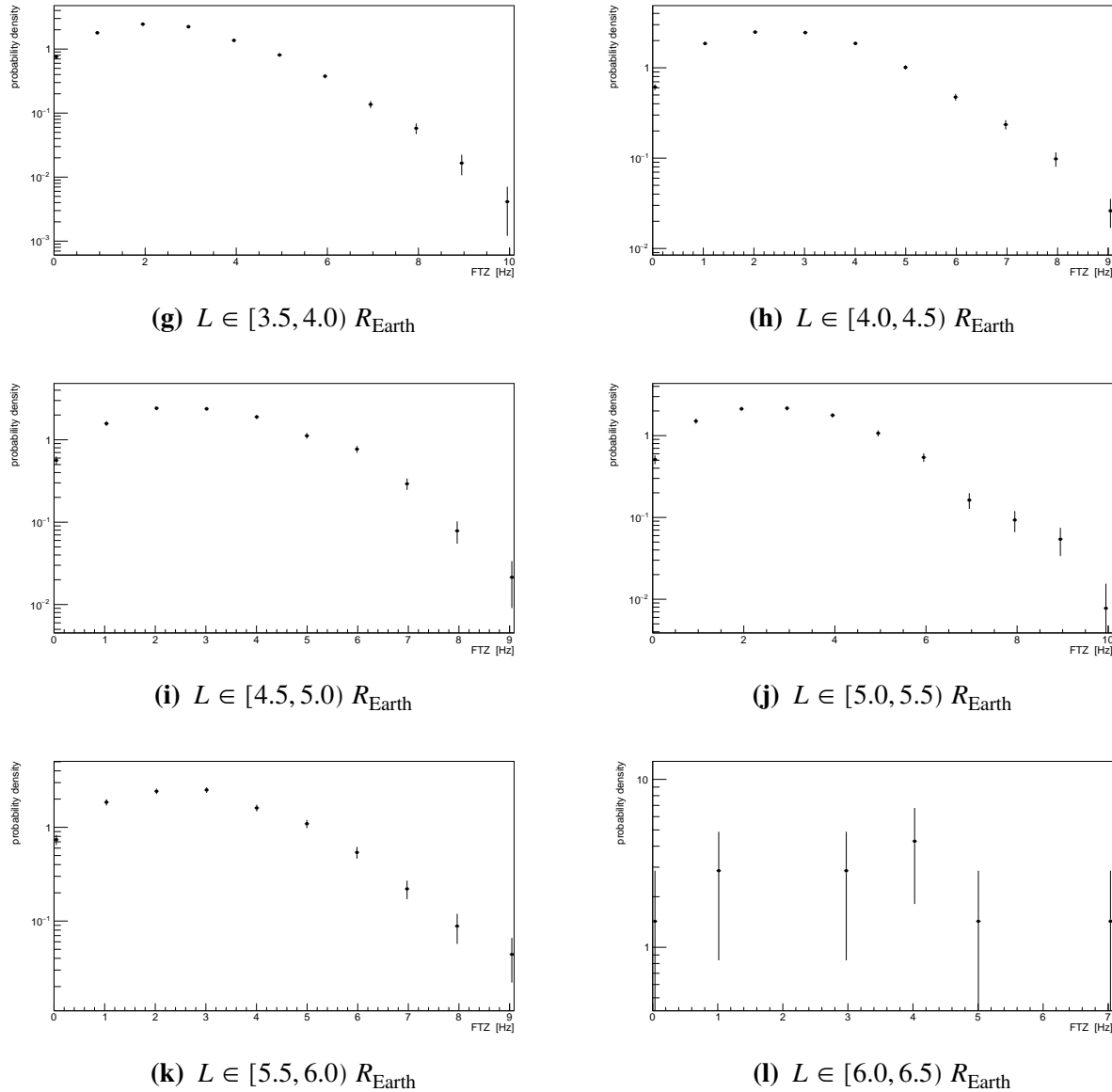
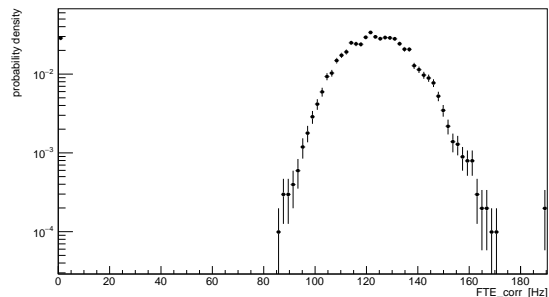
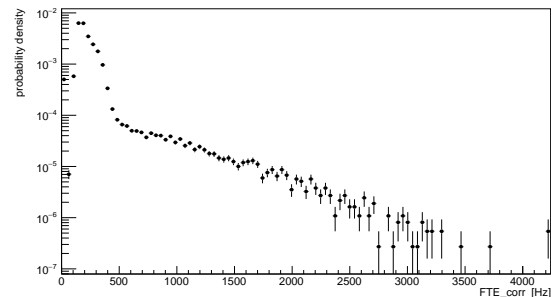
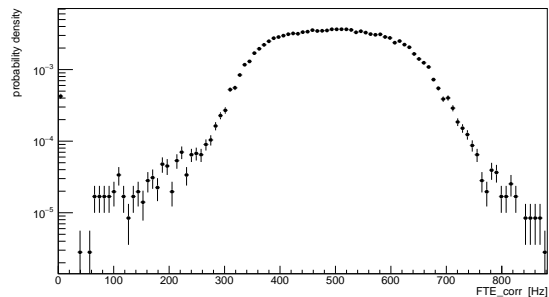
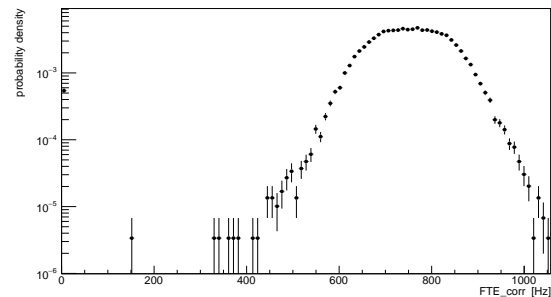
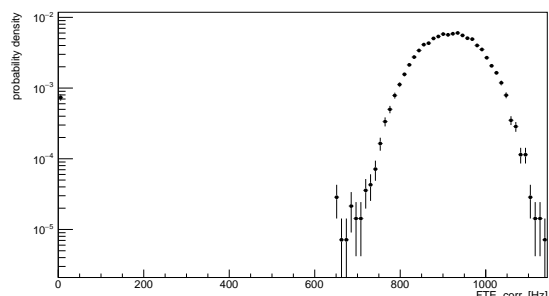
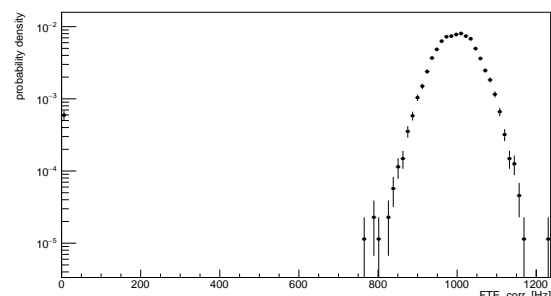


Figure A.4: distributions of AMS-02 trigger rate FTZ (raw) for different L -values during January, 2020.

(a) $L \in [0.5, 1.0] R_{\text{Earth}}$ (b) $L \in [1.0, 1.5] R_{\text{Earth}}$ (c) $L \in [1.5, 2.0] R_{\text{Earth}}$ (d) $L \in [2.0, 2.5] R_{\text{Earth}}$ (e) $L \in [2.5, 3.0] R_{\text{Earth}}$ (f) $L \in [3.0, 3.5] R_{\text{Earth}}$

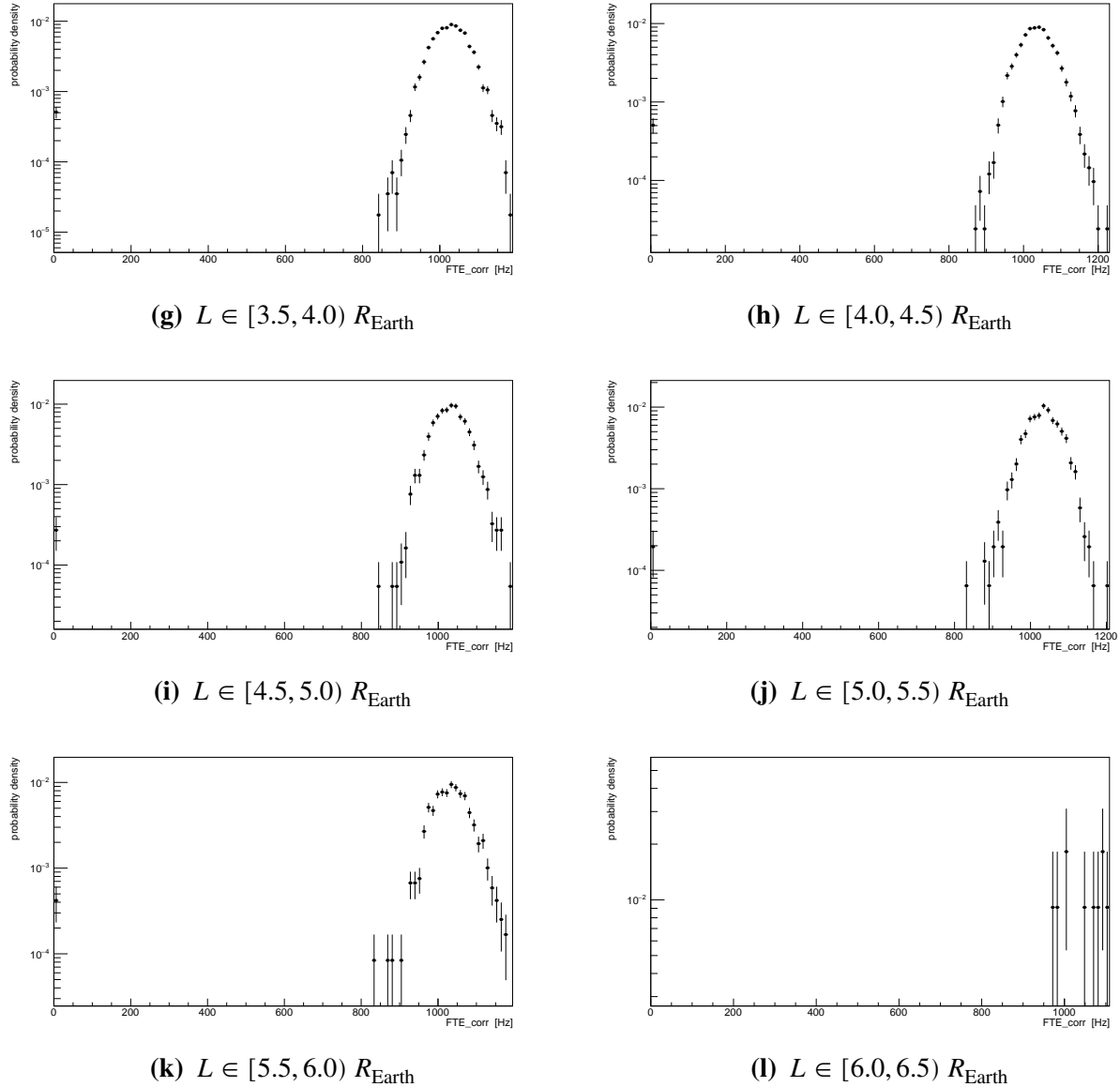
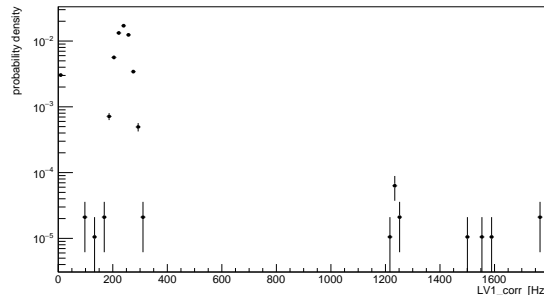
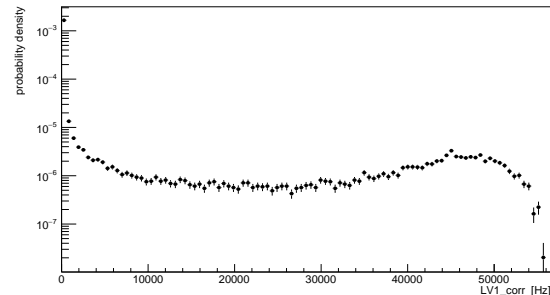
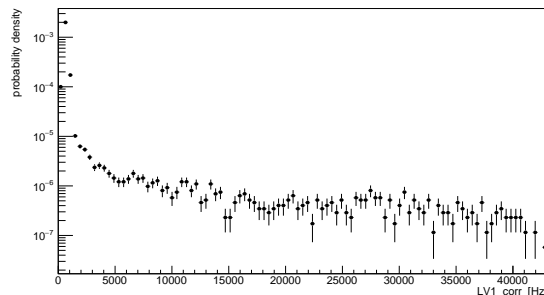
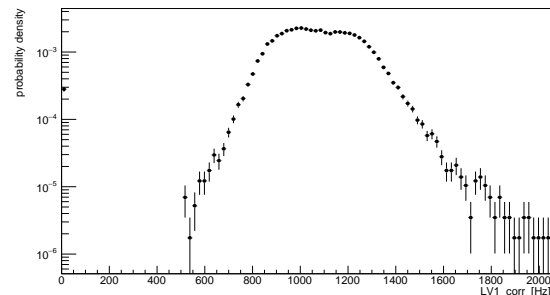
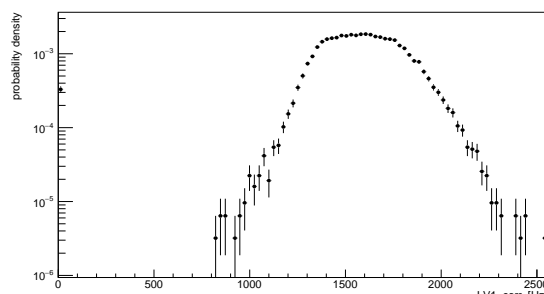
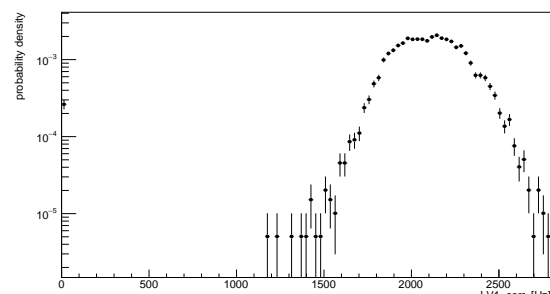


Figure A.5: distributions of AMS-02 trigger rate FTE (corrected by the live-time) for different L -values during January, 2020.

(a) $L \in [0.5, 1.0] R_{\text{Earth}}$ (b) $L \in [1.0, 1.5] R_{\text{Earth}}$ (c) $L \in [1.5, 2.0] R_{\text{Earth}}$ (d) $L \in [2.0, 2.5] R_{\text{Earth}}$ (e) $L \in [2.5, 3.0] R_{\text{Earth}}$ (f) $L \in [3.0, 3.5] R_{\text{Earth}}$

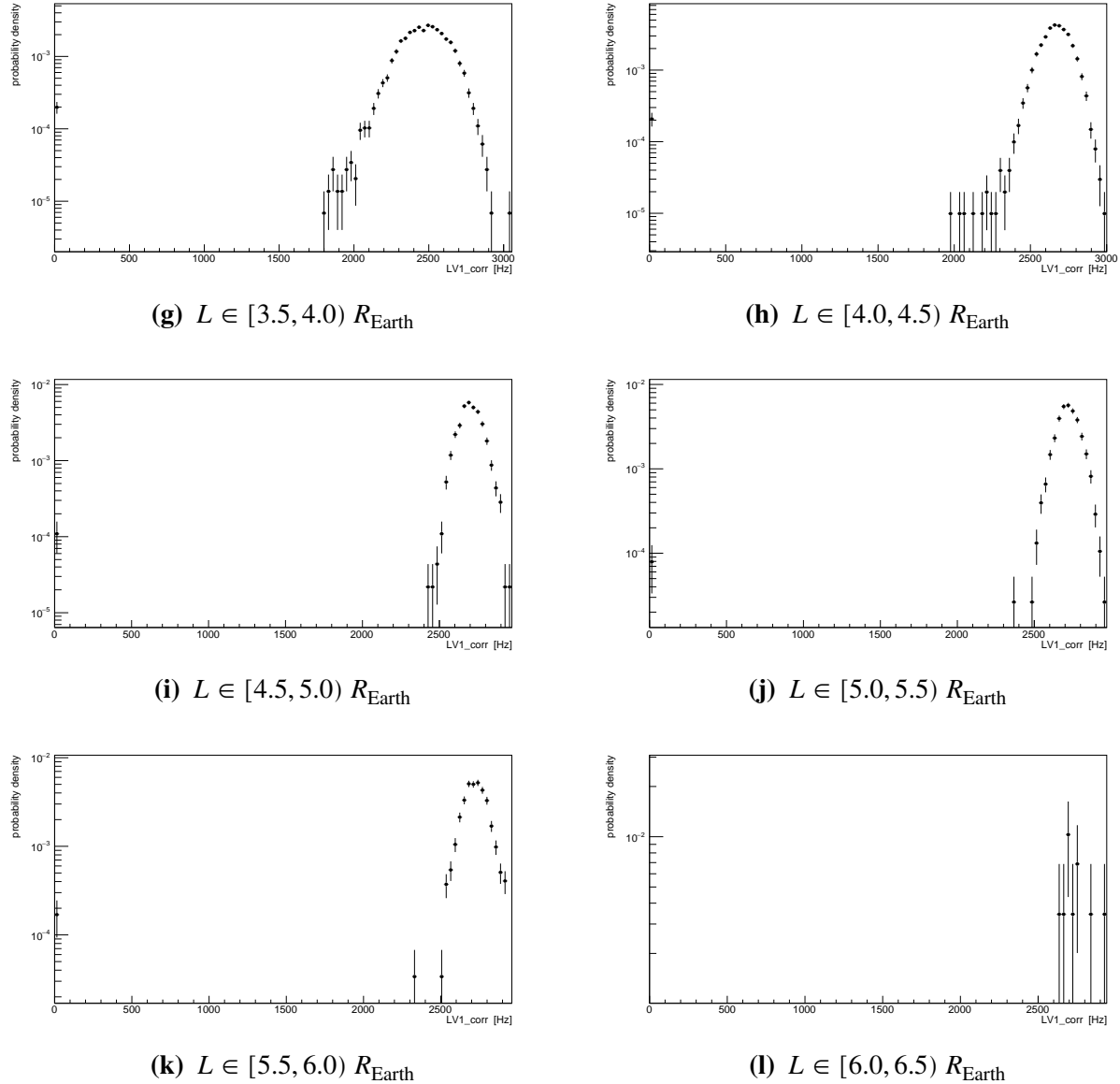
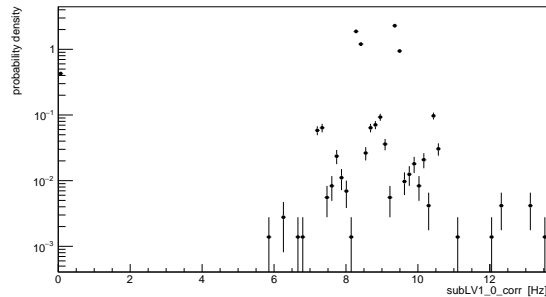
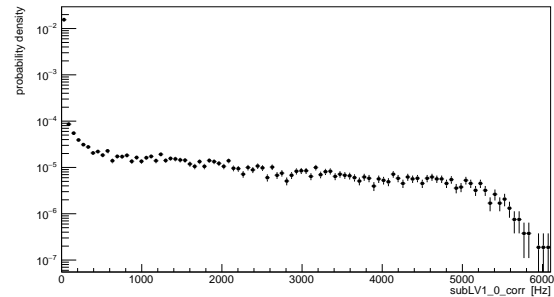
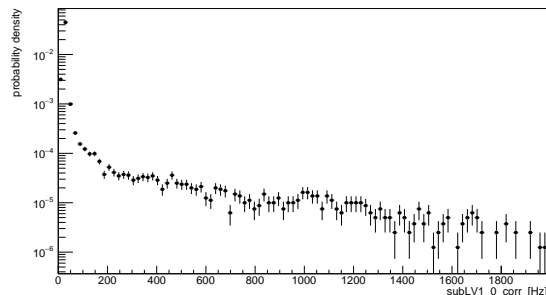
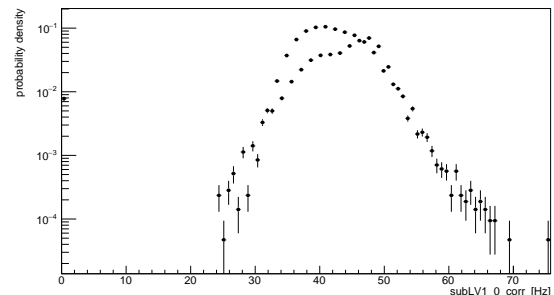
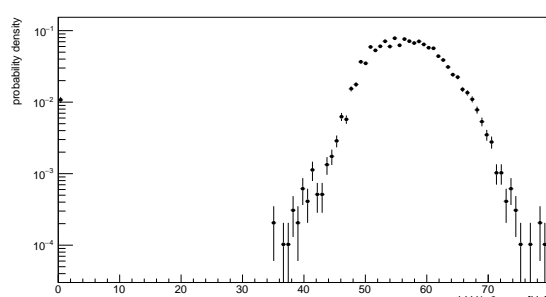
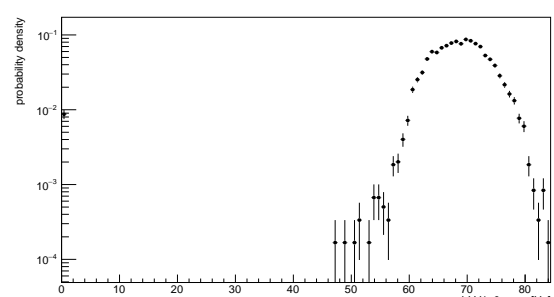


Figure A.6: distributions of AMS-02 trigger rate LV1 (corrected by the live-time) for different L -values during January, 2020.

(a) $L \in [0.5, 1.0] R_{\text{Earth}}$ (b) $L \in [1.0, 1.5] R_{\text{Earth}}$ (c) $L \in [1.5, 2.0] R_{\text{Earth}}$ (d) $L \in [2.0, 2.5] R_{\text{Earth}}$ (e) $L \in [2.5, 3.0] R_{\text{Earth}}$ (f) $L \in [3.0, 3.5] R_{\text{Earth}}$

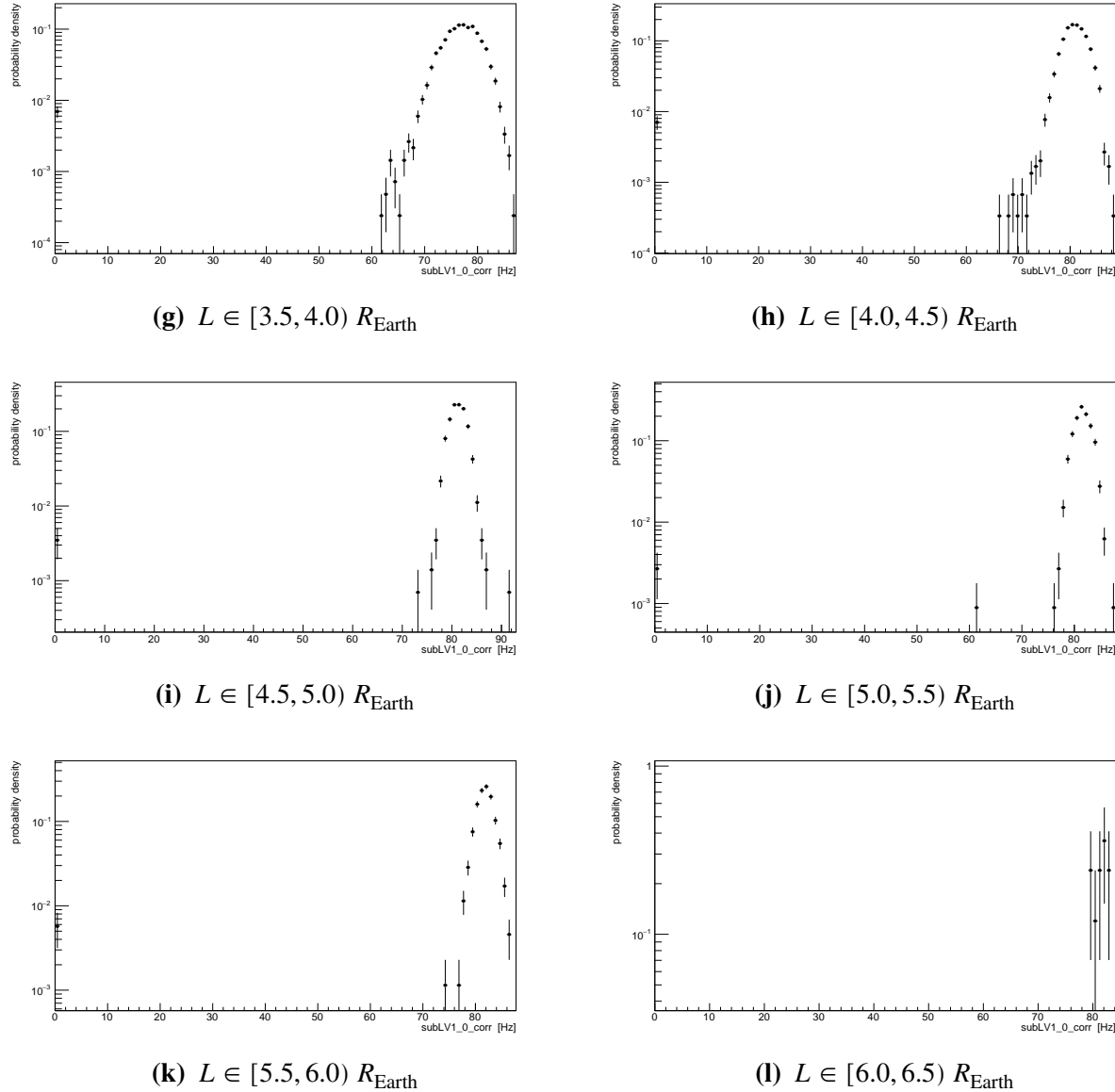
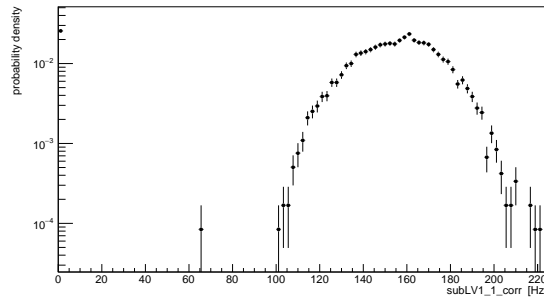
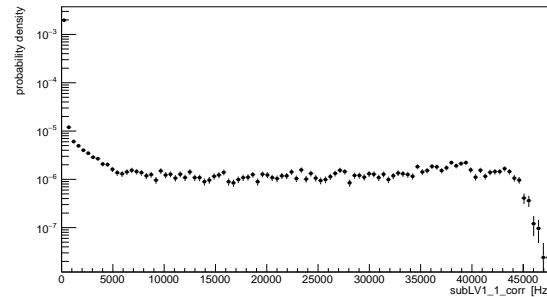
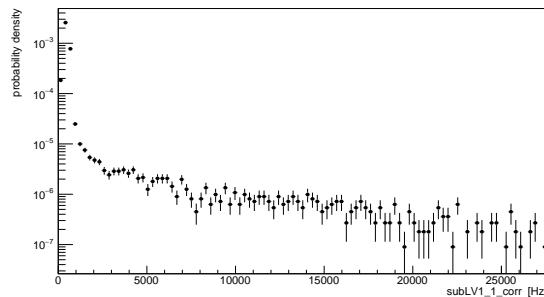
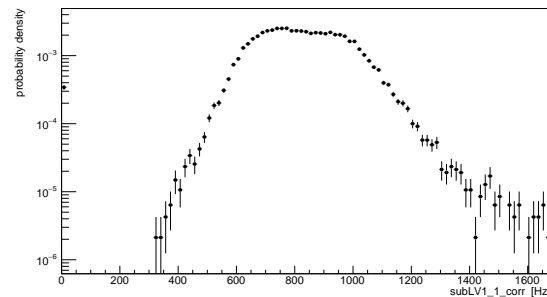
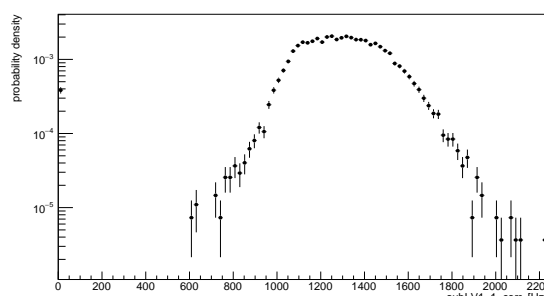
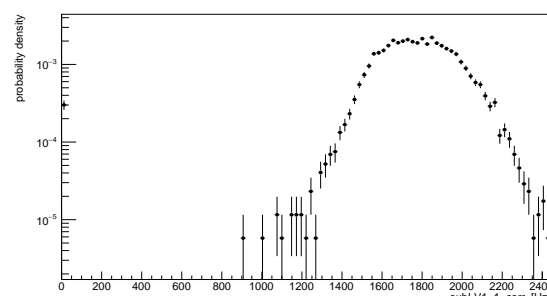


Figure A.7: distributions of AMS-02 trigger rate subLV1_0 (corrected by the live-time) for different L -values during January, 2020.

(a) $L \in [0.5, 1.0] R_{\text{Earth}}$ (b) $L \in [1.0, 1.5] R_{\text{Earth}}$ (c) $L \in [1.5, 2.0] R_{\text{Earth}}$ (d) $L \in [2.0, 2.5] R_{\text{Earth}}$ (e) $L \in [2.5, 3.0] R_{\text{Earth}}$ (f) $L \in [3.0, 3.5] R_{\text{Earth}}$

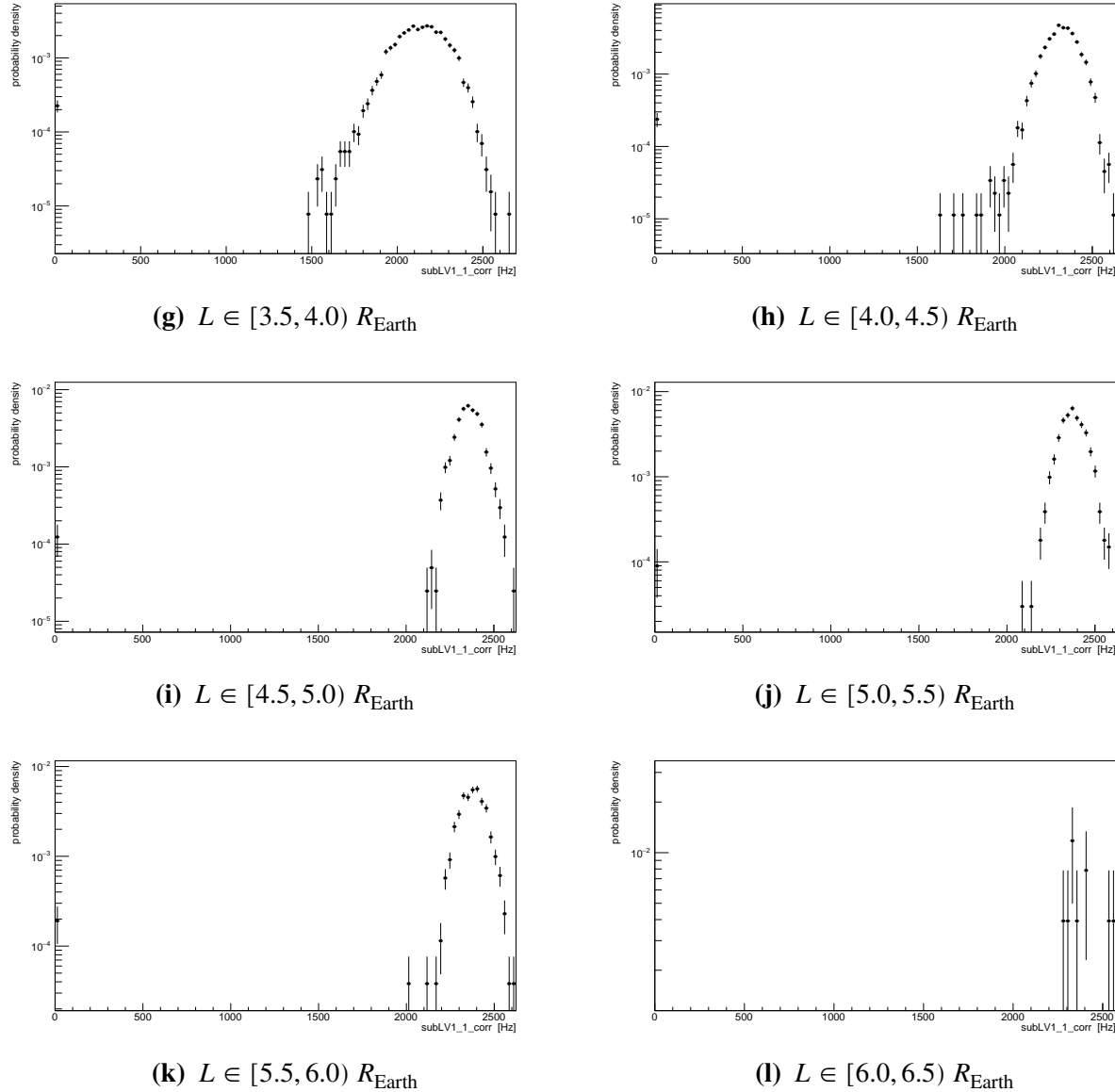
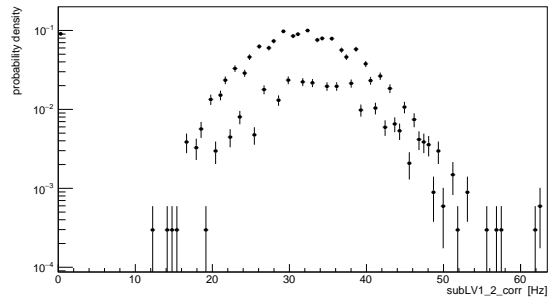
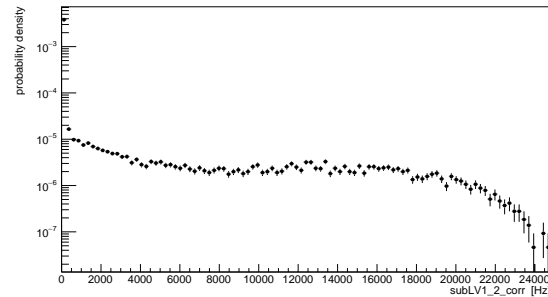
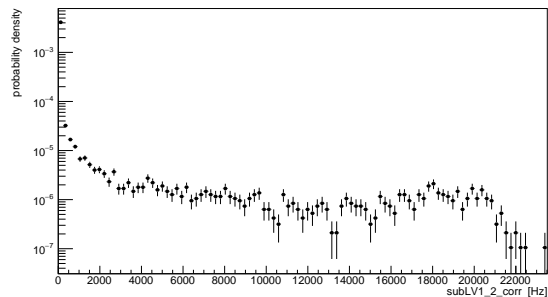
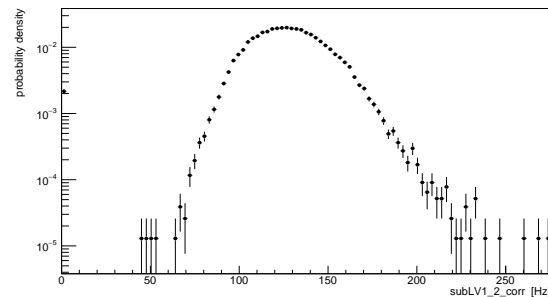
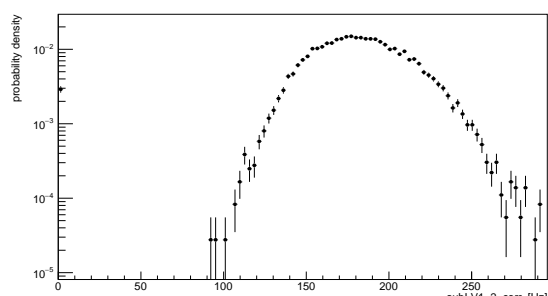
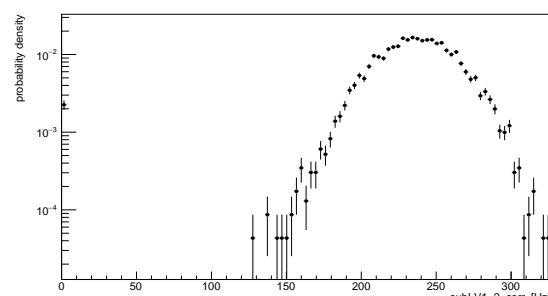


Figure A.8: distributions of AMS-02 trigger rate subLV1_1 (corrected by the live-time) for different L -values during January, 2020.

(a) $L \in [0.5, 1.0] R_{\text{Earth}}$ (b) $L \in [1.0, 1.5] R_{\text{Earth}}$ (c) $L \in [1.5, 2.0] R_{\text{Earth}}$ (d) $L \in [2.0, 2.5] R_{\text{Earth}}$ (e) $L \in [2.5, 3.0] R_{\text{Earth}}$ (f) $L \in [3.0, 3.5] R_{\text{Earth}}$

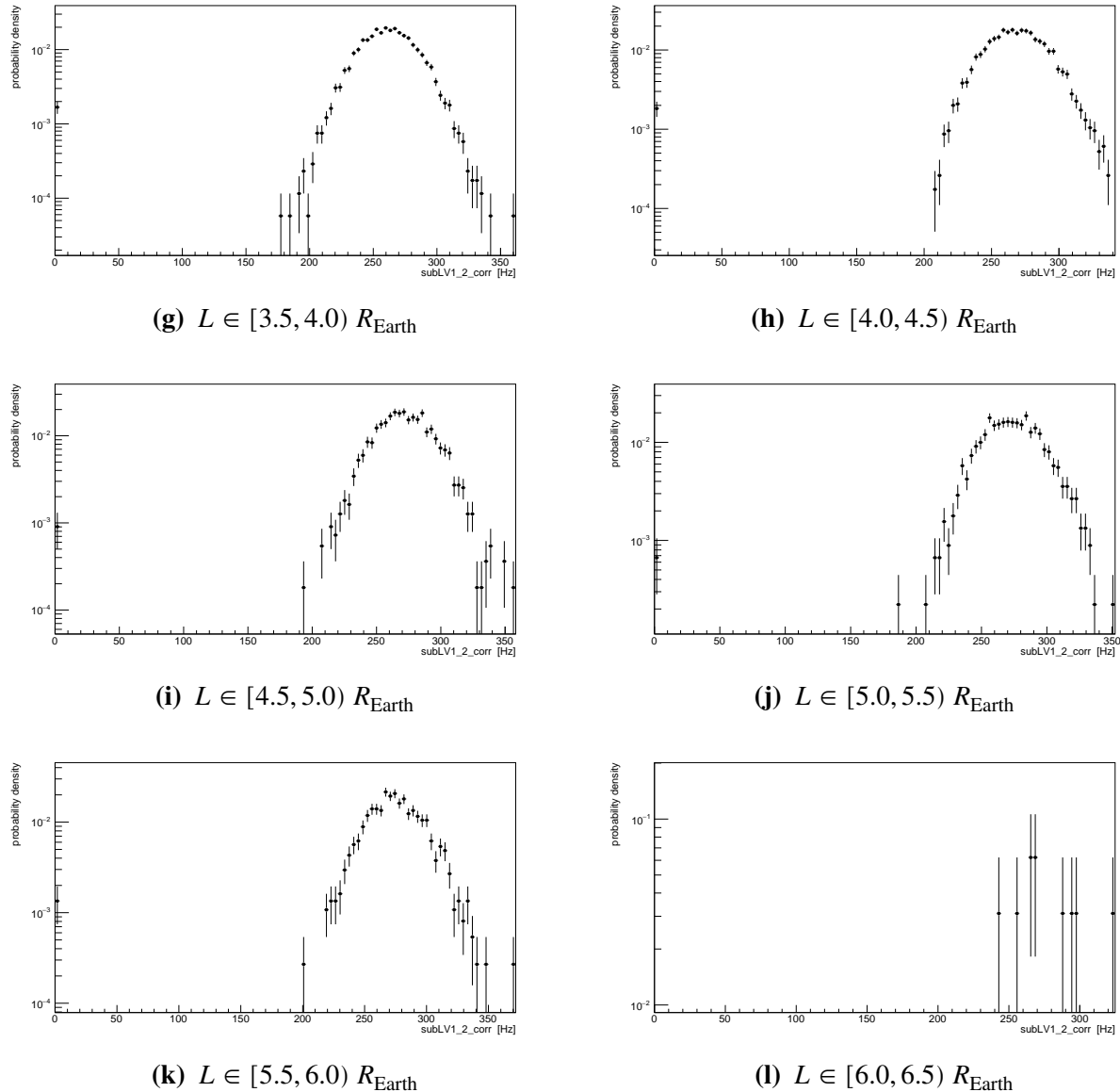
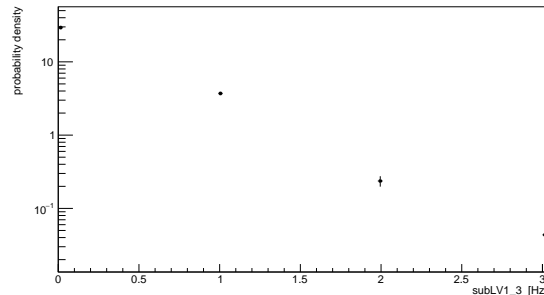
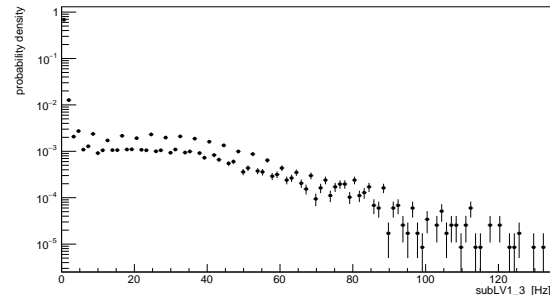
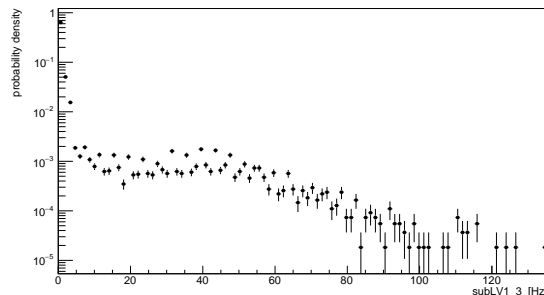
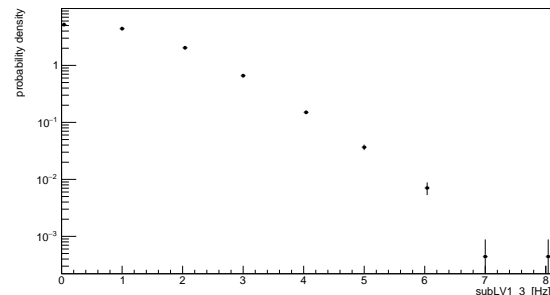
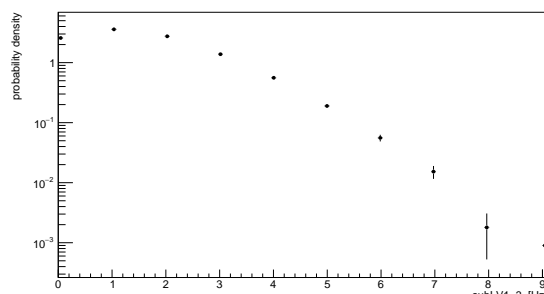
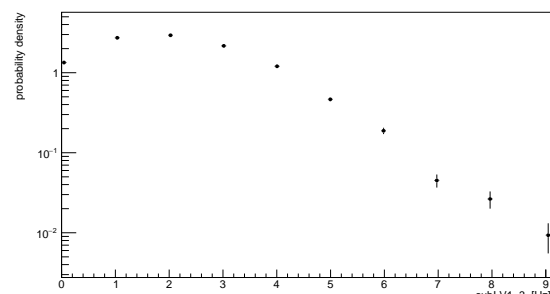


Figure A.9: distributions of AMS-02 trigger rate subLV1_2 (corrected by the live-time) for different L -values during January, 2020.

(a) $L \in [0.5, 1.0] R_{\text{Earth}}$ (b) $L \in [1.0, 1.5] R_{\text{Earth}}$ (c) $L \in [1.5, 2.0] R_{\text{Earth}}$ (d) $L \in [2.0, 2.5] R_{\text{Earth}}$ (e) $L \in [2.5, 3.0] R_{\text{Earth}}$ (f) $L \in [3.0, 3.5] R_{\text{Earth}}$

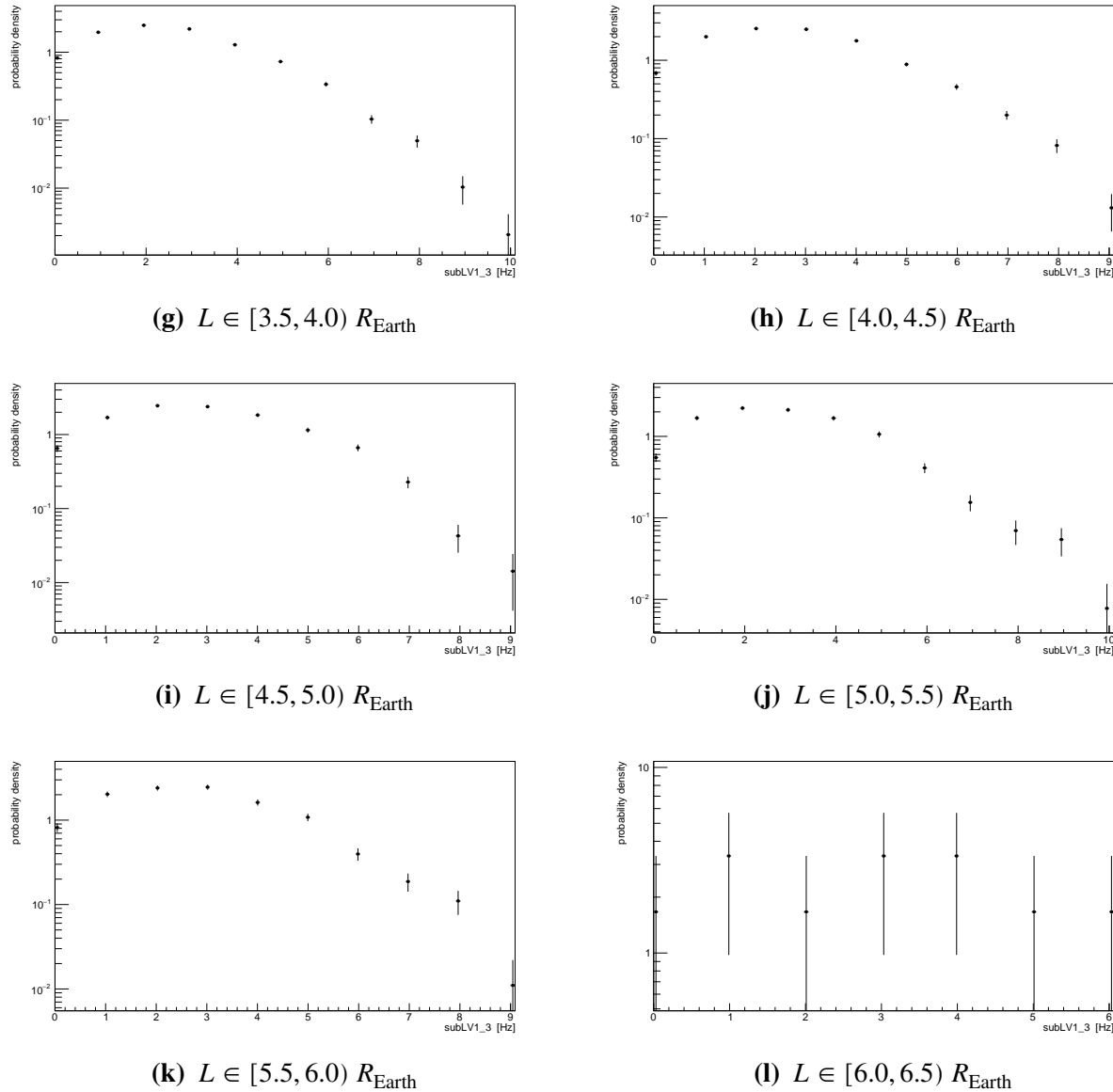
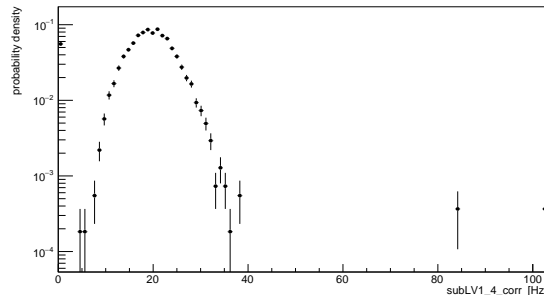
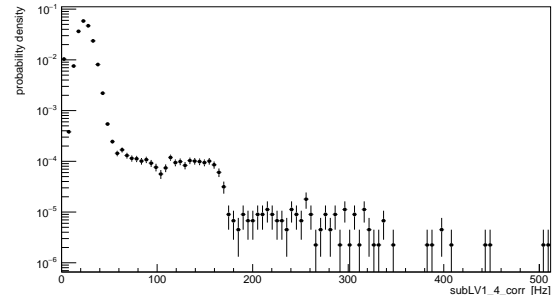
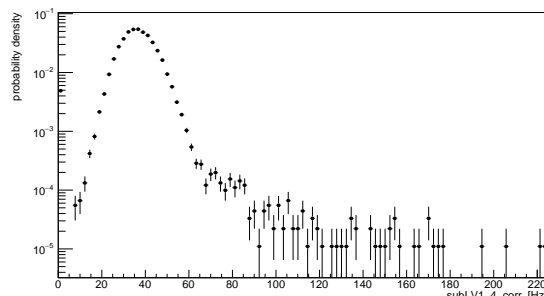
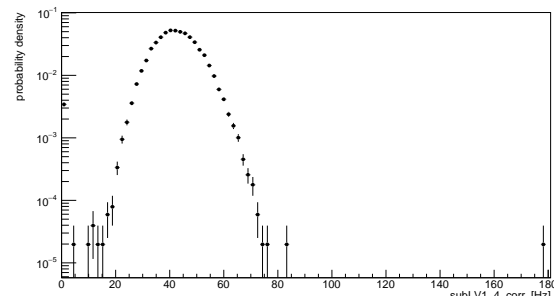
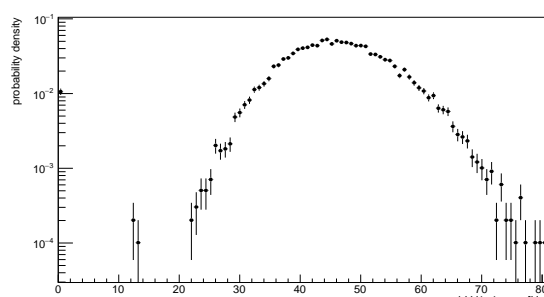
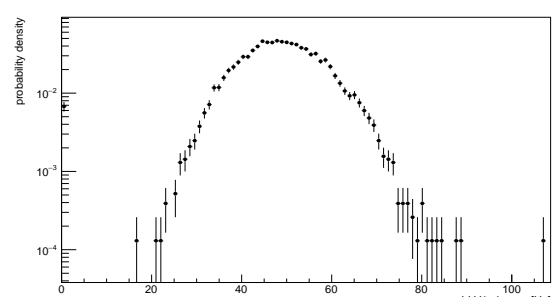


Figure A.10: distributions of AMS-02 trigger rate subLV1_3 (raw) for different L -values during January, 2020.

(a) $L \in [0.5, 1.0] R_{\text{Earth}}$ (b) $L \in [1.0, 1.5] R_{\text{Earth}}$ (c) $L \in [1.5, 2.0] R_{\text{Earth}}$ (d) $L \in [2.0, 2.5] R_{\text{Earth}}$ (e) $L \in [2.5, 3.0] R_{\text{Earth}}$ (f) $L \in [3.0, 3.5] R_{\text{Earth}}$

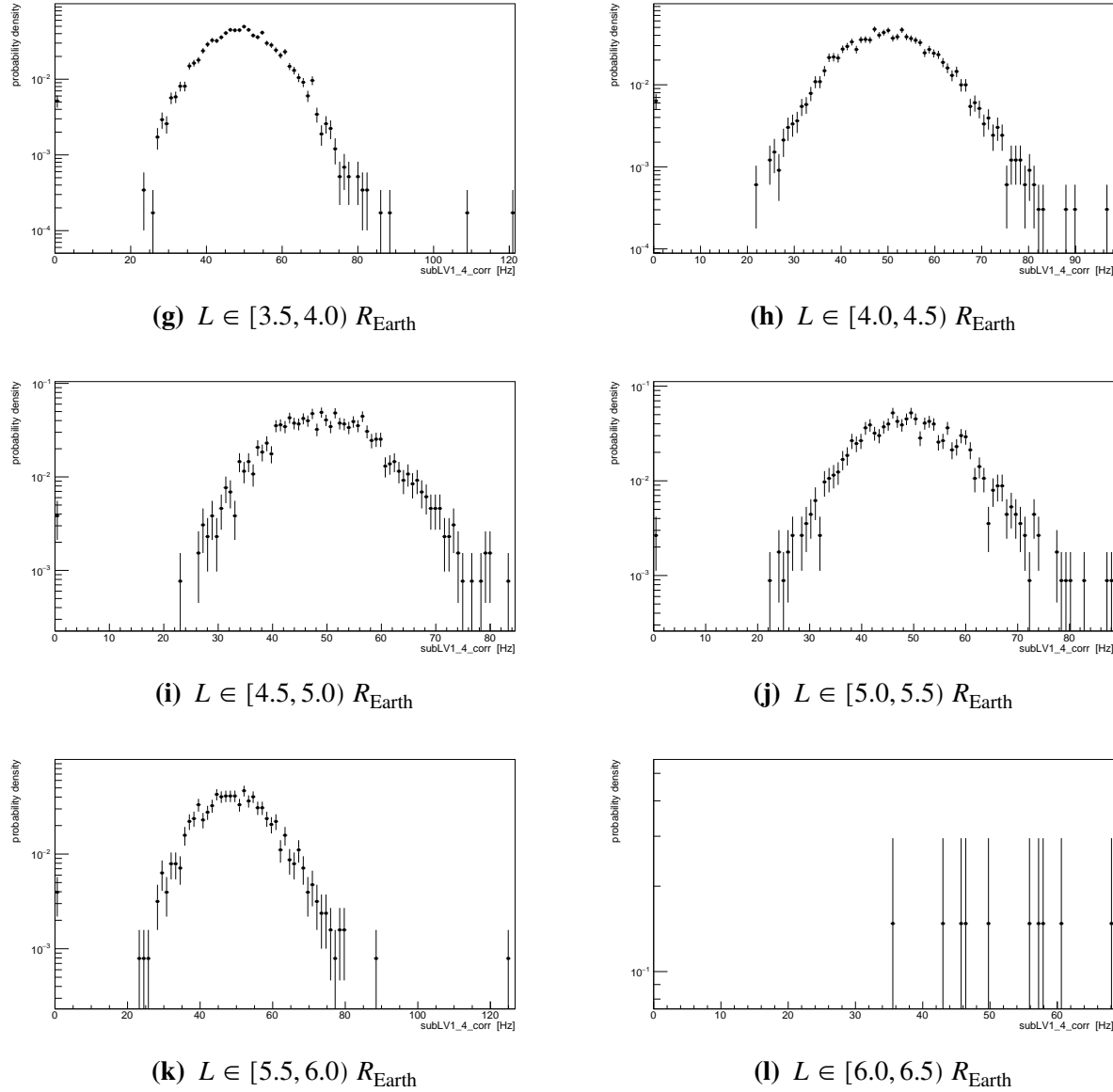
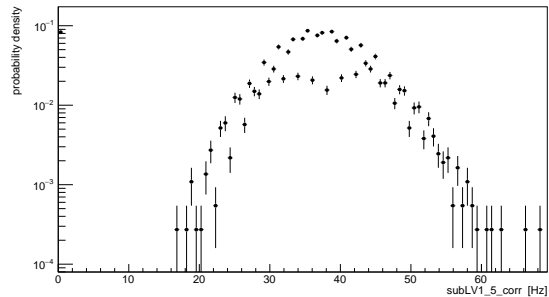
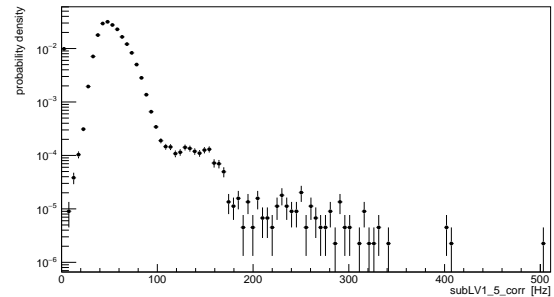
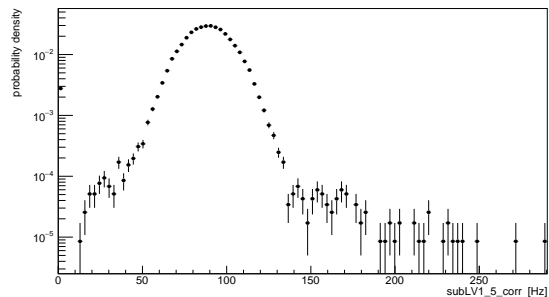
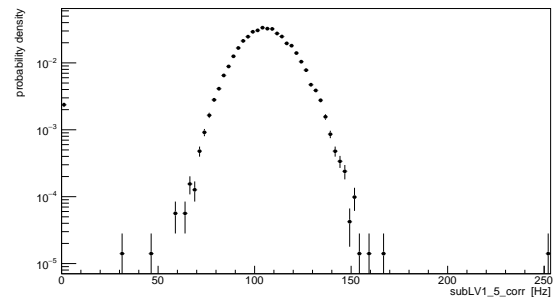
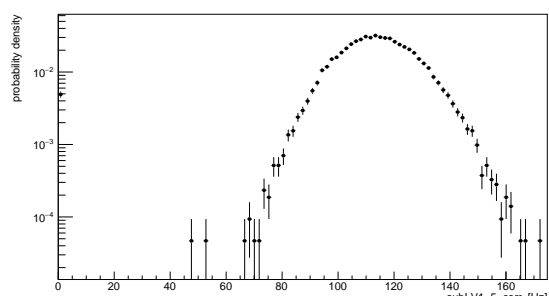
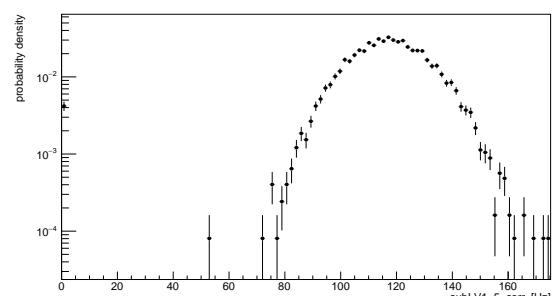


Figure A.11: distributions of AMS-02 trigger rate subLV1_4 (corrected by the live-time) for different L -values during January, 2020.

(a) $L \in [0.5, 1.0] R_{\text{Earth}}$ (b) $L \in [1.0, 1.5] R_{\text{Earth}}$ (c) $L \in [1.5, 2.0] R_{\text{Earth}}$ (d) $L \in [2.0, 2.5] R_{\text{Earth}}$ (e) $L \in [2.5, 3.0] R_{\text{Earth}}$ (f) $L \in [3.0, 3.5] R_{\text{Earth}}$

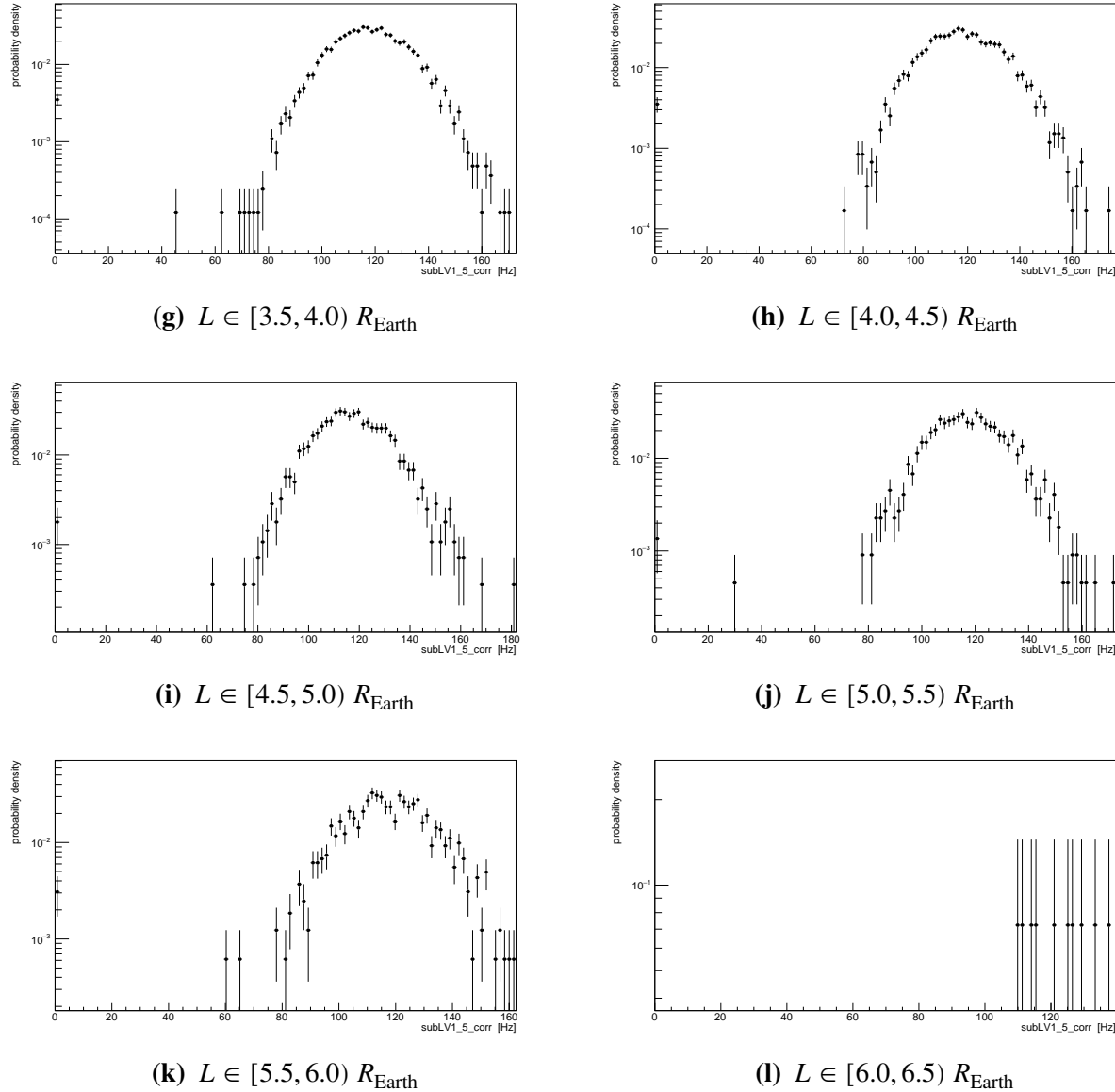


Figure A.12: distributions of AMS-02 trigger rate subLV1_5 (corrected by the live-time) for different L -values during January, 2020.

Appendix B

Solar Proton Events

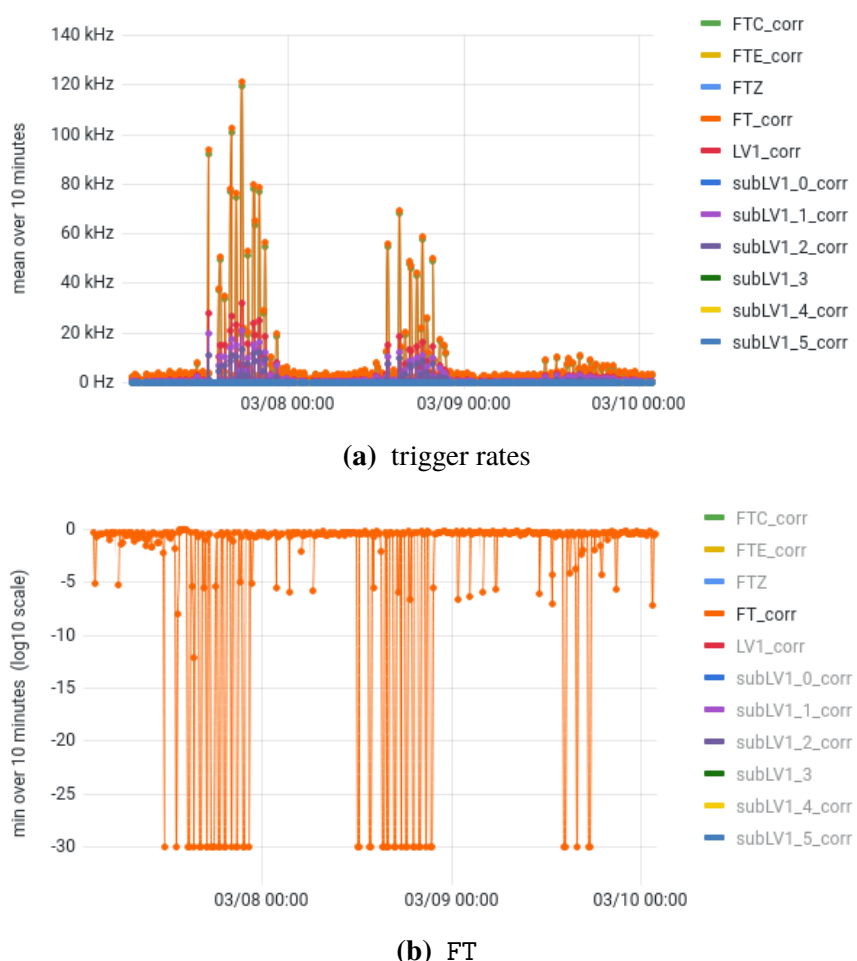
Event start (Day/UTC)	Event maximum (Day/UTC)	Proton flux (cm⁻² s⁻¹ sr⁻¹)
2011		
Mar 08/0105	Mar 08/0800	50
Mar 21/1950	Mar 22/0135	14
Jun 07/0820	Jun 07/1820	72
Aug 04/0635	Aug 05/2150	96
Aug 09/0845	Aug 09/1210	26
Sep 23/2255	Sep 26/1155	35
Nov 26/1125	Nov 27/0125	80
2012		
Jan 23/0530	Jan 24/1530	6310
Jan 27/1905	Jan 28/0205	796
Mar 07/0510	Mar 08/1115	6530
Mar 13/1810	Mar 13/2045	469
May 17/0210	May 17/0430	255
May 27/0535	May 27/1045	14
Jun 16/1955	Jun 16/2020	14
Jul 07/0400	Jul 07/0745	25
Jul 12/1835	Jul 12/2225	96
Jul 17/1715	Jul 18/0600	136
Jul 23/1545	Jul 23/2145	12
Sep 01/1335	Sep 02/0859	59
Sep 28/0300	Sep 28/0445	28

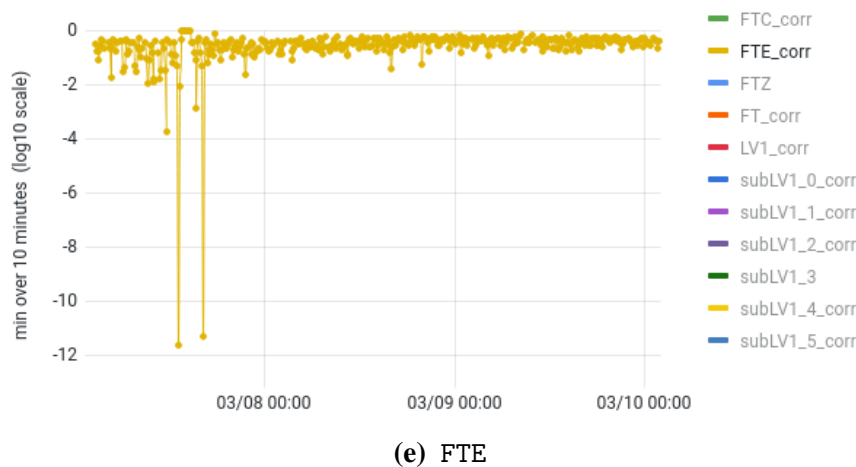
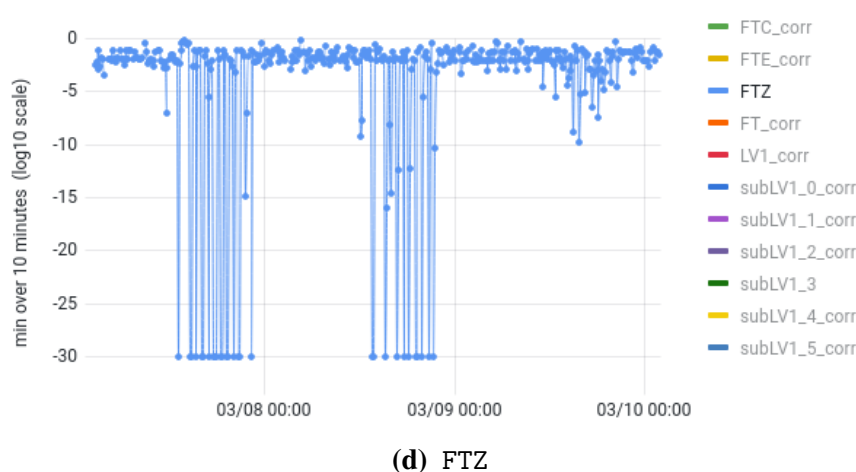
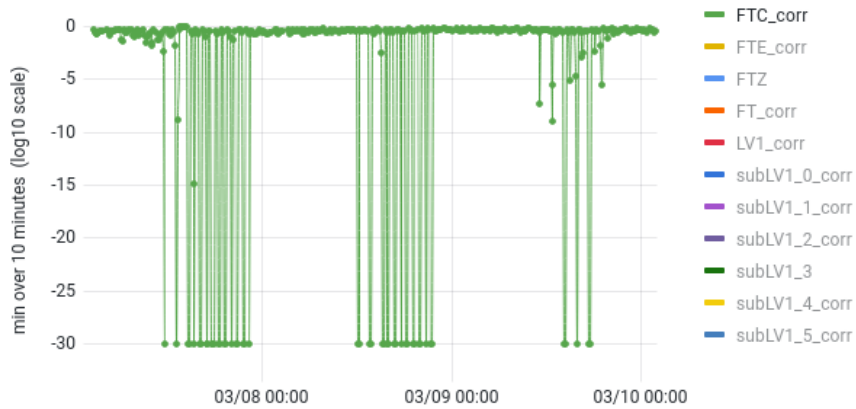
Event start (Day/UTC)	Event maximum (Day/UTC)	Proton flux (cm⁻² s⁻¹ sr⁻¹)
2013		
Mar 16/1940	Mar 17/0700	16
Apr 11/1055	Apr 11/1645	114
May 14/1325	May 17/1720	41
May 22/1420	May 23/0650	1660
Jun 23/2014	Jun 24/0520	14
Sep 30/0505	Sep 30/2005	182
Dec 28/2150	Dec 28/2315	29
2014		
Jan 06/0915	Jan 06/1600	42
Jan 06/0915	Jan 09/0340	1033
Feb 20/0850	Feb 20/0925	22
Feb 25/1355	Feb 28/0845	103
2015		
Jun 18/1135	Jun 18/1445	16
Oct 29/0550	Oct 29/1000	23
2016		
Jan 02/0430	Jan 02/0450	21
2017		
Sep 05/0751	Sep 05/1930	210
2021		
May 29/0300	May 29/0320	15
Oct 30/2100	Oct 30/2105	11
2022		
Jan 20/0800	Jan 20/1015	22
Mar 28/1325	Mar 28/1450	19
Mar 31/0620	Mar 31/0630	11
Apr 02/1430	Apr 02/1600	32

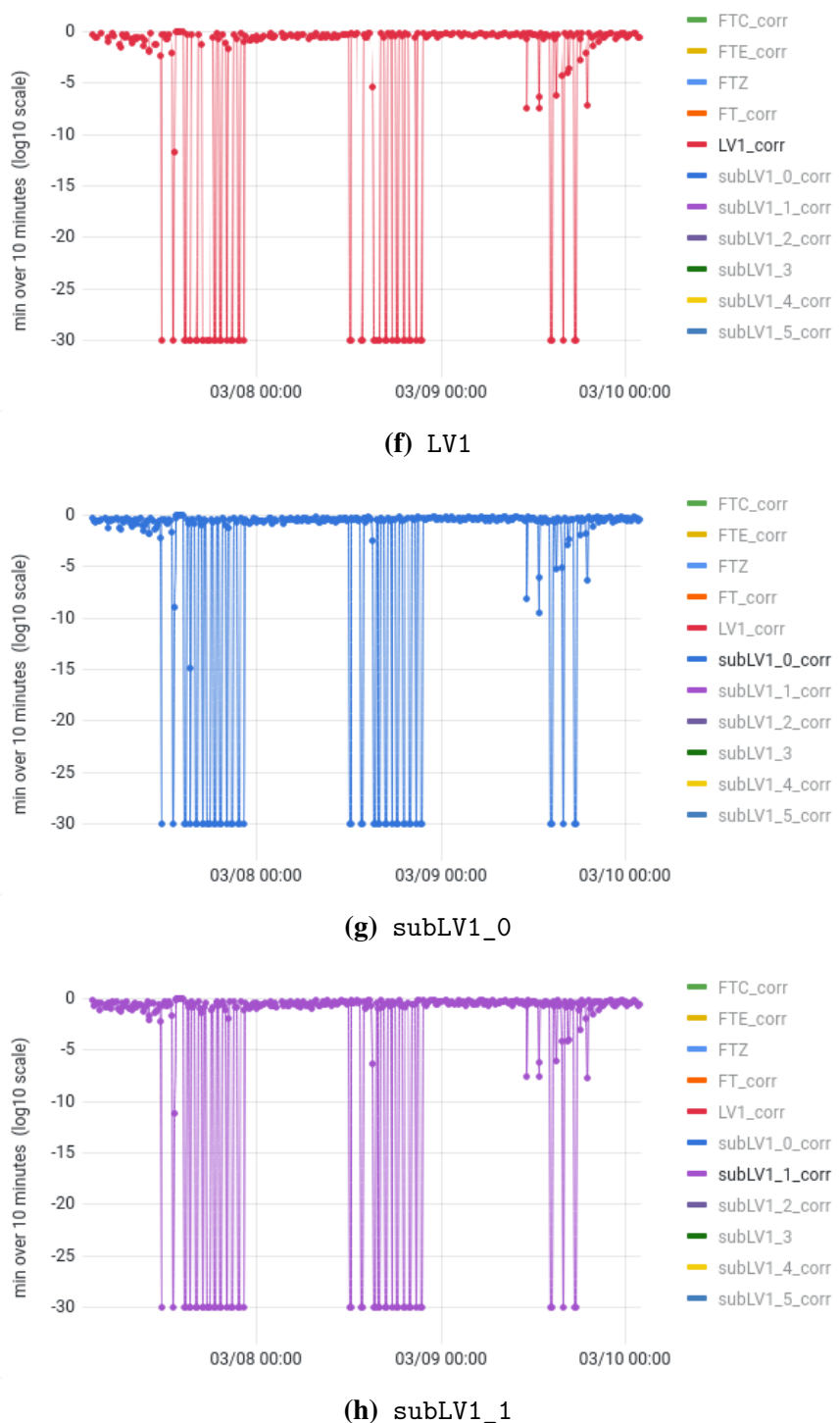
Table B.1: Solar Proton Eventss (SPEs) affecting the Earth environment between 2011 and 2022 [136]. Proton fluxes are given as 5-minutes averages for energies > 10 MeV, measured by Geostationary Operational Environmental Satellite (GOES) spacecraft at Geosynchronous orbit. The Space Weather Prediction Center (SWPC) defines the start of a proton event to be the first of 3 consecutive data points with fluxes ≥ 10 particles cm⁻² s⁻¹ sr⁻¹ and its end the last time the flux was greater than the threshold. Flare and CMEs associations are given from SOHO.

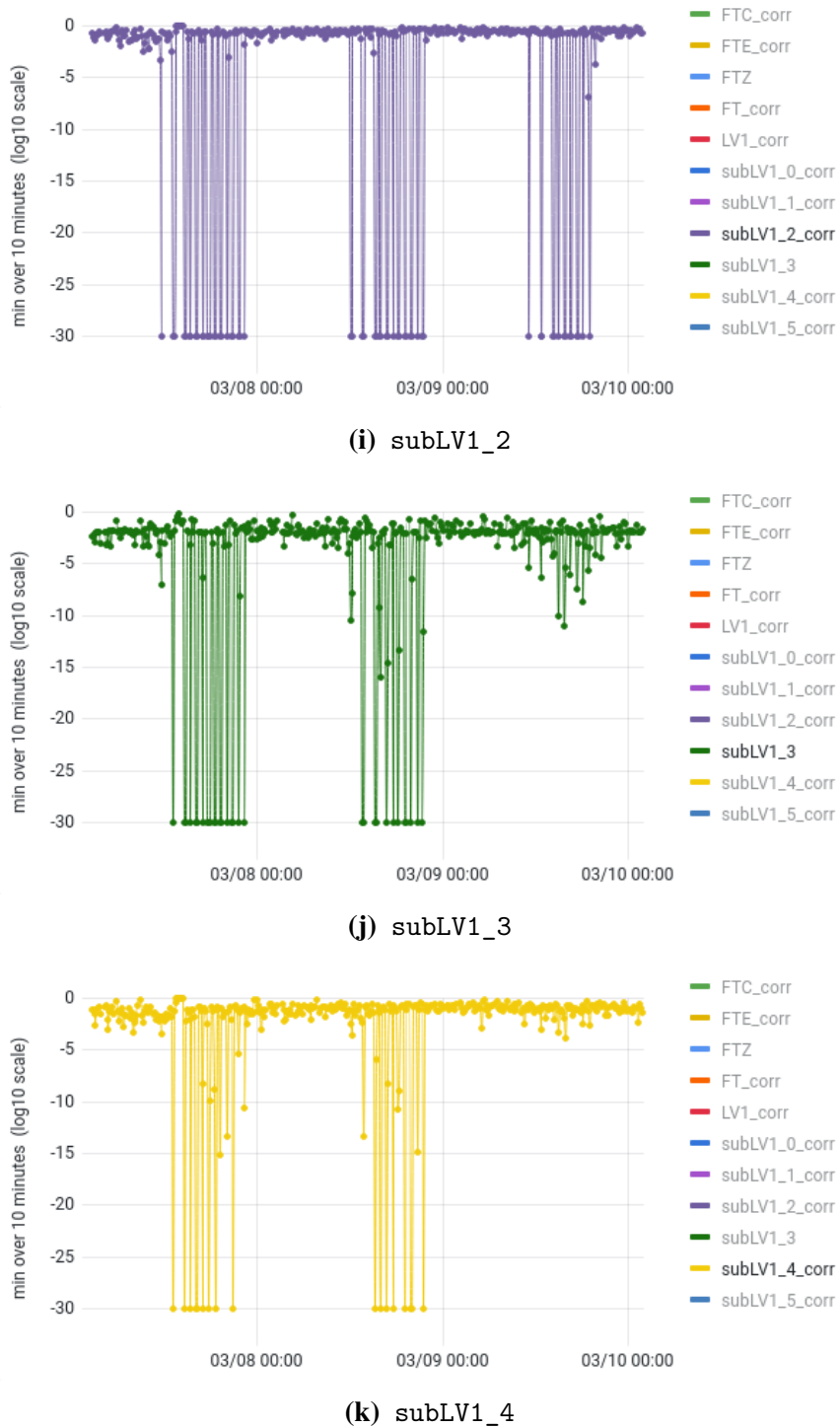
Appendix C

Time-series from the real-time monitor









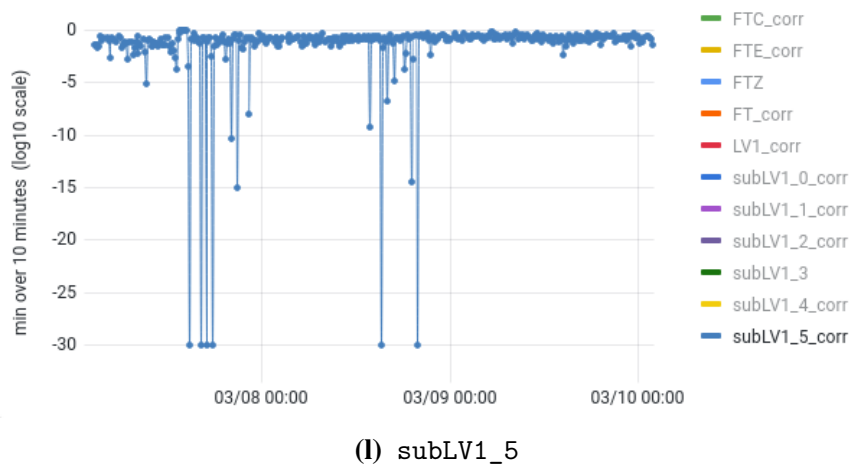
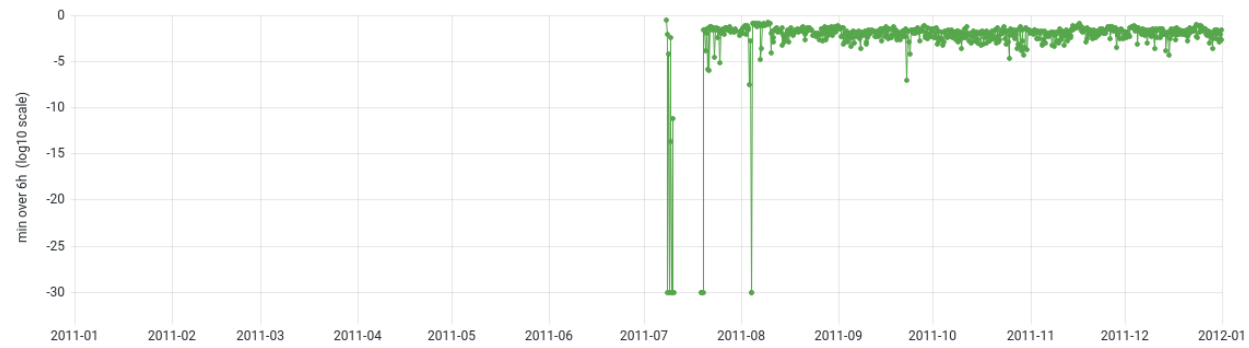


Figure C.1: SEP event of March 7–8, 2012 (ref. to tab. B.1) [135]. Sub-figures show the rates and the tilde scores processed by the system described in chapter 5. The rate plot shows three excesses left by the SEPs; the event does not generate just one continuous peak because of the changing in the L -value of the data taking area and the rigidity of the SEPs. Score plots show which triggers present excesses traceable to the event. In particular FTE is completely inaccurate while the smallest excess of the series, i.e. the last one, is missing in triggers subLV1_3, subLV1_4, subLV1_5 and reduced in FTZ. Rate plot uses mean values over 10 minutes time intervals, while score plots reports minimum values over the same time intervals with a logarithmic scale. In score plots, null values, due to very large deviations from the nominal level, are replaced by 10^{-30} .



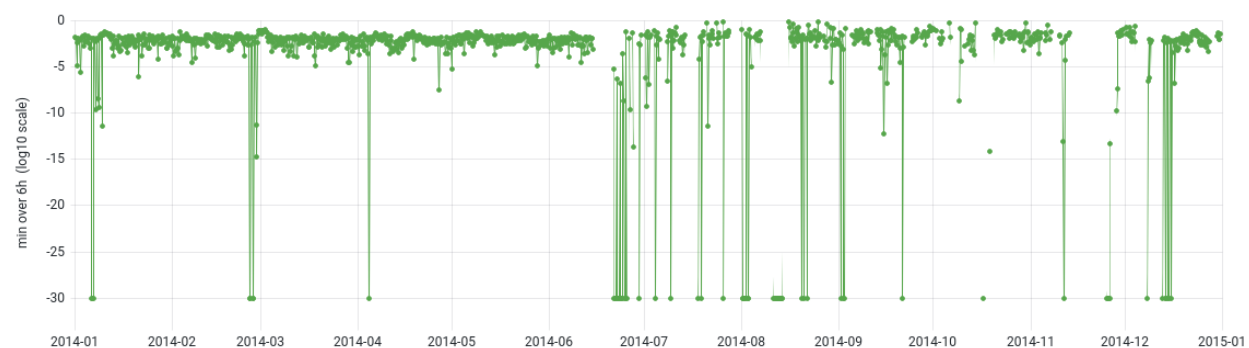
(a) 2011



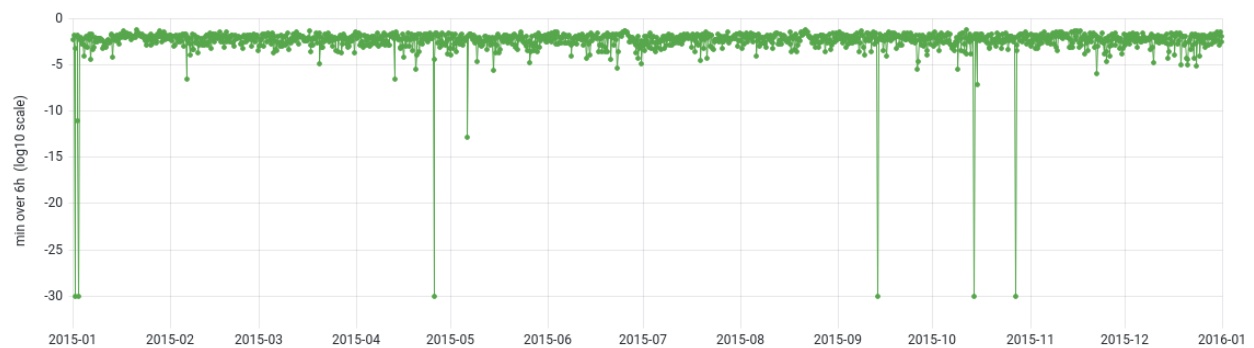
(b) 2012



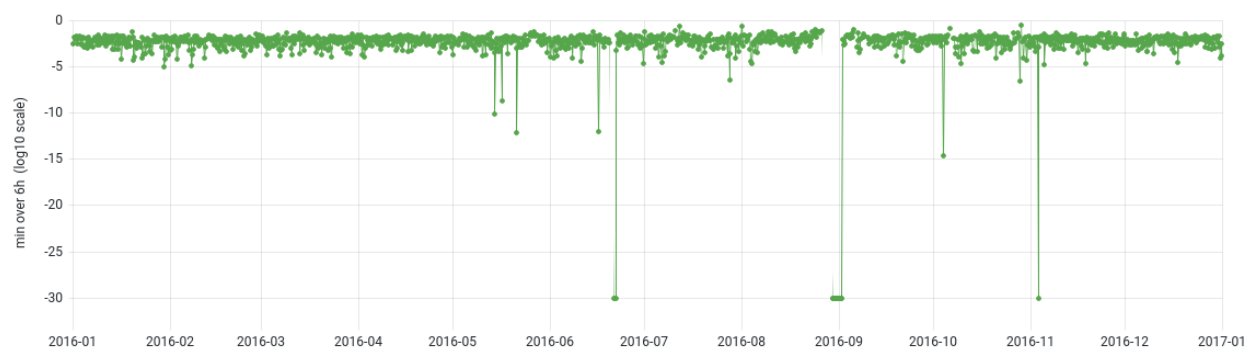
(c) 2013



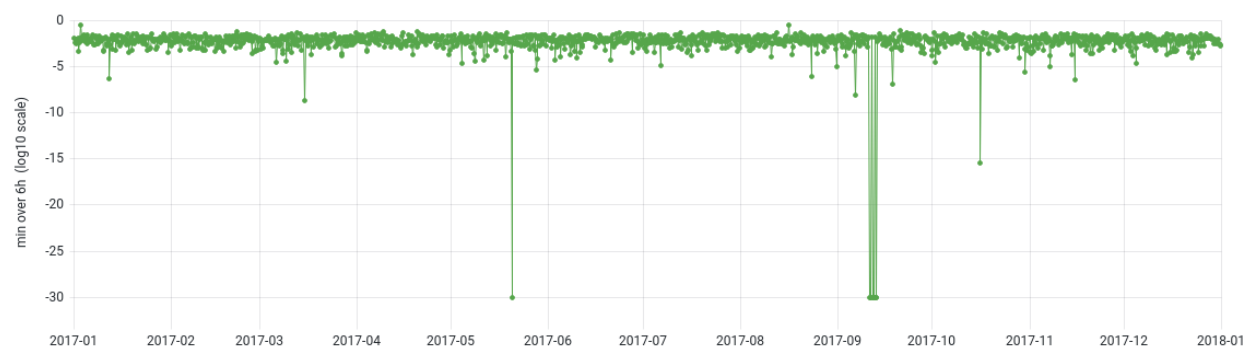
(d) 2014



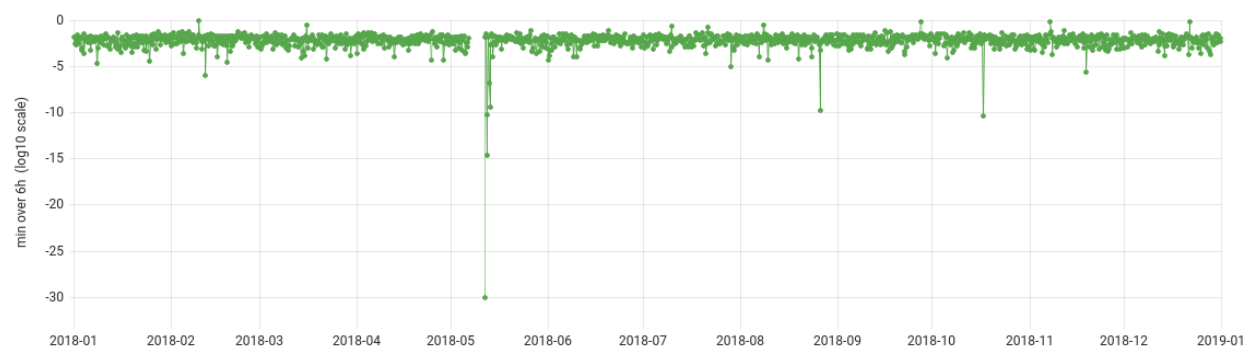
(e) 2015



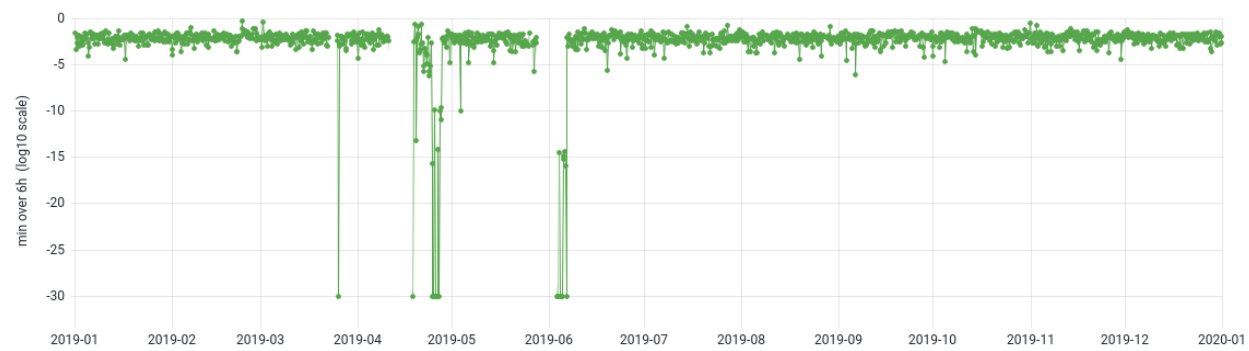
(f) 2016



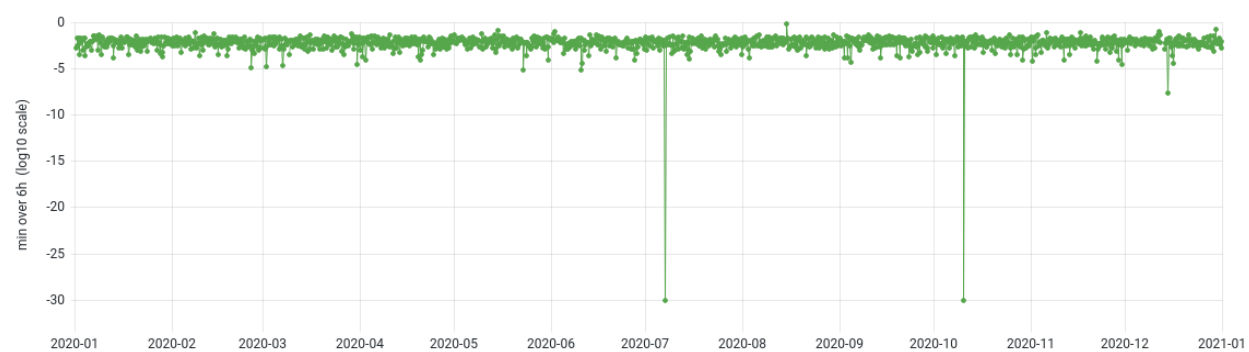
(g) 2017



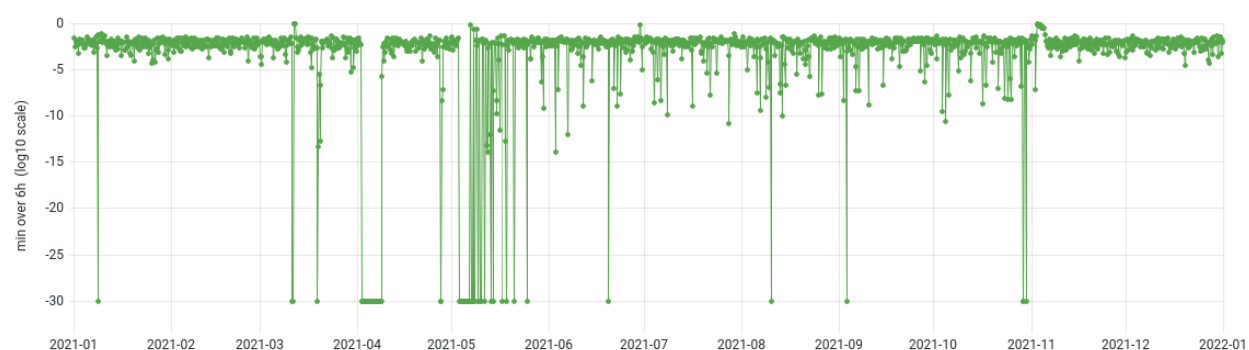
(h) 2018



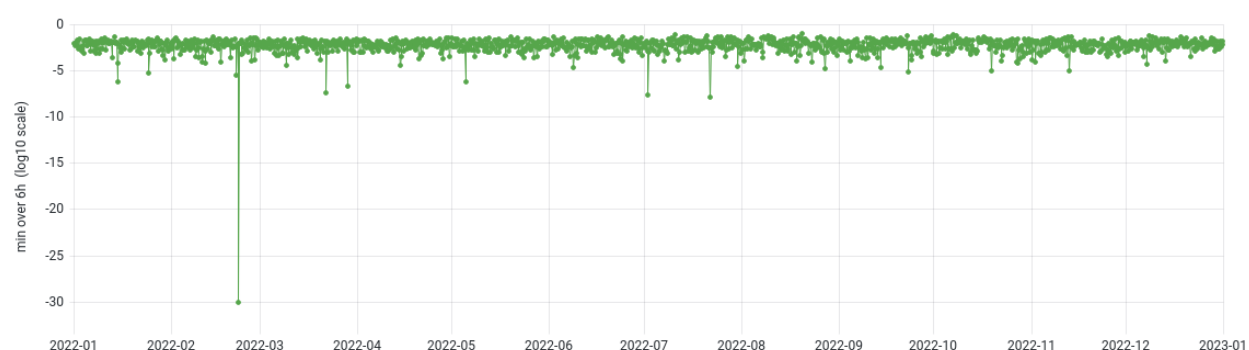
(i) 2019



(j) 2020



(k) 2021



(l) 2022

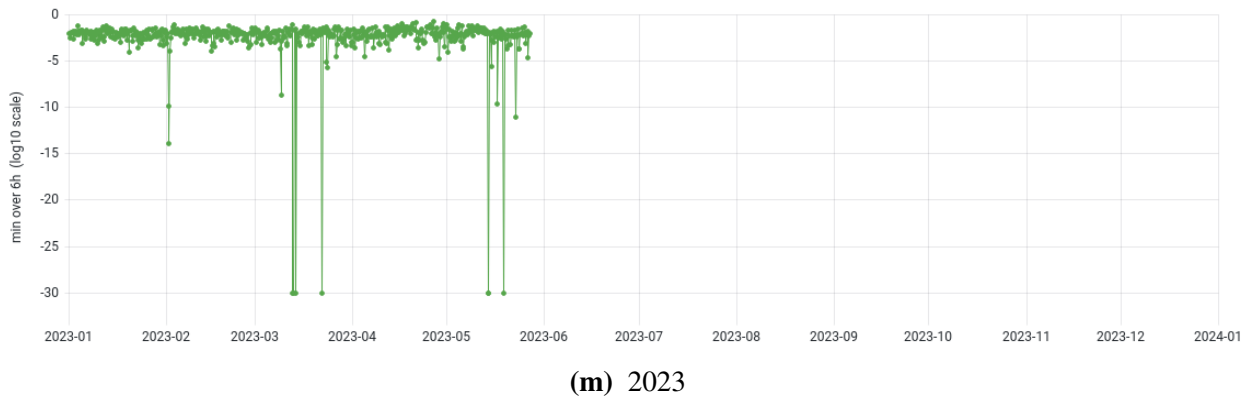


Figure C.2: complete time-series of regular score of LV1 trigger [135]. Sub-figures show minimums over 6 hours time-intervals for 1 year of data. In the plots, null scores are replaced by 10^{-30} , to show them on a logarithmic scale. An additional cut $L < 6 R_{\text{Earth}}$ is applied beyond the standard ones for background subtraction (ref. to sect. 5.3); the bin $[6.0, 6.5] R_{\text{Earth}}$ is characterized by a low number of entries for the reference distributions that define the quiet level (~ 10 entries per month), therefore it generates apparent excesses in the regular score time-series. Low scores not always correspond to a SEP event, showing the need of more exclusion conditions for SEPs identification.

Bibliography

- [1] *Programmi di ricerca per le borse di studio per i laureandi o neo laureati magistrali in Fisica e Ingegneria. Progetto formativo "La Fisica Astroparticellare nei Laboratori"*. Content viewed on May 27, 2023. Mar. 2022. URL: <https://web.infn.it/csn2/index.php/it/eventi-2/borse-laureandi-neo-laureati/2-uncategorised/171-elenco-programmi-borse-2022>.
- [2] Malcolm S. Longair. “The origin of cosmic rays in our Galaxy”. In: *High Energy Astrophysics*. 2011. Chap. 16.
- [3] E. Fermi. “On the Origin of the Cosmic Radiation”. In: *Phys. Rev.* 75 (8 Apr. 1949), pp. 1169–1174. doi: 10.1103/PhysRev.75.1169.
- [4] Andrew W. Strong, Igor V. Moskalenko, and Vladimir S. Ptuskin. “Cosmic-Ray Propagation and Interactions in the Galaxy”. In: *Annual Review of Nuclear and Particle Science* 57.1 (2007), pp. 285–327. doi: 10.1146/annurev.nucl.57.090506.123011.
- [5] E.N. Parker. “The passage of energetic charged particles through interplanetary space”. In: *Planetary and Space Science* 13.1 (1965), pp. 9–49. doi: 10.1016/0032-0633(65)90131-5.
- [6] N. E. Raouafi et al. “Solar Coronal Jets: Observations, Theory, and Modeling”. In: *Space Science Reviews* 201 (1 Nov. 2016), pp. 1–53. doi: 10.1007/s11214-016-0260-5.
- [7] S. W. Kahler et al. “Associations between coronal mass ejections and solar energetic proton events”. In: *Journal of Geophysical Research: Space Physics* 89.A11 (1984), pp. 9683–9693. doi: 10.1029/JA089iA11p09683.
- [8] F. Faldi et al. “Real-time monitoring of solar energetic particles outside the ISS with the AMS-02 instrument”. In: *Rendiconti Lincei. Scienze Fisiche e Naturali* (Apr. 2023). doi: 10.1007/s12210-023-01156-2.
- [9] N. Bucciantini. *Raggi cosmici, particelle dallo spazio profondo*. Content viewed on Feb. 15, 2023. 2017. URL: <https://www.media.inaf.it/2017/07/25/raggi-cosmici/>.
- [10] Karl-Heinz Kampert. “Cosmic Rays from the Knee to the Ankle - Status and Prospects”. In: *Nuclear Physics B - Proceedings Supplements* 165 (2007), pp. 294–306. doi: 10.1016/j.nuclphysbps.2006.11.048.
- [11] Veniamin Berezhinsky, Askhat Gazizov, and Svetlana Grigorieva. “On astrophysical solution to ultrahigh energy cosmic rays”. In: *Physical Review D* 74.4 (Aug. 2006). doi: 10.1103/physrevd.74.043005.
- [12] Kenneth Greisen. “End to the Cosmic-Ray Spectrum?” In: *Phys. Rev. Lett.* 16 (17 Apr. 1966), pp. 748–750. doi: 10.1103/PhysRevLett.16.748.
- [13] K.L. Klein and S. Dalla. “Acceleration and Propagation of Solar Energetic Particles”. In: *Space Science Reviews* 212 (2017), pp. 1107–1136. doi: 10.1007/s11214-017-0382-4.

- [14] S. Manconi, M. Di Mauro, and F. Donato. “Dipole anisotropy in cosmic electrons and positrons: inspection on local sources”. In: *Journal of Cosmology and Astroparticle Physics* 2017.01 (Jan. 2017), p. 006. doi: 10.1088/1475-7516/2017/01/006.
- [15] Nicola Tomassetti. “Direct Measurements of Galactic Cosmic Rays”. 2023. doi: 10.48550/ARXIV.2301.10255.
- [16] Thomas K. Gaisser, Ralph Engel, and Elisa Resconi. “Composition of cosmic rays”. In: *Cosmic Rays and Particle Physics*. 2nd ed. Cambridge University Press, 2016. Chap. 1.4. doi: 10.1017/CBO9781139192194.
- [17] Kfir Blum, Ryosuke Sato, and Eli Waxman. “Cosmic-ray Antimatter”. 2017. doi: 10.48550/ARXIV.1709.06507.
- [18] Malcolm S. Longair. “Extragalactic high energy astrophysics”. In: *High Energy Astrophysics*. IV. 2011.
- [19] A.R. Bell. “Cosmic ray acceleration”. In: *Astroparticle Physics* 43 (2013), pp. 56–70. doi: 10.1016/j.astropartphys.2012.05.022.
- [20] R. Beck. “Galactic and extragalactic magnetic fields - a concise review”. In: *Astrophysics and Space Sciences Transactions* 5.1 (2009), pp. 43–47. doi: 10.5194/asta-5-43-2009.
- [21] H. Alfvén. “Existence of Electromagnetic-Hydrodynamic Waves”. In: *Nature* 150 (Oct. 1942), pp. 405–406. doi: 10.1038/150405d0.
- [22] Meera Gupta et al. “Correlative study of solar activity and cosmic ray intensity for solar cycles 20 to 23”. In: *29th International Cosmic Ray Conference Pune* 2 (2005). Content viewed on Apr 6, 2023, pp. 147–150. URL: <https://cds.cern.ch/record/957422/files/12147-ind-gupta-M-abs1-sh34-poster.pdf>.
- [23] L. J. Gleeson and W. I. Axford. “Solar Modulation of Galactic Cosmic Rays”. In: *Astrophysical Journal* 154 (Dec. 1968), p. 1011. doi: 10.1086/149822.
- [24] *The Earth’s Magnetic Field: An Overview*. Content viewed on Mar. 11, 2023. URL: <http://www.geomag.bgs.ac.uk/education/earthmag.html>.
- [25] W. Li and M.K. Hudson. “Earth’s Van Allen Radiation Belts: From Discovery to the Van Allen Probes Era”. In: *Journal of Geophysical Research: Space Physics* 124.11 (2019), pp. 8319–8351. doi: 10.1029/2018JA025940.
- [26] D. L. Turner et al. “The Response of Earth’s Electron Radiation Belts to Geomagnetic Storms: Statistics From the Van Allen Probes Era Including Effects From Different Storm Drivers”. In: *Journal of Geophysical Research: Space Physics* 124.2 (2019), pp. 1013–1034. doi: 10.1029/2018JA026066.
- [27] Carl Störmer. “Periodische Elektronenbahnen im Felde eines Elementarmagneten und ihre Anwendung auf Brüches Modellversuche und auf Eschenhagens Elementarwellen des Erdmagnetismus. Mit 32 Abbildungen.” In: *Zeitschrift für Astrophysik* 1 (Jan. 1930), p. 237.
- [28] C. Störmer. “The polar aurora”. In: *Quarterly Journal of the Royal Meteorological Society* 82.351 (1956), pp. 115–115. doi: 10.1002/qj.49708235123.
- [29] Carl E. McIlwain. “Coordinates for mapping the distribution of magnetically trapped particles”. In: *Journal of Geophysical Research (1896-1977)* 66.11 (1961), pp. 3681–3691. doi: 10.1029/JZ066i011p03681.

- [30] M.A. Shea, D.F. Smart, and L.C. Gentile. “Estimating cosmic ray vertical cutoff rigidities as a function of the McIlwain L-parameter for different epochs of the geomagnetic field”. In: *Physics of the Earth and Planetary Interiors* 48.3 (1987), pp. 200–205. doi: 10.1016/0031-9201(87)90145-2.
- [31] “The Pierre Auger Cosmic Ray Observatory”. In: *Nuclear Instruments and Methods in Physics Research Section A: Accelerators, Spectrometers, Detectors and Associated Equipment* 798 (2015), pp. 172–213. doi: 10.1016/j.nima.2015.06.058.
- [32] *Neutrino Observatory*. Content viewed on May 13, 2023. URL: <https://icecube.wisc.edu/>.
- [33] Tianlu Yuan. “Detecting neutrinos in IceCube with Cherenkov light in the South Pole ice”. 2022. doi: 10.48550/arXiv.2212.12142.
- [34] *Opens a new window on our universe*. Content viewed on May 13, 2023. URL: <https://www.km3net.org/>.
- [35] S. Adrián-Martínez et al. “Detection potential of the KM3NeT detector for high-energy neutrinos from the Fermi bubbles”. In: *Astroparticle Physics* 42 (2013), pp. 7–14. doi: 10.1016/j.astropartphys.2012.11.010.
- [36] *Cherenkov Telescope Array*. Content viewed on May 13, 2023. URL: <https://www.cta-observatory.org/>.
- [37] J. Cortina. “Status of the Large Size Telescopes of the Cherenkov Telescope Array”. In: *Proceedings of 36th International Cosmic Ray Conference - PoS(ICRC2019)*. Vol. 358. 2019, p. 653. doi: 10.22323/1.358.0653.
- [38] P. von Doetinchem et al. “The flight of the GAPS prototype experiment”. In: *Astroparticle Physics* 54 (2014), pp. 93–109. doi: 10.1016/j.astropartphys.2013.11.009.
- [39] N. Park et al. “Cosmic-ray Isotope Measurements with HELIX”. In: *Proceedings of 36th International Cosmic Ray Conference - PoS(ICRC2019)*. Vol. 358. 2019, p. 121. doi: 10.22323/1.358.0121.
- [40] M. Aguilar et al. “The Alpha Magnetic Spectrometer (AMS) on the International Space Station: Part I - results from the test flight on the space shuttle”. In: *Physics Reports* 366.6 (2002), pp. 331–405. doi: 10.1016/S0370-1573(02)00013-3.
- [41] O. Adriani et al. “The PAMELA space mission”. In: *Astroparticle, Particle and Space Physics, Detectors and Medical Physics Applications*, pp. 858–864. doi: 10.1142/9789812819093_0143.
- [42] *Fermi Spacecraft and Instruments*. Content viewed on Mar. 11, 2023. URL: <https://www.nasa.gov/content/goddard/fermi-spacecraft-and-instruments>.
- [43] W. B. Atwood et al. “The Large Area Telescope on the Fermi Gamma-Ray Space Telescope Mission”. In: *The Astrophysical Journal* 697.2 (June 2009), pp. 1071–1102. doi: 10.1088/0004-637X/697/2/1071.
- [44] Charles Meegan et al. “The Fermi Gamma-Ray Burst Monitor”. In: *The Astrophysical Journal* 702.1 (Aug. 2009), p. 791. doi: 10.1088/0004-637X/702/1/791.
- [45] J. Chang et al. “The DArk Matter Particle Explorer mission”. In: *Astroparticle Physics* 95 (2017), pp. 6–24. doi: 10.1016/j.astropartphys.2017.08.005.
- [46] *PAMELA instrument*. Content viewed on Mar. 10, 2023. URL: https://pamela-web.web.roma2.infn.it/?page_id=56.

- [47] O. Adriani et al. “An anomalous positron abundance in cosmic rays with energies 1.5-100 GeV”. In: *Nature* 458 (Apr. 2009), pp. 607–609. doi: 10.1038/nature07942.
- [48] O. Adriani et al. “PAMELA Measurements of Cosmic-Ray Proton and Helium Spectra”. In: *Science* 332.6025 (2011), pp. 69–72. doi: 10.1126/science.1199172.
- [49] *AMS detector*. Content viewed on Mar. 10, 2023. URL: <https://ams02.space/detector>.
- [50] *AMS-01. The precursor experiment of AMS-02*. Content viewed on May 11, 2023. URL: <https://ams02.space/what-is-ams/ams-01>.
- [51] Oscar Adriani et al. “Design of an Antimatter Large Acceptance Detector In Orbit (ALADInO)”. In: *Instruments* 6.2 (2022). doi: 10.3390/instruments6020019.
- [52] S. N. Zhang et al. “The high energy cosmic-radiation detection (HERD) facility onboard China’s Space Station”. In: *Space Telescopes and Instrumentation 2014: Ultraviolet to Gamma Ray*. Vol. 9144. 2014, p. 91440X. doi: 10.1117/12.2055280.
- [53] S. Schael et al. “AMS-100: The next generation magnetic spectrometer in space - An international science platform for physics and astrophysics at Lagrange point 2”. In: *Nuclear Instruments and Methods in Physics Research Section A: Accelerators, Spectrometers, Detectors and Associated Equipment* 944 (2019), p. 162561. doi: 10.1016/j.nima.2019.162561.
- [54] *HERD facility overall design*. Content viewed on Mar. 10, 2023. URL: <http://herd.ihep.ac.cn/instrument/overall%20design/2021/743878.shtml>.
- [55] D.V. Reames. “The structure of the Sun”. In: *Solar Energetic Particles. A Modern Primer on Understanding Sources, Acceleration and Propagation*. 2nd ed. Lecture Notes in Physics. Springer Cham, Mar. 2021. Chap. 1.1. ISBN: 978-3-030-66401-5. doi: 10.1007/978-3-030-66402-2.
- [56] *Sunspots*. Content viewed on May 14, 2023. URL: <https://soho.nascom.nasa.gov/sunspots/>.
- [57] M.J. Aschwanden. *Physics of the Solar Corona. An Introduction with Problems and Solutions*. 1st ed. Springer Praxis Books. Springer Berlin, Heidelberg. ISBN: 978-3-540-30765-5. doi: 10.1007/3-540-30766-4.
- [58] E. N. Parker. “Nanoflares and the Solar X-Ray Corona”. In: *Astrophysical Journal* 330 (July 1988), p. 474. doi: 10.1086/166485.
- [59] *Coronal Hole Front and Center*. Content viewed on May 14, 2023. Oct. 2015. URL: <https://www.nasa.gov/image-feature/goddard/coronal-hole-front-and-center>.
- [60] E. N. Parker. “Solar Magnetism: The State of Our Knowledge and Ignorance”. In: *Space Science Reviews* 144 (1 Apr. 2009), pp. 15–24. doi: 10.1007/s11214-008-9445-x.
- [61] N. R. Sheeley. “Surface Evolution of the Sun’s Magnetic Field: A Historical Review of the Flux-Transport Mechanism”. In: *Living Reviews in Solar Physics* 2 (1 Oct. 2005). doi: 10.12942/lrsp-2005-5.
- [62] Y. Iida et al. “VECTOR MAGNETIC FIELDS AND DOPPLER VELOCITY STRUCTURES AROUND A CANCELLATION SITE IN THE QUIET SUN”. In: *The Astrophysical Journal* 713.1 (Mar. 2010), p. 325. doi: 10.1088/0004-637X/713/1/325.
- [63] P. Bhowmik et al. “Physical Models for Solar Cycle Predictions”. Mar. 2023. doi: 10.48550/arXiv.2303.12648.

- [64] *The Dynamic Solar Magnetic Field*. Content viewed on May 7, 2023. Jan. 2016. URL: <https://svs.gsfc.nasa.gov/cgi-bin/details.cgi?aid=4391>.
- [65] L. Fletcher et al. “An Observational Overview of Solar Flares”. In: *Space Science Reviews* 159 (1 Aug. 2011). doi: 10.1007/s11214-010-9701-8.
- [66] S. Krucker et al. “MEASUREMENTS OF THE CORONAL ACCELERATION REGION OF A SOLAR FLARE”. In: *The Astrophysical Journal* 714.2 (Apr. 2010), p. 1108. doi: 10.1088/0004-637X/714/2/1108.
- [67] E. N. Parker. “Dynamical theory of the solar wind”. In: *Space Science Reviews* 4 (5 Sept. 1965), pp. 666–708. doi: 10.1007/BF00216273.
- [68] L. F. Burlaga. *Interplanetary magnetohydrodynamics*. Vol. 3. Oxford University Press, Jan. 1995. ISBN: 978-0-19-508472-6.
- [69] “Magnetic fields and plasmas in the inner heliosphere: Helios results”. In: *Planetary and Space Science* 49.14 (2001), pp. 1619–1627. ISSN: 0032-0633. doi: 10.1016/S0032-0633(01)00098-8.
- [70] E. N. Parker. “Dynamics of the Interplanetary Gas and Magnetic Fields”. In: *Astrophysical Journal* 128 (Nov. 1958), p. 664. doi: 10.1086/146579.
- [71] Miguel O. et al. “Observation of a time lag in solar modulation of cosmic rays in the heliosphere”. In: *Journal of Physics: Conference Series* 1181.1 (Feb. 2019), p. 012013. doi: 10.1088/1742-6596/1181/1/012013.
- [72] D. F. Webb and T. A. Howard. “Coronal Mass Ejections: Observations”. In: *Living Reviews in Solar Physics* 9 (1 June 2012). doi: 10.12942/lrsp-2012-3.
- [73] *What is a coronal mass ejection or CME?* Content viewed on May 6, 2023. Mar. 2015. URL: <https://www.nasa.gov/content/goddard/what-is-a-coronal-mass-ejection>.
- [74] S. F. Martin. “Conditions for the Formation and Maintenance of Filaments - (Invited Review)”. In: *Solar Physics* 182 (1 Sept. 1998), pp. 107–137. doi: 10.1023/A:1005026814076.
- [75] T. G. Forbes et al. “CME Theory and Models”. In: *Space Science Reviews* 123 (1 Mar. 2006), pp. 251–302. doi: 10.1007/s11214-006-9019-8.
- [76] G. Mann et al. “Formation and development of shock waves in the solar corona and the near-Sun interplanetary space”. In: *Astronomy & Astrophysics* 400.1 (2003), pp. 329–336. doi: 10.1051/0004-6361:20021593.
- [77] D.V. Reames. “Solar Energetic Particles”. In: *Solar Energetic Particles. A Modern Primer on Understanding Sources, Acceleration and Propagation*. 2nd ed. Lecture Notes in Physics. Springer Cham, Mar. 2021. Chap. 1.5. ISBN: 978-3-030-66401-5. doi: 10.1007/978-3-030-66402-2.
- [78] D. V. Reames. “Particle acceleration at the Sun and in the heliosphere”. In: *Space Science Reviews* 90 (3 Oct. 1999), pp. 413–491. doi: 10.1023/A:1005105831781.
- [79] D. V. Reames. “The Two Sources of Solar Energetic Particles”. In: *Space Science Reviews* 175 (1 June 2013), pp. 53–92. doi: 10.1007/s11214-013-9958-9.
- [80] J. P. Meyer. “The baseline composition of solar energetic particles”. In: *Astrophysical Journal*. Supplement 57 (Jan. 1985), pp. 151–171. doi: 10.1086/191000.
- [81] W. R. Webber. “Solar and Galactic Cosmic Ray Abundances - A Comparison and Some Comments”. In: *International Cosmic Ray Conference*. Vol. 5. International Cosmic Ray Conference. Aug. 1975, p. 1597.

- [82] D.V. Reames. “Solar Energetic Particles. Abundances”. In: *Solar Energetic Particles. A Modern Primer on Understanding Sources, Acceleration and Propagation*. 2nd ed. Lecture Notes in Physics. Springer Cham, Mar. 2021. Chap. 1.5.2. ISBN: 978-3-030-66401-5. doi: 10.1007/978-3-030-66402-2.
- [83] D.V. Reames. “Impulsive SEP events (and Flares)”. In: *Solar Energetic Particles. A Modern Primer on Understanding Sources, Acceleration and Propagation*. 2nd ed. Lecture Notes in Physics. Springer Cham, Mar. 2021. Chap. 4. ISBN: 978-3-030-66401-5. doi: 10.1007/978-3-030-66402-2.
- [84] D. V. Reames et al. “Solar He-3-rich events and nonrelativistic electron events - A new association”. In: *Astrophysical Journal* 292 (May 1985), pp. 716–724. doi: 10.1086/163203.
- [85] D. V. Reames and R. G. Stone. “The Identification of Solar 3He-rich Events and the Study of Particle Acceleration at the Sun”. In: *Astrophysical Journal* 308 (Sept. 1986), p. 902. doi: 10.1086/164560.
- [86] J. M. Laming. “The FIP and Inverse FIP Effects in Solar and Stellar Coronae”. In: *Living Reviews in Solar Physics* 12 (1 Sept. 2015). doi: 10.1007/lrsp-2015-2.
- [87] P. Bochsler. “Composition of matter in the heliosphere”. In: *Proceedings of the International Astronomical Union* 4.S257 (2008), pp. 17–28. doi: 10.1017/S1743921309029044.
- [88] J. Geiss. “Processes affecting abundances in the solar wind”. In: *Space Science Reviews* 33 (1 Mar. 1982), pp. 201–217. doi: 10.1007/BF00213254.
- [89] R. A. Mewaldt et al. “Fractionation of solar energetic particles and solar wind according to first ionization potential”. In: *Advances in Space Research* 30.1 (2002), pp. 79–84. doi: 10.1016/S0273-1177(02)00263-6.
- [90] Donald V. Reames. In: *Solar Physics* 293 (3 Feb. 2018). doi: 10.1007/s11207-018-1267-8.
- [91] A. Kounine. “Status of the AMS Experiment”. 2010. doi: 10.48550/ARXIV.1009.5349.
- [92] NASA official Flickr profile. URL: <https://www.flickr.com/people/nasa2explore/>.
- [93] Picture of AMS-02. URL: <https://www.flickr.com/photos/nasa2explore/32302130661/>.
- [94] Picture of the International Space Station. Nov. 2021. URL: <https://www.flickr.com/photos/nasa2explore/51814201006/in/album-72157720187084178/>.
- [95] The AMS Magnet. Content viewed on Mar 16, 2023. URL: <https://ams02.space/detector/magnet>.
- [96] The AMS Silicon Tracker. Content viewed on Mar 16, 2023. URL: <https://ams02.space/detector/silicon-tracker>.
- [97] B. Alpat et al. “The internal alignment and position resolution of the AMS-02 silicon tracker determined with cosmic-ray muons”. In: *Nuclear Instruments and Methods in Physics Research Section A: Accelerators, Spectrometers, Detectors and Associated Equipment* 613.2 (2010), pp. 207–217. doi: 10.1016/j.nima.2009.11.065.
- [98] K. Lübelsmeyer et al. “Upgrade of the Alpha Magnetic Spectrometer (AMS-02) for long term operation on the International Space Station (ISS)”. In: *Nuclear Instruments and Methods in Physics Research Section A: Accelerators, Spectrometers, Detectors and Associated Equipment* 654.1 (2011), pp. 639–648. doi: 10.1016/j.nima.2011.06.051.

- [99] L. Mussolin et al. “Overview of the mechanical, thermal vacuum and EMI/EMC tests performed for the AMS-02 UTTPS space qualification campaign”. In: *2020 IEEE 20th Mediterranean Electrotechnical Conference (MELECON)*. 2020, pp. 130–135. doi: 10.1109/MELECON48756.2020.9140595.
- [100] Wolfgang Wallraff. “The AMS-02 tracker alignment system for 3D position control with artificial laser generated straight tracks”. In: *Nuclear Instruments and Methods in Physics Research Section A: Accelerators, Spectrometers, Detectors and Associated Equipment* 572.1 (2007), pp. 325–327. doi: 10.1016/j.nima.2006.10.273.
- [101] V. Bindi et al. “Calibration and performance of the AMS-02 time of flight detector in space”. In: *Nuclear Instruments and Methods in Physics Research Section A: Accelerators, Spectrometers, Detectors and Associated Equipment* 743 (2014), pp. 22–29. doi: 10.1016/j.nima.2014.01.002.
- [102] *The AMS Time of Flight counters*. Content viewed on Mar 16, 2023. URL: <https://ams02.space/detector/time-flight-tof-counters>.
- [103] L. Brocco et al. “Photomultipliers behavior in strong magnetic field, for the TOF system of the AMS-02 space experiment”. In: *International Cosmic Ray Conference*. Vol. 6. 2001, p. 2193.
- [104] T. Bruch and W. Wallraff. “The Anti-Coincidence Counter shield of the AMS tracker”. In: *Nuclear Instruments and Methods in Physics Research Section A: Accelerators, Spectrometers, Detectors and Associated Equipment* 572.1 (2007), pp. 505–507. doi: 10.1016/j.nima.2006.10.376.
- [105] A.C. Pigna. *AMS-02 experiment*. Content viewed on Mar 16, 2023. URL: <http://www.fisica.unipg.it/valdata/rivelatori/Lezioni/L%5C%92esperimento%5C%20AMS-02.pdf>.
- [106] T. Siedenburg. “The AMS TRD. A gasdetector designed for operation in space”. In: *Nuclear Physics B - Proceedings Supplements* 150 (2006), pp. 30–33. doi: 10.1016/j.nuclphysbps.2004.06.001.
- [107] Ruoxi Chen et al. “Recent advances of transition radiation: Fundamentals and applications”. In: *Materials Today Electronics* 3 (2023), p. 100025. doi: 10.1016/j.mtelec.2023.100025.
- [108] *The Transition Radiation Detector (TRD)*. Content viewed on Mar 20, 2023. URL: <https://ams02.space/detector/transition-radiation-detector-trd>.
- [109] Wei Sun. “Measurement of the absolute charge of cosmic ray nuclei with the AMS Transition Radiation Detector”. In: *33rd International Cosmic Ray Conference*. 2013, p. 0940.
- [110] M. Heil et al. “Operations and Alignment of the AMS-02 Transition Radiation Detector”. In: *33rd International Cosmic Ray Conference*. 2013, p. 1232.
- [111] F. Giovacchini. “Performance in space of the AMS-02 RICH detector”. In: *Nuclear Instruments and Methods in Physics Research Section A: Accelerators, Spectrometers, Detectors and Associated Equipment* 766 (2014), pp. 57–60. doi: 10.1016/j.nima.2014.04.036.
- [112] *The Ring Imaging Cherenkov Detector (RICH)*. Content viewed on Mar 20, 2023. URL: <https://ams02.space/detector/ring-imaging-cherenkov-detector-rich>.

- [113] C. Adloff et al. “The AMS-02 lead-scintillating fibres Electromagnetic Calorimeter”. In: *Nuclear Instruments and Methods in Physics Research Section A: Accelerators, Spectrometers, Detectors and Associated Equipment* 714 (2013), pp. 147–154. doi: 10.1016/j.nima.2013.02.020.
- [114] G. Gallucci. “Performance of the AMS-02 Electromagnetic Calorimeter in Space”. In: *Journal of Physics: Conference Series* 587.1 (2015), p. 012028. doi: 10.1088/1742-6596/587/1/012028.
- [115] Egidio Longo and Ignazio Sestili. “Monte Carlo calculation of photon-initiated electromagnetic showers in lead glass”. In: *Nuclear Instruments and Methods* 128.2 (1975), pp. 283–307. doi: 10.1016/0029-554X(75)90679-5.
- [116] Stefano Di Falco. “Performance of the AMS-02 Electromagnetic Calorimeter in Space”. In: vol. 33. International Cosmic Ray Conference. Jan. 2013, p. 562.
- [117] Manuela Vecchi, Kaiyuan Wu, and Yuan-Hann Chang. “A 3-dimensional electromagnetic shower characterization and its application to AMS-02 pointing capability”. In: *33rd International Cosmic Ray Conference*. 2013, p. 0653.
- [118] F. Cadoux et al. “The Electromagnetic Calorimeter Trigger System for the AMS-02 Experiment”. In: *IEEE Transactions on Nuclear Science* 55.2 (2008), pp. 817–821. doi: 10.1109/TNS.2008.918517.
- [119] C. Lin. *Trigger Logic Design Specification*. Internal document of AMS-02 collaboration (n. AMS-JT-JLV1-LOGIC-R02c). Nov. 2005.
- [120] M. Duranti. “Measurement of the Atmospheric Muon Flux on Ground with the AMS-02 Detector”. PhD thesis. 2012. URL: <https://cds.cern.ch/record/1543542>.
- [121] A. Kounine and V. Koutsenko. *Flight Software for xDR and JINx nodes in AMS-02*. Feb. 2011. URL: https://www.researchgate.net/publication/265159183_Flight_Software_for_xDR_and_JINx_nodes_in_AMS-02.
- [122] Raheem Karim Hashmani et al. “New monitoring interface for the AMS experiment”. In: *Nuclear Instruments and Methods in Physics Research Section A: Accelerators, Spectrometers, Detectors and Associated Equipment* 1046 (2023), p. 167704. doi: 10.1016/j.nima.2022.167704.
- [123] *InfluxData website*. URL: <https://www.influxdata.com/>.
- [124] *Grafana project website*. URL: <https://grafana.com/grafana/>.
- [125] *Documentation of CERN Database On Demand (DBOD) service*. URL: <https://dbod-user-guide.web.cern.ch/>.
- [126] *Documentation of CERN Grafana*. URL: <https://grafana.docs.cern.ch/>.
- [127] *Grafana instance hosted by CERN of AMS Monitoring Interface*. Accessible with a CERN computing account or through eduGAIN. URL: <https://ams-ami.web.cern.ch/>.
- [128] Andrea Serpolla. *AMI SEP repository*. URL: <https://baltig.infn.it/andrea.serpolla/ami-sep/>.
- [129] *SpacePy documentation*. Content viewed on May 16, 2023. URL: <https://spacepy.github.io/>.
- [130] *irbempy. Python interface to IRBEM library*. Content viewed on May 16, 2023. URL: <https://spacepy.github.io/irbempy.html>.

- [131] *IRBEM library user's guide*. Content viewed on May 16, 2023. URL: <https://prbem.github.io/IRBEM/>.
- [132] *International Geomagnetic Reference Field (IGRF)*. Content viewed on May 16, 2023. URL: <https://www.ncei.noaa.gov/products/international-geomagnetic-reference-field>.
- [133] P. Alken et al. “International Geomagnetic Reference Field: the thirteenth generation”. In: *Earth, Planets and Space* 73 (1 Feb. 2021). doi: 10.1186/s40623-020-01288-x.
- [134] *External Payloads Proposer's Guide to the International Space Station*. Content viewed on May 17, 2023. NASA. URL: https://www.nasa.gov/mission_pages/station/research/facilities_external_payloads_proposer_guide.
- [135] Andrea Serpolla. *AMI SEP Grafana*. Accessible with a CERN computing account or through eduGAIN. URL: <https://ami-sep-monitor.app.cern.ch>.
- [136] *Solar Proton Events. 1976 – present*. Content viewed on May 22, 2023. URL: <https://umbra.nascom.nasa.gov/SEP/>.

List of Acronyms

A

- ACC** Anti-Coincidence Counters. 2, 16, 29, 30, 34, 38, 40–42
ACC0 ACC signal 0. 40
ACC1 ACC signal 1. 40
ACD Anti-Coincidence Detector. 15
ADC Analog-to-Digital Converter. 35
AGN Active Galactic Nucleus. 1, 3, 6
ALADInO Antimatter Large Acceptance Detector In Orbit. 16, 17
AMS Alpha Magnetic Spectrometer. 1, 2, 12, 14, 16, 29–44, 47–49, 59, 60, 67, 68
AMI AMS Monitoring Interface. 30, 43, 45, 47–50, 52, 53, 59, 64, 67, 68
AMS-01 Alpha Magnetic Spectrometer 01. 14, 16, 29, 30
AMS-02 Alpha Magnetic Spectrometer 02. 1, 16, 17, 29, 30, 56, 70, 72, 74, 76, 78, 80, 82, 84, 86, 88, 90, 92
AMS-100 Alpha Magnetic Spectrometer 100. 16, 18

B

- BZ** Big-Z. 39–41

C

- CDF** cumulative distribution function. 48
CERN European Organization for Nuclear Research, or *Conseil Européen pour la Recherche Nucléaire*. V, 2, 29, 30, 43, 44
CMB Cosmic Microwave Background. 4
CME Coronal Mass Ejection. 1, 20–23, 27, 94
CP Charged Particle. 39, 40
CR Cosmic Ray. 1–14, 29, 59, 67, 68
GCR Galactic Cosmic Ray. 1, 3, 5–7
CSN2 National Scientific Commission 2, or *Commissione Scientifica Nazionale 2*. V
CT Charged particle in Tracker acceptance. 39, 40
CTA Cherenkov Telescope Array. 13

D

- DAMPE** DArk Matter Particle Explorer. 14–16
DAQ Data Acquisition. 30, 38, 42–44
DR Data Reduction. 42, 44
EDR ECAL Data Reduction. 42
SDR2 ToF & ACC Data Reduction. 42

TDR Tracker Data Reduction. 42
UDR TRD Data Reduction. 42
DSA Diffusive Shock Acceleration. 1, 3, 6, 7

E

ECAL Electromagnetic Calorimeter. 2, 16, 30, 32, 37–42
ECAL-A ECAL Angular. 40
ECAL-F ECAL Fast. 39, 40
ECAL-F_and ECAL Fast AND signal. 39, 40
ECAL-F_or ECAL Fast OR signal. 39, 40
ETRG ECAL Trigger. 38–40
EM electromagnetic. 41

F

Fermi-GBM Fermi Gamma-ray Burst Monitor. 15
Fermi-LAT Fermi Large Area Telescope. 15
FIFO First In, First Out. 50
FIP First Ionization Potential. 19, 24, 25, 28
FT Fast Trigger. 30, 39–41, 43, 48, 62, 72, 95
FTC Fast Trigger Charged. 40, 41, 48, 74, 96
FTE Fast Trigger ECAL. 40, 41, 48, 64–66, 68, 78, 96, 99
FTZ Fast Trigger big-Z. 40, 41, 48, 61, 64, 76, 96, 99

G

GAPS General AntiParticle Spectrometer. 13
GOES Geostationary Operational Environmental Satellite. 94
GRB Gamma-Ray Burst. 15
GZK-mechanism Greisen-Zatsepin-Kuzmin mechanism. 4

H

HCS Heliospheric Current Sheet. 9, 22, 26
HELIX High Energy Light Isotope eXperiment. 13
HERD High Energy cosmic-Radiation Detection. 16, 18
HG High Gain. 37, 38
HT High Threshold. 39, 41

I

IGRF International Geomagnetic Reference Field. 49
INFN National Institute of Nuclear Physics, or *Istituto Nazionale di Fisica Nucleare*. I, V
IRBEM International Radiation Belt Environment Modeling. 49
ISM Interstellar Medium. 1, 3–6, 22
ISS International Space Station. 1, 2, 12, 16, 29, 30, 43, 47–50, 54–56, 59, 61, 64, 67, 68

K

KM3NeT Cubic Kilometre Neutrino Telescope. 13

L

LASCO Large Angle and Spectrometric COronagraph. 22, 27

LEO Low Earth Orbit. 1, 9, 67

LG Low Gain. 37, 38

LIS Local Interstellar Spectrum. 8

LV1 Level 1. 30, 39–42, 48, 58, 62, 63, 80, 97, 103

subLV1 sub-Level 1. 41

subLV1_0 sub-Level 1 signal 0. 48, 82, 97

subLV1_1 sub-Level 1 signal 1. 48, 84, 97

subLV1_2 sub-Level 1 signal 2. 48, 86, 98

subLV1_3 sub-Level 1 signal 3. 48, 61, 64, 88, 98, 99

subLV1_4 sub-Level 1 signal 4. 48, 64, 90, 98, 99

subLV1_5 sub-Level 1 signal 5. 48, 64, 92, 99

subLV1_6 sub-Level 1 signal 6. 48, 61

LVLH Local Vertical Local Horizontal. 49, 55

M

MDI Michelson Doppler Imager. 21

MDR Maximum Detectable Rigidity. 32

MIP Minimum Ionizing Particle. 38, 39

ML Machine Learning. 68

N

NASA National Aeronautics and Space Administration. 22, 30, 43, 44

NUD Neutron Detector. 15

P

PAMELA Payload for Anti-Matter and Light-nuclei Astrophysics. 14

PDF probability density function. 48, 50, 67

PMT photomultiplier. 13, 33, 34, 37–39

SiPM silicon photomultiplier. 13

POCC Payload Operations and Control Center. 30, 43

PSD Plastic Scintillator Detector. 15

R

RICH Ring Imaging Cherenkov. 2, 16, 30, 32, 36, 37, 42

rms root mean square. 50, 56, 57, 67

S

SAA South Atlantic Anomaly. 51, 60

SDE Stochastic Differential Equation. 1, 10

SDO Solar Dynamic Observatory. 22

SEP Solar Energetic Particle. 1, 2, 19, 21, 23–25, 27, 28, 47–49, 51, 59–68, 99, 103

SHT Super-High Threshold. 39, 41

SILSO Sunspot Index and Long-term Solar Observations. 24

SL SuperLayer. 37–39

SMF Solar Magnetic Field. 1, 9, 19–21, 26

SN Supernova. 1, 3, 5–7
SNR Supernova Remnant. 1, 3, 5, 6
SOHO Solar and Heliospheric Observatory. 21, 22, 27, 94
SPE Solar Proton Events. 94
SSN Solar Sunspot Number. 10, 20, 24
STK Silicon-Tungsten tracKer-converter. 15
SW Solar Wind. 1, 9, 19–22, 24–26
SWPC Space Weather Prediction Center. 94

T

TAS Tracker Alignment System. 32
ToF Time-of-Flight. 2, 16, 29, 30, 32–34, 36, 38–42
TRD Transition Radiation Detector. 2, 16, 29, 32, 34–36, 42

U

UTC Coordinated Universal Time. 45
UTTPS Upgraded Tracker Thermal Pump System. 32

W

WDC World Data Center. 24
WSO Wilcox Solar Observatory. 24